Suitability of different nanocomposite concepts for self-lubricating hard coatings

Mag. Karl Philipp Budna

Leoben, August 2009

Being a thesis in partial fulfillment of the requirements for the degree of a

Doctor of montanistic science (Dr.mont.)

at the University of Leoben

This thesis was done within the EU project NAPILIS (Nanocomposites for piston/liner systems) at the Materials Center Leoben Forschung GmbH.

Affidavit

I declare in lieu of oath that I did the PhD thesis by myself using only literature cited in this volume.

Graz, November 2009

Acknowledgements

I would like to thank the Head of the Department of Physical Metallurgy and Materials Testing, Univ.Prof. Dr. DI Helmut Clemens, for the opportunity to carry out this thesis at the institute.

My sincerest gratitude is due to my supervisor and Head of the Thin Film Group, ao. Univ. Prof. Dr. DI Christian Mitterer, for his guidance and help, for the interesting discussions, for his kindness and support and for giving an expertise to this thesis. I am greatful for everything I have learned from him.

Furthermore I would like to thank Priv.-Doz. Dr. DI Paul Mayrhofer, Dr. DI Claudia Walter and Dr. Dipl.Phys. (FH) Jörg Neidhardt for their valuable comments and discussions concerning my experimental.

Special thanks to my co-workers Thomas Klünsner and Roland Spicak for their excellent work being a part of this thesis.

I would also like to express my sincere appreciation to my colleagues of the Thin Film Group of the Department of Physical Metallurgy and Materials Testing for their patience and helpful discussion in all matters.

I am very indepted to ao. Univ. Prof. Dr. DI Reinhold Ebner, Managing Director of the Materials Center Leoben Forschung GmbH, for giving me the opportunityfor doing this work.

Dr. Béla Pécz, Dr. Lajos Tóth, Dr. Eva Hegedũs, István Kovács (MFA Budapest) and Prof. Dr. Erich Bergmann (EIG Geneva) have to be accounted for their scientific contribution in course of the EU project ‘NAPILIS’. In the same way, I would like to thank DI Alex Fian (Joanneum Research, Weiz) and Gerhard Hawranek (Department of Physical Metallugy and Marterials Testing, Leoben) for offering their help during various XPS and SEM sessions.

My final and special thanks go to my beloved family. Without their everlasting support and faith throughout my entire life, it would have never been possible to do this thesis. I am deeply grateful to them.

Table of contents

1 Introduction

Since the early seventies, protective thin films for improvement of mechanical and tribological properties of tools and components became increasingly essential for industrial applications in many fields. This is based on their preeminent properties like high hardness, excellent corrosion resistance, and good tribological behaviour [Ro92a]. Physical Vapor Deposition (PVD) and Chemical Vapor Deposition (CVD) coatings are well established for wear protection, especially for cutting and forming applications. Moreover, based on their decorative, thermal and electrical properties, these coatings nowadays also open new fields in mechanical and plant engineering, microelectronics, medical devices and environmental engineering [Ba00].

Especially for automotive components like piston rings, the combination of a high wear resistance with a low friction coefficient due to self-lubrication is desired to increase lifetime, performance and efficiency and to decrease fuel consumption and emissions of CO_2 and fine particles [Kv78].

Auspicious candidates are self-lubricating metal and ceramic matrix nanocomposites (SLMCMNCs), which consist of a metal or hartstoff matrix (a refractory metal like tungsten, titanium, molybdenum and chromium or a carbide or nitride of these metals) with dispersed self-lubricating nanoparticles (like graphite, h-BN, MoS_2 or WS_2). SLMCMNCs have so far never been synthesized and there exists no process technology for their synthesis. Self-lubricating microcomposites with a lubricant matrix (diamond like carbon, DLC) and carbide (WC, B_4C) inclusions are state of the art since 15 years. They are produced by a vapor deposition method on a large scale, by filling (SiC/C), sintering and casting (e.g. grey cast iron, Pb/PTFE, CuSnPb, AlSn, etc), galvanic & electroless deposition (Ni/PTFE), plasma spraying (alloy + MoS_2, PTFE) and used for gliding seals [St00]. These technologies used for self-lubricating microcomposites can not be used for nanocomposites due to their environmental impact. They would involve handling of large quantities of powders of nanosized particles, which are a clear health risk.

The aim of this thesis is to develop novel multiphase and multifunctional coatings of SLMCMNC type which combine high wear resistance with low friction properties. State of the art for piston/liner systems are thin CrN coatings which fulfill the present requirements, but produce too high friction losses under marginal lubrication. Therefore the goal is to produce dense, relatively hard and wear resistant coatings based on CrN with a sufficiently high concentration of a lubricant phase to obtain self-lubrication. The presence of a solid lubricant reservoir throughout the coating thickness should allow lubrication to be maintained even as the coating gradually wears away. As solid lubricant phases h-BN, MoS_2 and WS_2 were chosen due to their hexagonal and layered structure [Ho95] permitting sheering and lubricating even at higher temperatures (above 300°C) in ambient air atmosphere [Bh01,Bo01].

The deposition of the coatings has been performed using a unbalanced direct current (dc) magnetron sputtering plant [Lo98,Mi94]. The coatings were characterized with respect to their chemical, structural, mechanical, and tribological properties and behaviour. These investigations were performed by means of standard analysis methods [Br92] like electron probe micro analysis (EPMA), X-ray photoelectron spectroscopy (XPS), scanning electron microscopy (SEM), transmission electron microscopy (TEM), X-ray diffraction (XRD), microhardness measurements, biaxial stress temperature measurements (BSTM), ball-on-disk tests, and white light interferometry [DI-a].

While the first chapters of this thesis will give a short introduction in tribology of thin films, PVD, general aspects of coating materials as well as solid lubricants, and applied methods for coating analysis, the major experimental research is summarized in four subsequently given publications.

2 Friction and wear

Tribology (this term was defined 1966 by a commission of the British government, based on the greek word “tribos” for rubbing) is a modern aspect of engineering science and understood as “the science and technology of interacting surfaces in relative motion and all practices related thereto”. Consequently, the term tribology deals with phenomena related to friction, wear, and lubrication [Bl89].

2.1 General

Friction is the resistance to motion which is experienced whenever one solid body slides relative to another. The resistive force (also known as friction force) acts tangential to the interface, perpendicular to the normal force and opposite to the direction of sliding [Ar91,Ho94]. The coefficient of friction μ is the frictional force F, divided by the normal load F_N on the contact as given in equation 2.1.

$$\mu = \frac{F}{F_N} \tag{2.1}$$

Wear is defined as the gradual loss of material from contacting solid surfaces in relative motion [Bu96]. The term wear rate describes the ratio of the volume of removed material (or dimensional change) due to the wear per applied load and sliding distance, whereas K stands for the wear rate, V for the removed volume of material, and s for the sliding distance, respectively. The wear rate K is often used with the dimension [10^{-6}mm^3/Nm] [Ba02].

$$K = \frac{V}{F_N \times s} \tag{2.2}$$

Mostly, wastage of surface material can be observed, but some materials can wear without wastage of surface material, e.g. grooving and scratching of ductile materials [Bu96]. Friction and wear can only be described as system property but never as a material property of the particular tribo-bodies due to the occurring mechanism and state of contacts during testing [Ga87,Ka00a]. A tribo-system consists of at least two bodies, but more often formation of a third or more new generated bodies can be seen (e.g. abrasive particles, oxide-layers, liquid films, etc.). Tribology might also be understood as a black box, which transforms input data like materials, lubricants or geometry to output data, which are friction and wear (cp. Fig. 2.1).

To describe the tribological contact while sliding, several mechanisms, which might occur at the same time, have to be considered. Five types of mechanisms can be identified and are shown in Figure 2.1 [Ho00a].

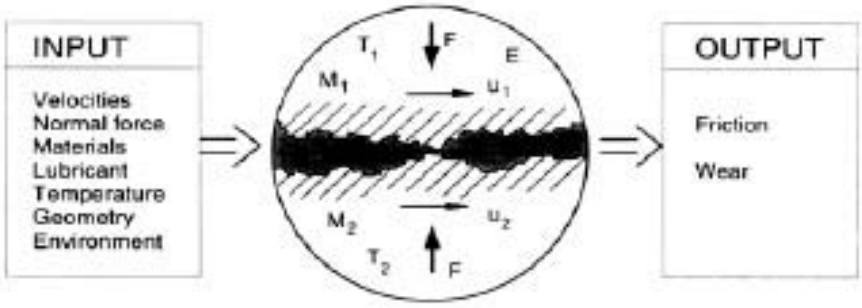

Figure 2.1: Input and output data of a schematic tribo-system. Sliding velocity, normal force, material compositions, etc., can be set as input data, which will be transformed by tribo-chemical and -physical mechanisms to friction and wear as observable output data [Ho94].

Macromechanical changes embrace strains and stresses, the deformation (elastic and plastic) and the origin and dynamics of wear particles in the contact area.

Micromechanical changes describe the stress and strain origin at an asperity-to-asperity level, the crack formation and propagation, material liberation and particle formation. Typically, these phenomena are sized with about 1 mm or less.

Tribochemical changes are placed at the surfaces during sliding contact and/or during the periods between repeated contacts. Due to the compositional changes of the outmost surfaces, differences of the mechanical properties can be observed.

Material transfer and wear particles liberated from the surface influence the tribological behaviour of the contacts. Loose wear debris in the contact zone influence friction by plowing or asperity deformation but also attach to the counterface and generate a new transfer layer with significantly different tribological properties of the contact area.

Nanophysical changes describe tribological phenomena in the molecular and atomic scale. The enlarged understanding of the formation of friction at the atomic scale and why friction exists has resulted in investigations of the relationship between the conventional used laws of tribology at a macro scale and the molecular frictional behaviour on a nano-scale.

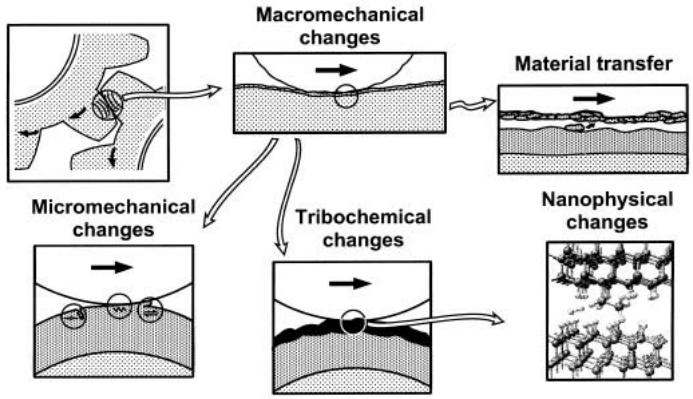

Figure 2.2: Tribological contact mechanisms are related to macromechanical changes, material transfer, micromechanical, tribochemical and nanophysical changes in the contact [Ho00a].

2.2 Tribological mechanics and models

2.2.1 Genesis of friction

Although serious investigations to understand friction between sliding surfaces have started in the 1940's [Bo50,Er40,Ra65,Sh49], the first satisfying concept was published by Suh and Sin [Su81]. They combined the consisting tribological models to a theory, where the mechanical properties of participating materials are affecting the tribological behaviour to a greater extent at moderate interfacial temperature than chemical properties of the counterparts while sliding. Suh *et al.* also demonstrated that adhesion does not play a significant role on the onset of sliding under typical sliding conditions and that the frictional force (and therefore the friction coefficient μ) mainly is based on adhesion (Fig. 2.3a), plowing by wear particles and asperities (Fig. 2.3b), and asperity deformation (Fig. 2.3c).

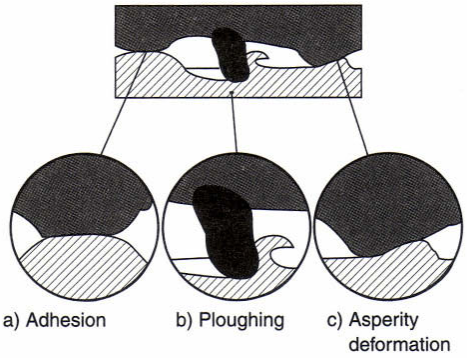

Figure 2.3: The three components of sliding friction are **(a)** adhesion, **(b)** plowing, and **(c)** asperity deformation [Ho01].

The relative contribution of these three components depends on the conditions of sliding interfaces which is influenced by the history of sliding, the specific materials, the surface topography, and the environment [Su81].

In the proposed concept of Suh *et al.*, they have defined several different stages of frictional mechanism during sliding contact of metals before reaching the steady-state level (see Fig. 2.4).

Figure 2.4: Six stages in friction force vs. sliding distance for metal/metal contacts [Su81].

stage I: The friction coefficient μ is more or less independent of the material combination, the surface conditions and the environmental conditions and controlled by plowing of the surface by asperities. This is due to the origin and deformation of asperities, the contamination of the surface in combination with occurring polishing and results in a non-adhesion-controlled mechanism.

stage II: The friction coefficient begins to rise because of an increase of adhesion. This is based on removal of oxide layer and generation of wear particles generated by asperity deformation and fracture which plow the surface.

stage III: The higher number of entrapped wear particles between the sliding surfaces as a consequense of higher wear rates induces an elevated friction force. This is also affected by an increase in adhesion due to the increase in clean interfacial area. The force needed to deform the asperities will continue to contribute to the frictional force as long as surface asperities are existent. For metals with nearly equal hardness, plowing will be higher due to the penetration of wear particles into both surfaces (prevents any slippage between the particle and the surfaces).

stage IV: The maximum is reached when the number of wear particles entrapped between the surfaces remains constant (equilibrium between newly entrapped and leaving entrapped particles). When asperity deformation is done and the number of new asperities generated is low, plowing is more effective than deformation. Normally, for two metals sliding against each other, the friction coefficient of stage IV complies with the steady state friction force.

stage V: For the case of a hard stationary slider sliding against a soft counterpart, the asperities of the hard surface become removed step by step and create a mirror polish. Due to the decrease in plowing (no anchor on a polished surface) and asperity deformation, a decrease of the friction force can be noticed.

stage VI: A steady state condition is reached once both sliders show a polished surface topography and wear particles do not affect further influences.

The concept of Suh *et at.* has been postulated for a steel-steel-system as friction counterparts. Differences for other materials can thus be expected [Bu99,Su91].

2.2.2 Wear mechanisms

Wear originates by chemical and/or mechanical means and is universally promoted by thermal means. There are different wear mechanisms to describe the way of removal of material from the surface, but a classification for fundamental wear mechanism was given by Blau [Bl89]. He subdivided them into (1) adhesive wear, (2) abrasive wear, (3) surface fatigue and (4) tribochemical reactions (see Fig. 2.5).

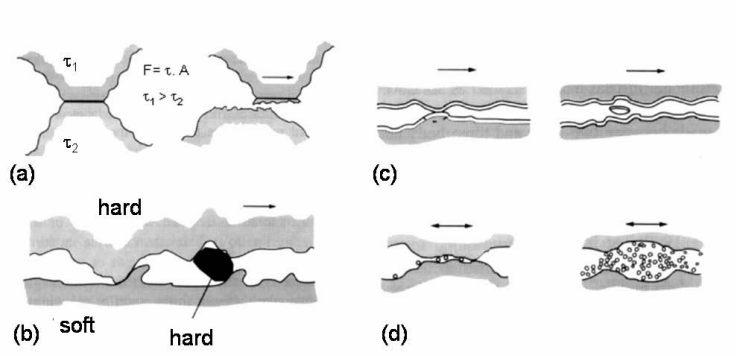

Figure 2.5: The fundamental mechanisms of wear are **(a)** adhesion, **(b)** abrasion, **(c)** fatigue, and **(d)** tribochemical wear [Bl89].

Adhesive wear is characterized by the formation of local asperity junctions during sliding against each other (cp. Fig. 2.5a). Tangential motion of the contact zones results in fracture of these junctions and material removal or transfer from one material surface to the opposite one. Depending on position of shearing, the amount of wear varies. No wear will be formed if fracture is localized at the initial asperity junctions, whereas adhesive wear occurs when fracture takes place away from the initial junctions which results in transfer material. Physical and chemical properties of both solid surfaces are responsible for the tendency of formation of junctions, as well as contact and operation conditions (load, contact area, etc.) or topographic factors like roughness or contaminations on the surface [Ho94,Ra95].

Abrasive wear is the removal of material affected by hard particles (Fig. 2.5b). It can be classified into two different types. The first one is called as two-body abrasion and occurs when hard asperities of the counterface slide against a softer surface (Fig. 2.6). The asperities are pressed into the softer material and cause plastic flow and displacement of the softer surface. In three-body abrasion, hard asperities are placed between the sliding surfaces and cause material removal of one or both of them. Several mechanical processes are responsible for abrasion, depending on material hardness, operating conditions or geometry [Bu04,Bu96,Ga87,Ho94].

Surface fatigue can be observed after repeated loading and unloading cycles (Fig. 2.5c). They result in origin of surface cracks and delamination. Cyclic loading are released by repeated sliding, rolling, or impact contact. These cracks grow parallel to the surface direction and result in flaking of the material and formation of large asperities [Bu96,Ga87,Ho94].

Tribochemical wear embraces rubbing in a corrosive (oxidizing or reducing) environment (Fig. 2.5d). Chemical reaction products on the surface of one or both of the sliding pairs or on the surface of wear debris influence the sliding process due to their different chemical, physical and tribological properties. This kind of mechanism is mostly determined by the chemical composition and reactivity of the participating surfaces and materials, the

presence of reactive environments (ambient air, humidity, lubricants), and temperature [Ga87,Ho94].

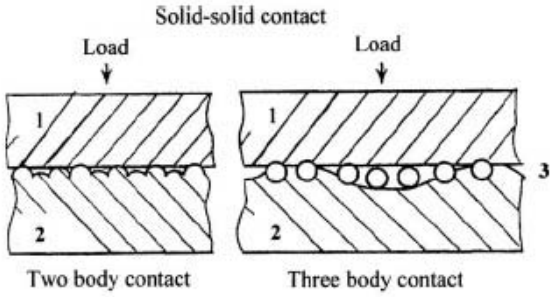

Figure 2.6: Schematic of two-bodiy and three-body contact of rough surfaces [Bu04].

2.3 Tribology of thin films

New approaches in thin film technology permit the coating/substrate system to be tailored for specific applications with optimal conditions based on advancements and improvements in understanding of tribomechanisms during contact [Ho98].

Contact mechanisms during relative motion can be described as a black box model with several input and output parameters (see Fig. 2.7). Material input parameters like geometry, chemical composition and environment, microstructure, mechanical properties as well as energy parameters (velocity, temperature, etc.) can be specified in front of the tribological contact. Mechanical and tribomechanical changes as well as material transfer can be determined by means of output parameters. Changes in geometry, topography, chemical composition, increase or decrease of particles or fluids but also energy terms like friction, wear and temperature represent typical output parameters taken for modelling [Ho01,Ho98]. As mentioned before, measurement of forces and mass changes will be taken for classification of friction and wear.

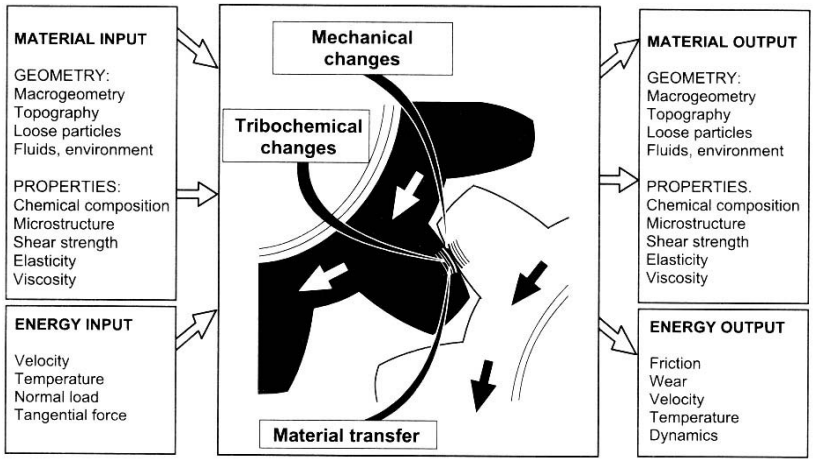

Figure 2.7: The tribological process in a contact between two surfaces [Ho01].

Stress, strain distribution in the contact zone, the originated elastic and plastic deformation and additionally the kind of process and dynamics of formation of wear particles describes the friction and wear but also the involved tribological mechanisms. For the contact conditions for solids where at least one of them is coated, additional four critical parameters have to be defined [Ho01,Ho94], and they are:

- hardness relationship between coating and substrate
- thickness of the coating
- roughness of the surface and
- size and hardness of wear particles in the contact zone

The relationships between these four parameters results in 12 very typical tribological contact conditions with different friction and wear mechanisms for a hard sliding body (Fig. 2.8) [Ho00a,Ho01,Ho94,Ho98].

As an important factor, coating hardness and its relationship to substrate hardness can be determined. Bowden et al. [Bo01] demonstrated the benefits of soft coatings for friction reduction. There, friction force can ideally be seen as the product of contact zone and shear strength. Further decrease of friction can be obtained by using an additional soft thin film on a hard substrate. This lowers the interfacial shear strength as well as the contact zone. Furthermore, wear reduction can be achieved by using a hard coating on a softer substrate material due to preventing ploughing, in particular in abrasive environments. The formation of a microfilm with small shear strength on the surface of the coating also reduces friction. This is based on the effect that the shearing takes place in this microfilm while the load is supported by the hard coating.

The next crucial parameter is the thickness of the coating. It influences the ploughing component of the coating and is more distinct for thicker films (see Figs. 2.8a and b). There, the friction is assigned by the shear strength of the coating and the contact zone, which the latter is related to the deformation properties of the substrate material. For soft thick coatings, an increase in friction can be observed. This is both due the deformation ability of the coating (elastic and/or plastic) and the enhanced contact zone at the interface (between film and counterbody). In this region, the shear takes place (Fig. 2.8a). For the combination of soft substrates and thin hard films, the film is not able to sustain the load and elastic and/or plastic deformation in the substrate can be found (Fig. 2.8d). One the other hand, the requirement of protective coatings is to separate the substrate from the surface of the counterpart and the obviation of ploughing. Thicker hard coatings are able to resist elevated loads due to their load-carrying capacity (Fig. 2.8c). As third determining influence for the contact conditions of coating/substrate systems the surface roughness can be defined. For substrates with a considerable smaller surface roughness than the thickness of a soft coating, substrate roughness can be neglected due the capacity of load-carrying of the film (Fig 2.8e). On the other hand coating penetration can

be observed when the film thickness is smaller than the roughness of the counterpart. Due to scratching of substrate material, an elevated friction will emerge (Fig. 2.8f). Sliding on a small number of asperity tops can be found for hard rough counterparts sliding over a thick hard film (Fig. 2.8g).

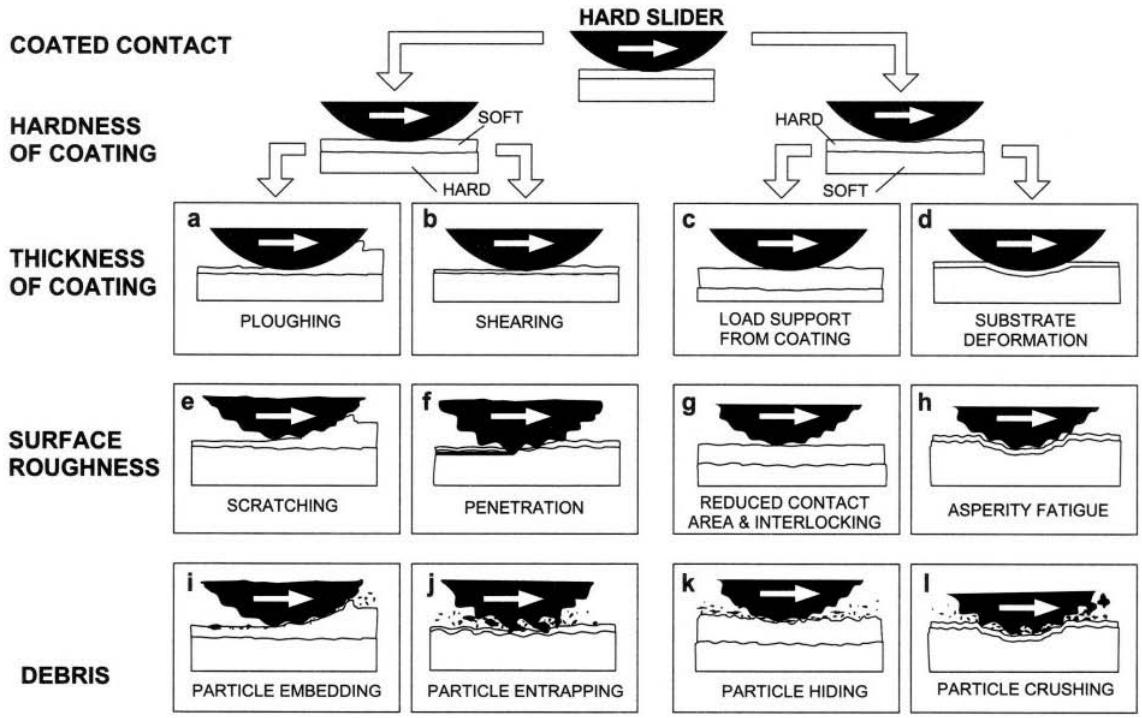

Figure 2.8: Macromechanical contact conditions for different sliding mechanisms which influence friction when a hard spherical slider moves on a smooth coated surface [Ho00a].

The friction coefficient will be small due the reduced contact areas (decreased adhesion) and increases with higher roughness of both surfaces because mechanisms of asperity interlocking and breaking respectively can be seen. For a hard slider moving on a soft substrate, covered by a thin hard film, elastic and/or plastic deformation will take place (Fig. 2.8h). Roughness increases the asperity contacts and generates pronounced fatigue because of the repeated loading by the moving counterface.

The fourth important factor for friction behaviour is the existence of debris. Wear particles get embedded into a coating, when the particle hardness is much higher than the film hardness and their size considerable smaller than film thickness. In this case no significant shift concerning friction behaviour can be found (Fig. 2.8i). With increasing particles size (same range or more than coating thickness), they will plough the coating and a formation of grooves will take place. At least this will result in an increased friction coefficient (Fig. 2.8j). On the other hand, for hard coatings and depending on the size of involved particles, different mechanisms can be observed. Small particles in the presence of hard and rough surfaces become hidden in the valleys of existing asperities and do not influence the friction behaviour. Consequently for smoother surfaces, debris affect a

chance in friction and an interaction takes place because particles can not be hidden in the valleys (Fig. 2.8k). Hard particles interacting with hard and smooth surfaces can act as rollers and may decrease the friction coefficient, whereas particles with a lower hardness get crushed and the formation of a new top layer takes place (Fig. 2.8l).

Typical wear mechanism of coatings and their interaction with counterbodies can be discussed in the same manner. Eight mechanisms are found and will be illustrated in Fig. 2.9 [Ho94,Ho01,Ho98,Ho00a].

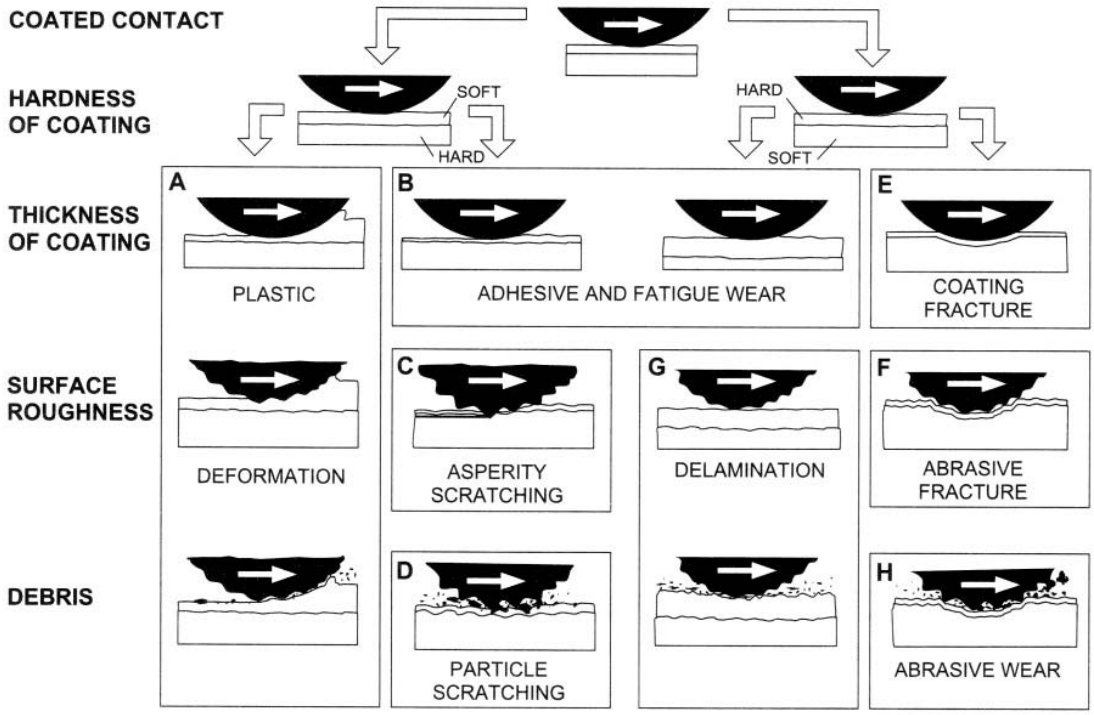

Figure 2.9: Macromechanical contact conditions for different sliding mechanisms which influence wear when a hard spherical slider moves on a coated surface [Ho00a].

Plastic deformation and grooving of the coating can be obtained for hard sliders moving on a thick hard coating. The higher the surface roughness, the more pronounced formation of microgrooves and microploughing is supposable (Fig. 2.9a). In the case of a thick hard coating, or a hard substrate covered with a thin soft film, contacting a hard counterbody, adhesive wear takes place (Fig. 2.9b). Increasing thickness of the soft film results in a decrease in load-carrying capacity due to the increased area of contact. Coating penetration or sliding on the substrate can be found for rough surfaces sliding on a hard substrate covered with a soft film (Fig. 2.9c). A decrease of film thickness can be seen in the first stage due plastic deformation and adhesive wear. An increase of wear can be achieved when asperities get in contact with the substrate material. This is based on the effect of scratching and adhesive wear occurring for that case. In Fig. 2.9d particle scratching and microploughing of both the film and the substrate can be noticed for hard and large particles in the contact between a soft thin rough coating and a hard rough

counterbody. In this case, debris is caught in the surface roughness. On the other hand, the appearance soft particles may enable a decrease of friction and wear due their load-carrying capacity and reduced areas of contact. For thin hard films to be applied for wear protection, the substrate must be hard enough to carry the load and to avoid elastic and/or plastic deformation in the substrate while in contact (Fig. 2.9e). Increasing substrate hardness results in increased load carrying capacity. Thick protective coatings are able to carry higher loads compared with thin films due to their elevated stiffness. On the other hand, thick coatings are more brittle because of their higher stresses. When a hard rough slider moves on a hard rough coating, a high tendency of asperity interlocking can be found (Fig. 2.9f). Smoothing of surface roughness and formation of sharp wear particles can be observed due to breaking of asperity tips and may result in changes of the tribological behaviour. For the same case but with smaller asperity angles, delamination may occur (Fig. 2.9g). A plastic deformation of the contacting asperity tips generates high stresses and yields dislocations, pile-up dislocations and crack nucleation below the surface. In Fig. 2.9h the mechanism of abrasive wear of a thin hard film can be seen. Large hard particles in the area of contact are scratching both surfaces and high pressure peaks on both surfaces induce cracks.

3 Physical vapor deposition

3.1 General

Since the discovery of current at around 1850 by M. Faraday and T.A. Edison, a wide variety of deposition techniques have been developed and are used nowadays in scientific and industrial applications to synthesize films. Concerning surface technology, the first relevant discovery was found in 1852 by Grove. He observed the deposition of cathode material onto the wall of glow-discharge tubes [Fr90,Gr52], and this effect was first used in 1877 by Wright for mirror production [Wr77]. In the thirties, Western Electric used this method for the first time for metallization of the waxed matrix of records [We70] and in the fourties, materials science and tool industries made full use of these new and further developed techniques for decorative, protecting, or optical uses [Fr90].

These techniques differ in several deposition parameters like the basis of the media of matter (solid, liquid, gaseous) [Ma96], material transport kinetics from the source to the substrate, particle state (atomic, ionic, clusters, and bulk), and particle energy. Additionally, other deposition parameters like substrate material and –temperature, deposition gases, working gas pressure, and bias voltage also influence the chemical composition, structure and properties of the synthesized films [Oh02,Pa03].

The preparation of wear resistant, hard, ceramic based coatings is mainly performed with chemical vapor deposition (CVD) and physical vapor deposition (PVD) techniques [Ho89a,Kn97,Ma96]. The former are based on chemical reactions of gaseous precursors in the vapour phase at working pressures of ~ 0.01 to 1 bar and temperatures between ~ 300 and 2000°C depending on the used CVD technique (exceptions are the deposition of BN and TiO_2 at room temperature) [Ga91a]. The activation energy to enable these reactions can be obtained by heat, plasma energy, and for more reactive species by UV light. Despite several advantages (as well as no size limitation for substrate geometries, good film adhesion and homogeneity, and high film density), there are a number of limitations for CVD processes, e.g. the high deposition temperature, the availability, thermal stability, and toxicity of precursor gases and the small number of types of reactions (main reactions are chemosynthesis, pyrolysis and disproportion) [Ei01,Ho89a]. In PVD processes, materials which form coatings are generated by vaporizing, i.e. no chemical reactions have to take place. All PVD processes base on three major techniques, i.e. sputtering, evaporation and ion plating of a solid or liquid material [Ba00,Ho89a]. Furthermore, additional elements or compounds can be introduced in the coating material via reactive gases like O_2, N_2, CH_4, C_2H_2, or H_2S [Ba00,Mo94,Su86]. These gases are able to form oxides, nitrides, carbides or sulfides. In contrast to CVD, PVD processes are very versatile due to the possibility of deposition of any metals and their alloys as well as organic materials and polymers. Furthermore, the deposition temperature can be varied between ~ 100°C and 800°C or more (depending on the

particular deposition system) and these features promote the use of PVD processes for several industrial applications [Sm99].

In general, PVD techniques are always processes operating in vacuum and contain the transition from a condensed phase (liquid or solid) to the vapour phase [Ba00]. The particular process steps can be divided into:

- Vaporisation of a source material (if the source is solid, it is called target)
- Transport of the vapor material between the source and the substrate
- Condensation and adsorption onto the surface of the substrate followed by nucleation and film growth

During the transport of vapor material (or species) from the source to the substrate surface, collisions may occur. To avoid or minimize these collisions during the transport of the vaporized source material, the processes normally take place in vacuum (with a mean free path of around 500 mm at 10^{-2} Pa and 12 mm at 0.4 Pa, respectively [Fr90]). Despite of this, the vacuum is also necessary to avoid involuntary reactions. Furthermore, for reactive deposition techniques (reaction between vaporized material and an active gas species like N, O, or S), reactions have to take place on the substrate surface due to the chemical inertness of the built reaction products. Otherwise, if the built components arise on the substrate surface in an inert atmosphere, these processes are named non-reactive processes [Ho89a].

For coating deposition, two PVD techniques are most established for industrial applications. They will be discussed in the following chapters and the can be classified as:

- Evaporation
- Sputtering

3.2 Evaporation

In evaporation processes, vapors are generated from a material source (solid or liquid) which is heated. The source material melts, vaporizes and is transferred as atoms or clusters to the substrate, crossing the vacuum chamber. On the surface of the substrate, condensation and film formation takes place by release of energy. Nowadays, several heat sources for evaporation are used like resistance and induction heating, laser, arc, or electron beam. Thereby the produced “steam flow” mainly consists of particles with neutral electric charges, whereas the origin of ions or charged particles is less pronounced (except for arc evaporation). With classical methods (resistance or induction heating), high deposition rates can be achieved in comparison to sputter processes [Bu00,Me01].

Transition of solid or liquid material sources into the vapour phase is based on thermodynamics and therefore consequently an atomistic phenomena. Due to the

presence of a vacuum (to attain an acceptable free path way of around 1 – 10^7 cm), thermodynamic and kinetic material characteristics like melting – and boiling point as well as vapor pressure are determining factors for this technique. The theoretical maximum rate of evaporation can be calculated by the Hertz-Knudsen equation,

$$\frac{dN_e}{A_e}\,dt = \alpha_v N(2\pi m k_B T)^{-1/2}(P^* - P) \qquad \textbf{(3.1)}$$

where $dN_e/A_e\,dt$ is the number of molecules evaporating from a surface area A_e in time dt, α_v is the evaporation coefficient, N is the Avogardo number, m is the molecular weight, k_B is the Boltzmann´s constant, T is the absolute temperature, P^* is the equilibrium vapour pressure at the evaporated surface, and P is the hydrostatic pressure acting on the surface. α_v, the coefficient of evaporation, is very dependant on the evaporate surface cleanliness and increases with higher impurity level [Bu00].

Deposition of alloys by evaporation is a common way to generate films, whereas simultaneous deposition of films consisting of several metals from separated crucibles is more advanced due to different vapor pressures of these materials and resultant evaporation rates.

3.2.1 Evaporation by resistance heating

Owing to the simple construction and high deposition rates, thermal evaporation by resistance (and induction) is a widespread technique used today, e.g. for deposition of aluminium for reflector coatings. Geometries for vapour sources are mainly resistance-heated wires (wire helix, wire basket) or metal foils like dimpled foils or dimpled foils with an alumina coating. For non heat-resistance materials like polymers, an installation of a shielding cover can be used. A representation of such a construction can be seen in Fig. 3.1.

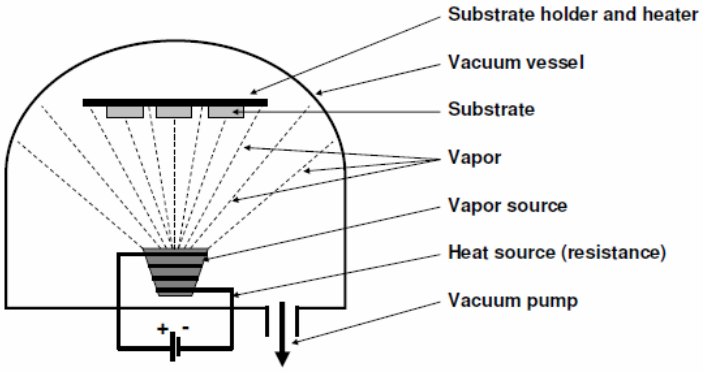

Figure 3.1: Schematic representation of a configuration for evaporation by resistance heating (modified) [Me01].

Two kinds of problems associated with the process mainly appear by evaporation with resistance (but also for induction). Due to the melting of the evaporation source within a crucible, reactions between these two materials can occur. Therefore the contact area

between the source crucible and the evaporant has to be held at a minimum. Furthermore metal oxides used for crucible materials like alumina or magnesia are less reactive than e.g. Pt, Fe, or Mo. High working temperatures additionally increase these phenomena. Furthermore, limitations can be noticed in the geometry of the construction. Due to the originating “pool”, deposition only works in the bottom-up direction [Bu00,Me01].

3.2.2 Electron beam assisted deposition

In electron beam assisted evaporation (EBAD), energy required for heating of evaporants is supplied by acceleration and focusing of an electron beam. To avoid contamination of the electron source with evaporation material, the electron beam mostly is side-mounted outside the vapour volume. The electron beam, generated by a hot cathode, is focused onto the evaporant (used as anode) or by means of electric and/or magnetic fields. For more complex constructions, an anode is placed close to the cathode and after leaving of electrons from the cathode surface, these electrons become accelerated by the potential difference, pass through a hole in the anode and impact on the evaporation material [Bu00,Fr90,Me01].

One mayor benefit of this technique is the very high power density, and hence, the wide range of control over evaporation rates from very low to very high. EBAD is very applicable for deposition of films containing refractory metals like W, Mo, and Ti. Furthermore high-melting, but non-conductive materials like alumina can be evaporated with this method. For crucible materials, ceramics and graphite will be taken. On the other hand, also copper can be used (in this case, the crucible has to be water-cooled to avoid impurities). Electron beam guns can be subdivided into two main types (thermionic and plasma guns) depending on the source of electrons, but many variations are known like diverse shielded filaments, transverse electron beam guns, cold cathode plasma electron guns, hot hollow cathode discharge beam guns, or RF hollow cathode low voltage electron beam guns [Bu00,Fr90,Me01].

3.2.3 Arc evaporation

Arc evaporation is a special case among all evaporation techniques and is one of the most widespread technologies for preparation of hard coatings. For example, one of the first industrial applications was for preparation of TiN coatings, particularly for high speed steel cutting tools [Bu00,Su85]. The basic principle for this application is the use of a glow discharge on the surface of the target, whereby this target can be switched either as cathode or as anode in the presence of an inert gas as well as reactive gas. The inner wall of the plant acts as counter-electrode. Nowadays, cathodic arc evaporation for preparation of hard coating is more common than the anodic way and has a lot of similarities with the sputtering process.

The initiated arc does not exist above the whole target material, but rather for a short period of around 5 till 40 ns onto a microscopic area (spot) with a diameter of only a few

microns. After this period, a new spot will be founded at the most energetically advantageous point in the next to the old spot, once again for only a few nanoseconds. At technical arc discharges with very high currents (-100 A or more) and power densities (10^7-10^9 W/cm^2), the evaporated material from the spot zone is almost totally ionised and forms a plasma flow moving to the substrate (see also chap. 3.3.1) [Jü87]. However, in the close proximity to the spot due to the high power densities, secondary particles with greater diameters get generated and also accelerated to the substrate. The particle size depends on process parameters as well as properties of the target material and leads to coating inhomogeneity and surface roughness. These defects are called droplets. Such particles can be reduced or nearly avoided with an adequate reactive gas or the use of traps and deflectors for the plasma flow. The direction of movement of the spot can be controlled with application of magnetic fields and is known as “steered arc evaporation” in contrast to “random arc evaporation”. As a result of the high energy input to a small area, no large-area melting pools create and allow evaporation in any position (see Fig. 3.2, with a schematic construction with typical components used for film deposition like vacuum pump, cooling units, arc rectifier, electrodes, and targets positioned vertically). Films deposited with cathodic arc evaporation exhibit good adhesion to the substrate and high film densities [Bo92,Bu00,Me01,Jü87].

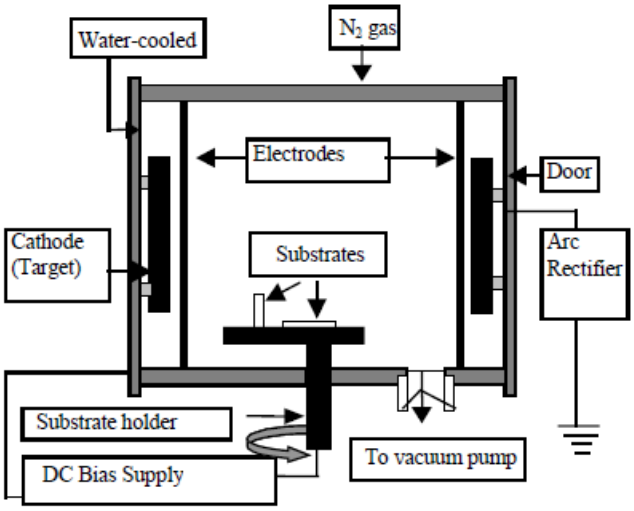

Figure 3.2: Schematic diagram of the cathodic arc evaporation (CAE) technique [Mu05].

3.2.4 Pulsed laser deposition

In the early 1960s, when first pulsed ruby lasers were available, a new way for deposition of thin films has been entrenched by employing laser radiation. This new technology, also called laser induced evaporation (LIE), or laser ablation, is nowadays used extensively for preparation of coatings utilized for electronic applications, e.g. compound semiconductor epitaxial layers, highly crystalline dielectric films or layers for bandgap engineering, or high T_c superconducting films like YBCO ($YBa_2Cu_3O_{7-x}$) [As04,Bu00,Ki95]. As illustrated in Fig.

3.3, an apparatus for pulsed laser deposition can be constructed without great expense and complexity. In a deposition vessel, the output of a laser is focused onto the surface of a rotating target in a vacuum or in presence of a background gas. Rotating or rastering of the target avoids renewed ablation from the same zone of the target and a higher yield of target material. The substrate is mounted diagonally opposite. The laser beam focused by a lens, and crossing a window (which transmits the wavelength band of the laser), impacts onto the target and evaporates material to the substrate. In general, every laser can be used for deposition, but most commonly the output wavelength ranges from the mid infrared (CO_2 laser with 10.6 µm), through the visible (Nd-YAG laser with 532 and 1064 nm respectively) and down to the UV, for example by excimer lasers (308 nm for XeCl, 193 nm for ArF or 157 nm for F_2). On the other hand, it is not always possible to find a laser with output wavelength compatible with the absorption characteristics of the evaporated target material, and the energy conversion efficiency is with around 1 – 2 % very low. Furthermore, the performance of deposition is also influenced by durations and sequences of the pulse [As04,Ki95].

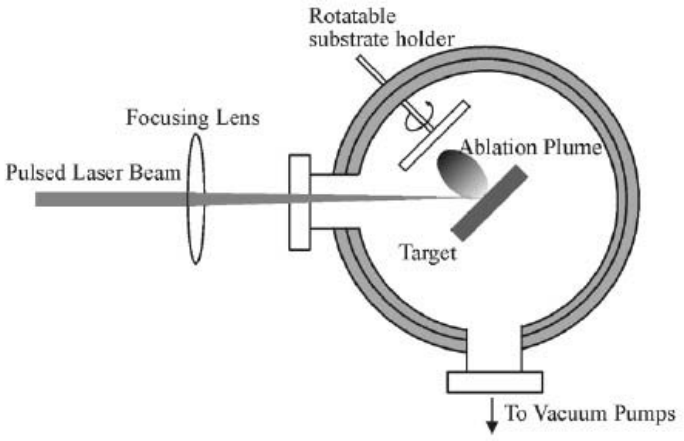

Figure 3.3: Schematic construction of an apparatus for pulsed laser deposition [As04].

3.3 Sputtering

3.3.1 Plasma

3.3.1.1 General

Based on his investigations in gases, generated by tungsten-filament light bulbs, the term was first coined in physics and chemistry by I. Langmuir. A plasma (from the greek word *πλασμα*, which can be translated as “moldable substance”) can be described as a largely ionized gas, containing an equal number of negative (electrons) and positive (cations) charges, but also any number of neutral atoms and/or molecules. Due to this ionized condition, plasma has electro-conductivity and can be influenced by eternal electric and magnetic fields. On the other hand, because of the same number of opposite charges, the

plasma, observed from an outward point, is in a neutral state (also called quasineutral). Although, plasma is not comparable to a normal gas which accords with the kinetic gas theory, some analogies can be found. In ideal plasmas, no preferential directions of particle motion occur, but these particles move with statistically distributed random speed and different directions, corresponding to the Coulomb interactions within the field. The energy input (W) to the plasma can be calculated by equation 3.2:

$$W = \frac{(e_0 E t)^2}{2m} \qquad \textbf{(3.2)}$$

with an acceleration a (a =e_0E/m), where e_0 is the elementary charge, E is the energy, t is the time, and m is the particle mass. Thus it appears that the energy input is transferred nearly full to the electrons due to their small weight, whereas the heavy particles (ions and neutral gaseous components) are hardly accelerated. Electron energy can reach for sputter deposition up to a few eV (~ 2-7 eV). Converting this kinetic energy (according to the Maxwell-Boltzmann theory) into temperature, where 1 eV = ~ 11600 K, average temperatures far beyond 20000 K can be assumed. Because of enormous different masses of the charged particles (m_e « m_i), a transfer of kinetic energy by elastic collisions is negligible. Therefore, the assumed temperature for ions and neutral particles is in the range of room temperature (≤ 0.1 eV). In that case, based on different thermodynamic behaviour of electrons, ions and neutral particles, plasma processes are never in thermodynamic equilibrium, where temperature and pressure is uniformly distributed. For argon plasmas, the current density of the electrons compared to the ions and neutral particles differs by a factor of around 10^3. Additionally, a broad speed (thermal, energy) distribution of the electrons can be observed due to the little number of inter-electronic collisions (n_{iec}). Increasing of the gas pressure (p_g) decreases the number of inter-electronic collisions (n_{iec} ~ $(p_g)^2$), and results in a contraction and shift to higher values of the energy distribution (called “hot plasma”). For that reason, a subdivision into “cold plasmas” and “hot plasmas”, or low-pressure plasmas (p < ~ 1 bar and a charge density of around 10^9 to 10^{12}/cm^3) and high-pressure plasmas, respectively, can be found in literature. Low-pressure plasmas can only exist in a small range, because undersized plasma densities result in a separation of charges due to missing electrostatic interactions, and increasing of plasma density yields in gas heating. Cold plasma generation and sustainment, as used for sputter deposition, normally is done by employing direct current (DC), microwave, and radio frequency (RF) for forming electric glow discharges [Ch80,Fr94,Go98,Gr94,Ha87,Mu99,Ra97].

3.3.1.2 Glow discharge

Electric glow discharges can be defined as transport reactions of charged particles (electrons and cations) within a gas phase and simultaneous origin of emission (the typical colour depends on the gas properties). This term implies the formation, movement,

and recombination of charged gaseous particles between an anode and cathode in the presence of electric and magnetic fields. In deposition technologies, a common way to achieve this effect is in ionisation of neutral gas particles by an inelastic impact of electrons.

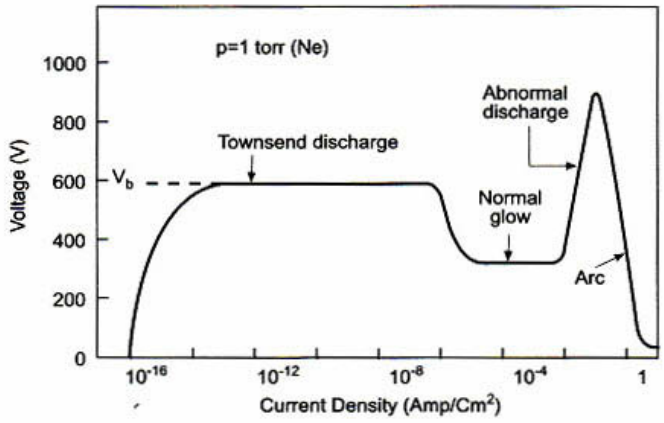

Figure 3.4: The I-V characteristic of a DC glow discharge [Gr94]

The different steps of forming a glow discharge as a function of voltage can be classified into four states, described by a voltage vs. current curve (as seen in Fig. 3.4). Even without an applied voltage, a small number of free electrons always are present because of natural radioactivity and cosmic radiation, or generated by field emission or photo ionization. After applying of a potential to the gas, these electrons become accelerated in the electric field and gain kinetic energy.

This acceleration continues till reaching a critical level, where the electrons are able to ionize neutral gas particles by inelastic collisions and produce themselves new electrons. This multiplication and acceleration of electrons in turn takes place until a steady state is reached. In this situation, the number of new originated electrons complies with the number of electrons, which are withdrawn by recombination processes as well as chamber wall reactions. In contrast, the cations are accelerated to the cathode and affect emission of secondary electrons by impacting. These secondary electrons speed up towards the anode and the following collisions with neutral particles result in formation of new electrons and cations. If the charge formation and recombination of both processes reach equilibrium, a Townsend or dark discharge can be obtained and is self-substaining [Ch80,Ha87,Gr94,Mu99,Ra97].

A sudden increase of current and decrease of voltage along with an occurrence of normal glow discharge is caused by further enhancement of power. Ion impact onto the cathode and emitted secondary electrons are the mainspring for sustainment of the plasma. The yield of secondary electrons (ratio between the amount of generated secondary electrons and the amount of impacting cations) has to be in the range of around 0,1, that means, a

secondary electron has to ionize approximately 10 – 20 neutral particles. At the same time, the discharge area onto the cathode enlarges from the initial zone close to the rim up to the complete target area to enable the constant current density required. After complete cathode area coverage, a rise of voltage and current density up to the abnormal discharge regime can be detected and this region is typically used for sputter deposition. Particle emission (atoms and molecules with altogether weakly ionisation) takes place due to the impact of generated high-energy cations and transfer of their kinetic energy to the target surface. As a helpful value for quantification of deposition conditions and material properties, respectively, the sputter yield (ratio between impacting ions and ejected atoms) is well-established in literature. Furthermore, these impacts and energy transfers result in a temperature rise of the target and can effect thermionic emission. Further increase of power leads to the formation of arcs with highly ionized particles and can be used for arc deposition techniques (cp. chap.3.2.3) [Ch80,Ha87,Gr94,Mu99,Ra97].

3.3.2 Glow discharge sputtering

Sputter deposition is characterised by acceleration of high-energy inert gas ions (plasma, see chap. 3.3.1 for a more detailed explanation) onto the surface of a target and the ejection of particles to the space (and substrate) above. The target material becomes eroded by these impinging ions due to an energy (pulse) transfer and the hence resulting consequential collision cascade, and neutral particles (predominant atoms, clusters, or molecules) as well as secondary electrons are emitted. The energy source, required to maintain the plasma state, can be provided by DC, radio frequency, or microwave. This deposition process will be realized normally by applying of a high voltage to an inert gas atmosphere (Ar) with a working pressure of around 10^{-3} Pa, positioned above a plane target, and results in a glow discharge and plasma formation. Positively charged ions (Ar^{+}) from the plasma get accelerated to the target, connected as a cathode (by a negative voltage supply). This process is based on the potential difference, and affects target erosion and particle emission. A schematic DC sputtering array is shown in Figure 3.5 [Ba00,Bu00,Fr90,Me01].

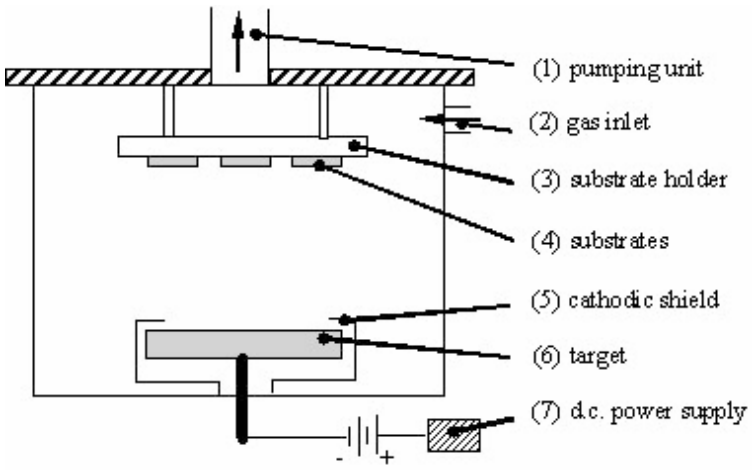

Figure 3.5: Schematic construction of an apparatus for sputter deposition [Ku05].

For perpendicular ion incidence, target erosion rate R and sputter yield S can be calculated with:

$$R = 62.3\frac{JSM_A}{\rho} \quad \textbf{(3.3)}$$

where J is the ion current density, S is the sputter yield in atoms/ion, M_A is the atomic weight, and ρ is the target density, and

$$S = \sim \frac{E_j}{U}\frac{M_i M_j}{(M_i + M_j)^2} \quad \textbf{(3.4)}$$

where M_i is the mass of incident atoms, M_j is the mass of the target atoms, E_j is the kinetic energy of incident ions, and U is the heat of sublimation of the target material [Bu00].

For common sputter constructions, higher deposition rates can be achieved by employment of added permanent magnets behind the target (magnetron sputtering), compared to older and more simple constructions (glow discharge sputtering) [Ba00,Bu00,Fr90,Me01].

3.3.3 Magnetron sputtering

Magnetrons, originally developed for the generation of high frequencies, are also used nowadays to enhance sputter deposition. Magnetic fields produce a force on the electrons (ions are too massive), leading to an acceleration, which results in a higher sputter yield due to higher plasma ionisation. With increasing of the path way of electrons by using magnetrons, their recombination at vacuum chamber walls (anode) is hindered. In other words, an axial magnetic field changes the direction of the electrons into a helical motion and reduces the velocity towards the walls, where recombination takes place, and leads to a higher ionisation. These electric and magnetic fields, generated by the magnetron (perpendicular and parallel to the target, respectively) act as an electron trap close to the target surface [Ch80,Ch84,Ha87,Li94].

For applied sputter techniques, several types of magnetron arrangements can be classified: e.g. planar, linear, cylindrical, and circular, whereas the first one was used for coating deposition within this thesis, and is itself a general term for specific adjustments. A distinguishing mark for planar magnetrons is the formation of an erosion zone, looking like a racetrack, due to looping magnetic fields and their indirect interaction to cations (Fig. 3.6). Based on magnetic and electric constrictions of electrons close to the target, a transverse electron flux with increased cation formation and higher deposition rates at lower working gas pressures can be achieved. On the other hand, this also results in higher target temperatures and is the reason, why the targets have to be cooled while deposition [Ch80,Es93].

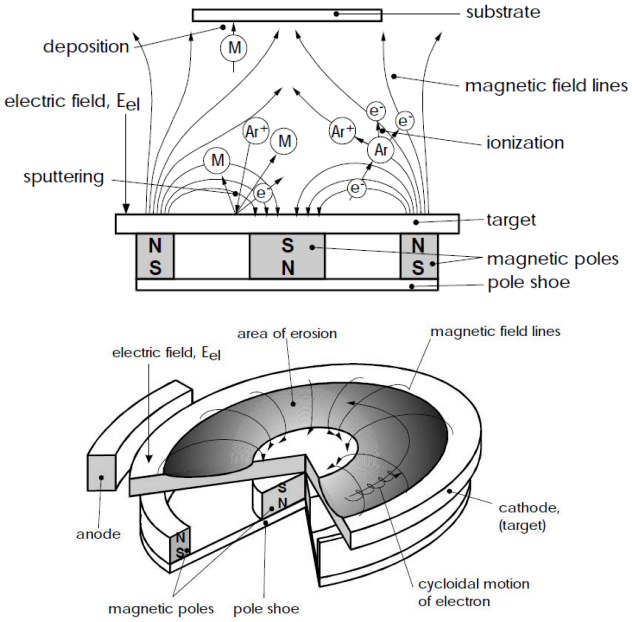

Figure 3.6: Schematic representation of a **(a,** above**)** planar circular magnetron configuration [Ha87,Ch80] and **(b,** below**)** unbalanced magnetron (UBM) configuration [Ga91b,Sp91].

As mentioned before, the planar magnetron configuration is a general term and can be subdivided into two subcategories. For an ideal case, the inner and outer magnets balance each other and the magnetic field line loops between them (conventional balanced magnetron - CBM) (see Fig 3.6a). There, ion bombardment onto the substrate surface while film growth is negligible, because the magnetic field confines the discharge in close vicinity to the target. With a transposition of magnets, or use of stronger inner or outer magnets, an ion flux to the substrate can be obtained due to the changed magnetic field configuration. This ion bombardment can change the properties of the growing film and has its technical counterpart in the unbalanced magnetron configuration (UBM) (see Fig. 3.6b). Here, the advantages of both processes (normal deposition behaviour and ion bombardment of the growing film with energies in the range of a few eV) can be combined.

Another way to achieve such deposition conditions can be put in practice by applying different potentials to the substrate (bias voltage). In that case, fast secondary electrons, escaped from the cathode, follow the magnetic field lines and move away from target. Collisions with neutral gas atoms cause ionisation and hence, the plasma is not narrowed to the target surface anymore, and expands away. Adjustment of the magnetic fields determines the number of generated ions and allows the variation of plasma density near to the substrate surface. For biased substrates, the energy of the impacting cations can be controlled by a potential difference between the plasma and the substrates [Ga91b,Iv94,Sp91,Wi86,Wi96].

As mentioned in previous chapters, for sputtering processes, a working gas atmosphere is indispensable. Depending on the type of gas atmosphere (inert gas like Ar, or reactive gases), a classification in categories can be found.

3.3.3.1 Non-reactive magnetron sputtering

For films, deposited from metals and metal alloys with different deposition rates in an inert gas atmosphere like Ar, the chemical composition is almost identical to the target composition. However, it is also possible to sputter non-metallic target materials (ceramics, multicomponent targets). For multicomponent targets, deposited for the first time, the component with the highest sputtering rate is removed strongest and quickest and leaves a modified surface composition with different sputtering rates. Equilibrium can be obtained, when the sputtering rate conforms to the availability (because of depletion) of all compounds participating. After reaching this stable state, the chemical composition of the formed film matches with the target composition [Ke99,Lo97a,Mi95,Mi96,Mi98a,Wa95].

For exceptional cases, where the chemical composition of both, the target and the grown film, disaccord, several mechanism or their combination are known: (1) Besides diffusion processes within the surface-near target area and evaporation of target material, additionally sublimation (significant vapour pressure of the particular compound) may take place which is due to too high target temperatures. (2) Contaminations on the target surface change the chemical composition and thus the sputtering rate. This case can often be observed in the presence of N_2 or O_2. The last one is more critical because an oxidation of the target surface changes the sputtering rate to them of oxides, where reduction never takes place. This effect can be seen for unclean working conditions or in the presence of leakage. (3) A notable re-sputtering effect occurs on the substrate during film formation and changes the chemical composition compared with the target material. For unbalanced magnetron configurations with an applied bias voltage to the substrate, the impacting cations foster re-sputtering. As a rule of thumb, materials with high sputtering rates and big atom radii are more dedicated for re-sputtering. With enlarged atom radii, the probability of ion impacts is increased [Ma83].

3.3.3.2 Reactive magnetron sputtering

Ceramic-like materials like carbides, nitrides or oxides, deposited with sputter techniques, can be generated by adding reactive gaseous components (CH_4 or C_2H_2, N_2, H_2S, or O_2, respectively) to the inert gas within the deposition chamber during deposition. Reactive species are generated in the presence of the plasma and contribute actively either in the gas phase or on solid surfaces (chamber wall, target and substrates) to the film formation. At low gas pressures, used normally for sputtering, the collision cross-sections are quite small, and therefore the reaction efficiency is very low. Furthermore, the deposition rate generally decreases by increment of the flow rate of the reactive gas, or rather its partial

pressure. This effect is called target poisoning and is based on the formation of compounds, fully covering the sputtering area, with a smaller deposition rate. The markedness of this process depends on the specific properties of the layer, originated on the target surface, and the chemical affinity of the participating compounds. A change in the discharge conditions and emission of secondary electrons, compared to the not-poisoned target surface, can be defined as reasons for this behaviour [Ma83].

Massive poisoning can be obtained for Al, Cr, or other metals, which are sputtered in an oxygen containing atmosphere, and which are able to form highly stable metal oxides. This effect is less pronounced for other common reactive gases like N_2 or C_2H_2. High deposition rates can be achieved by injection of the reactive gas close to the substrate. Hereby, both the disposability of reactive species for reactions reach the highest level and target poisoning is significantly prevented due to the large distance to the target. Further increase in substrate reactivity can be maintained by an approach of the plasma to the substrate surface, because charged particle bombardment elevates the dissociation of gaseous molecules [Ma89,Bu85].

3.4 Nucleation and film growth

3.4.1 General

The specific behaviour of materials is determined by their chemical composition, microstructure, and morphology. In thin film technology, especially for materials deposited with techniques based on the condensation of vapour phases, material properties are also strongly associated to the processes of formation. Therefore, the material specifics of coatings can not be compared with common bulk properties of an identical composition. They differ strongly e.g. in their grain size and microstructure, residual stresses or can even reach a metastable state. With variation of deposition parameters like substrate temperature, bias voltage, plasma adjustment, or presence and partial pressure of an involved reactive gas, the mechanism of film formation can be influenced and as a consequence the material properties [Ne83].

Usually, coating and substrate materials differ in their chemical composition and thus in their bonding nature. This is the reason, why particles from the vapour phase cannot condense instantaneously on the substrate surface, because an equal chemical nature is required. Consequently, for film formation, only condensation reactions on surfaces take place, i.e. combination of atoms by adhesion to small clusters, also called nuclei. This mechanism is termed nucleation and their accumulation building up closed layers is called growth of the film. Both mechanism can occur simultaneously [Ma83,Ri87].

As a general rule, the procedure of steps forming a continuous film can be classified as nucleation, crystal growth and segregation of impurities, caused by the deposition process. At first, the origin of adsorbed monomers and formation of subcritical embryos with various sizes take place until nuclei with critical sizes are formed. Additional growth

up to supercritical dimensions leads to depletion of monomers in the capture zone around them. At the same time, a procedure of step repetition in areas not depleted of monomers passes. In the next step clusters contact each other and coalesce under formation of new islands. Those islands occupy an area smaller than the sum to the original two and release fresh substrate surface. Monomers adsorb on these freshly released areas and this leads to “secondary” nucleation. After that, large islands grow together and leave holes and/or channels of released substrate surface. They are filled by “secondary” nucleation and give a continuous film. Furthermore, crystal growth, initiated by coalescence of individual crystals on the substrate and grain boundary migration in the polycrystalline structure, can be maintained. Additionally, process based segregation of impurities while crystal growth can be observed. Here, an impurity phase on the crystal surfaces is built and also takes place during grain boundary migration. Both effects elevate the impurity content of grain boundaries [Ba97,Ba98,Gr93,Ne83].

Nucleation and growth are mainly influenced by critical material and process values like substrate surface behaviour, geometrical configuration of target and substrate or compatibility of the substrate/film system. Both mechanisms are controlled by substrate temperature, which is responsible for epitaxial diffusion and re-evaporation, and arrival rate of atoms on the surface. For an impinging atom from the gas phase, two initial interactions with the substrate can be defined. Either they get adsorbed on the surface with a transfer of their kinetic energy to the lattice and become bonded weakly, or reflected to the space. Theses **ad**sorbed **atoms** (thus called **adatoms**) can diffuse a certain distance till the get desorbed (or re-evaporated) again or they get caught at low-energy lattice sites. A balance between ad- and desorption of adatoms can be observed for small impinging rates and a non-compliance of the critical number of particles, necessary for nucleation. Increasing of arrival rate promotes the formation of stable and metastable clusters. They may enlarge by incorporation of particles from the vapour phase or by diffusing and/or binding adatoms. At high supersaturations, two or three atoms can suffice to establish a stable nucleus. An enlargement of cluster size increases the probability of contact and a network of connected clusters is generated by coalescence and leads to the formation of dense films. Additionally, Oswald ripening, where particular adatoms diffuse from smaller to larger nuclei, supports the film growth [Ve75]. A schematic summarization of these mechanisms can be seen in Fig. 3.7.

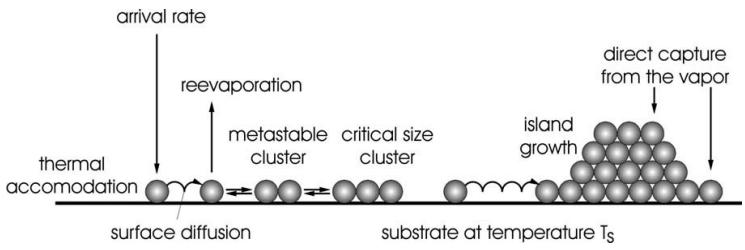

Figure 3.7: Representation of nucleation and growth processes on a substrate [Gr93,Ro92a,Ve75].

Three different models of nucleation and film growth are known for high temperatures and low deposition rates. The preferred mode depends on the type of predominant binding energy and determines the atomistic growth. They can be subdivided into: (1) the adsorption energy at the surface (2) the energy between adatoms and (3) the binding energy on the top of an adsorbed layer [Gr93,Je92].

The mechanism of layer growth (Frank-van der Merwe) can be observed for the case, that the energy between the adatoms and the substrate is most prevailing, thus a 2-dimensional surface covering is preferred (Fig. 3.8a). In diametrical opposition to the first one, a process of island growth (Volmer-Weber) can occur. Small clusters are nucleated straight on the substrate surface as a result of higher binding energies between the adatoms than those to the surface. A dense film is generated by coalescence of these cluster islands (Fig. 3.8b). The third epitaxial way of covering is termed layer plus island growth or Stranski-Krastanow growth (Fig. 3.8c). This intermediate formation process is a combination of both 2- and 3-dimensional island growths. Conversion of a layer-by-layer to an island-based growth happens at a critical layer thickness which mainly depends on the chemical and physical properties of the film and substrate, like surface energy or lattice parameters [Gr93,Je92].

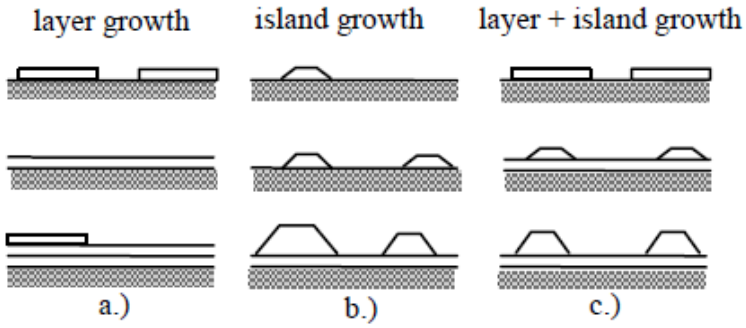

Figure 3.8: Representation of nucleation and growth processes after **(a)** Frank-van der Merwe, **(b)** Volmer-Weber, and **(c)** Stranski-Kastranov [Gr93,Je92].

These idealized mechanisms of covering originate in surfaces from perfect monocrystals and a random nucleation, but do not include impurities, vicinal surface steps, or surface defects. For example, ion bombardment of the surface, which is used for several applications like sputter cleaning or high energetic ion deposition or artificially generated surface defects, can influence the kinetics dramatically. Generally, defects change the binding energy sites and can be proactive for attachment and incorporation of species on surfaces or in films. Adsorption sites can be generated by high energetic ion bombardment, as used for sputtering, by reason of an increased number of surface defects and result in more stable cluster and nuclei. Amorphous structures can be obtained often for ionic and covalent compounds, when adatoms are inhibited in their surface diffusion. They don't have the possibility to occupy low-energy sites and became covered by succeeding vapour particles. With enhanced adatom mobility, as with metals,

this effect narrows. The use of reactive gases and their adsorption to the substrate surface reduces the diffusion mobility of other adatoms and causes the same effect, mentioned before. Antithetically, if a bias voltage is applied and high energetic ion bombardment promote substrate heating and enhanced mobility, than higher nucleation rates and crystallinity occur [Gr93,Me84].

3.4.2 Structure and morphology models

As mentioned in the capture before, the coating properties and behaviour is decided by the kinetics of nucleation and growth. Furthermore deposition does not take place at conventional thermodynamic equilibrium, therefore, a higher number of defects like vacancies, dislocations or precipitates can be obtained, compared to bulk material. To understand the consequences of growth as well as the influences of deposition and process parameter to the morphology, structure zone models (SZM) were conceptualized. Some of these deposition parameters determining the SZM are:

- Geometry of deposition construction (angle of impinging particles, shadowing)
- Substrate temperature (surface adatom and bulk mobility and diffusion)
- Substrate pre-treatment (roughness, density of surface sites, adsorption area)
- Gas pressure (surface covering, target poisoning, scattering processes)
- Applied voltage (impinging rate, kinetic energy of impacts)
- Applied bias voltage (high energy bombardment during growth)

But also energetic (thermodynamic and kinetic) aspects of used materials like sublimation energy or activation energy for surface and bulk diffusion can be set into relation to coating structure. In particular, the substrate temperature during deposition (T_s) and the melting point of the used material (T_m), and their ratio (T_s/T_m), respectively, are of great interest. Thus, T_s/T_m is the basis of all models of SZM.

The first SZM was developed by Movchan *et al.* with three structure zones as a function against T_s/T_m and modified by Thornton with involvement of the sputtering gas (Ar) as third axis (Fig. 3.9a). In this case, Zone I grows with elevated Ar pressure at the expense of Zone T. Additionally, Messier *et al.* extended this SZM with the energy of the impinging ions in the form of the applied bias voltage (Fig. 3.9b). Here, Zone T expands to lower temperatures at the expense of Zone I due to increased mobility of the adatoms [Me84,Mo69,Th74,Th75,Th77].

Four zones can be classified:

Zone I is marked by tapered, porous crystallites, which are separated by voids, and a high density of lattice imperfections. The morphology is generated by continued nucleation of grains during film growth as a result of shadowing effects in combination with low adatom mobility. Increasing T_s/T_m ratio results in gain of the crystal diameter.

Zone T, the transition from Zone I to Zone II, is composed of a dense arrangement of tightly packet, fibrous grains and dense boundaries. For this zone, a relatively fine doomed and smooth surface can be observed and can mainly be obtained for low temperature sputter depositions. The small surface roughness is based in enhanced adatom mobility and the possibility to find suitable sites.

Zone II is structured by uniform columnar grains separated by distinct, dense, and intercrystalline boundaries. The determining process herby can be localised in the adatom diffusion and increasing of the T_s/T_m ratio enlarges the grain size.

Zone III consists of equiaxed grains with a bright surface, because the diameter of columnar grains of Zone II have widened by the dominating mechanism of bulk diffusion and recrystallisation.

Shadowing effects are mainly the determining mechanism for formation of Zone I and Zone T whereas surface and/or bulk diffusion are dominating film growth for Zone II and Zone III, respectively.

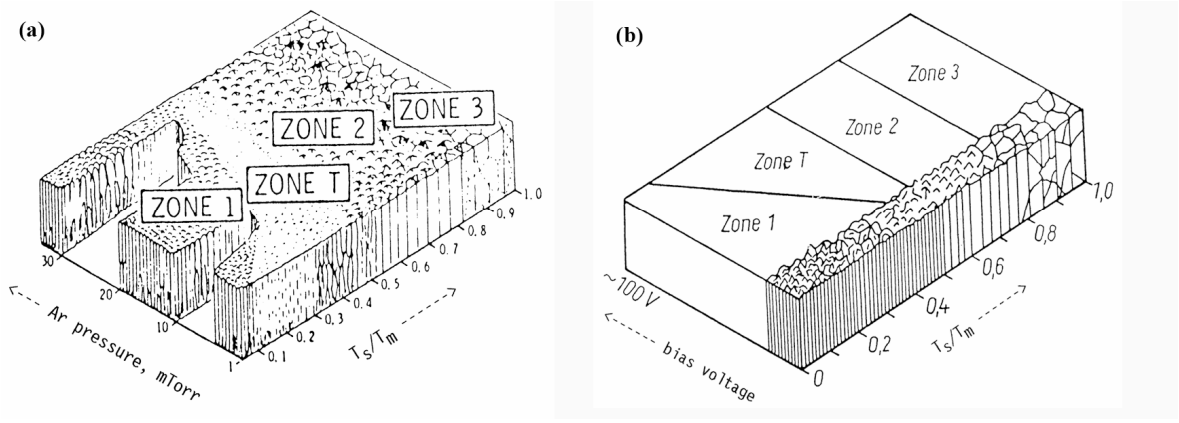

Figure 3.9: Structure zone model after **(a)** Thornton [Th74] and **(b)** Messier *et al.* [Me84].

In Fig. 3.10, some special SZM´s of films deposited at different conditions and their influence to the structure can be seen. Normally, film growth is started by formation of particular nuclei with different sizes. In the course of growth, the nuclei with the best prerequisites, depending on the process conditions, are preferred at the expanse of other nuclei. In Fig. 3.10a, a case without surface diffusion, i.e. every adatom keeps were it is adsorbed, and same condensing rates can be seen. Additionally, a normal coating flux with some side scattering is required. The first nuclei have a spherical geometry and a coating with a tight columnar morphology and a smooth surface can be obtained, corresponding to the Zone T structure. For the situation of zero surface diffusion but different condensing rates (and surface energies), and a normal coating flux, a Zone I structure is most likely. Based on preferred growth of crystal planes, the surface topography is rough and the morphology is open. This can be seen in Fig. 3.10b. Increasing temperature results in a Zone II structure with a smooth surface and a compact

morphology. Different condensation rates are compensated by higher diffusion rates, and therefore, the grains have a nearly identical growth rate (cp. Fig. 3.10c). The higher temperature also allows grain boundary mobility, bulk grain growth and adatom diffusion and is responsible for the dense structure. A structure, corresponding to Fig. 3.10d can be found for the case of random crystal nucleation on the top of growing crystal while film formation [Je92,Th77].

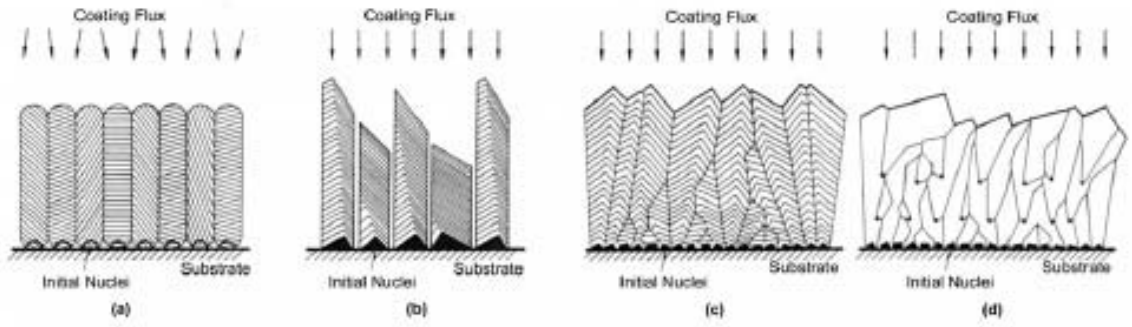

Figure 3.10: Structure development under various conditions [Th77].

In Fig. 3.11, the structure changes as a function of increasing T_s/T_m is shown. For Zone I ($T_s/T_m < 0.15$), the size of a critical nucleus is comparable to a single atom radius and the crystallite size for this structure is located in the nanoscaled range. For temperatures between $0.15 < T_s/T_m > 0.3$, grain boundaries of a single orientation are versatile and lead to the formation of favourable oriented grain boundaries and a bimodal grain size distribution. Increasing temperatures up to $T_s/T_m < 0.5$ results in mobility of all grain boundaries and formation of a Zone II structure. Provided that bulk grain growth and surface recrystallization can take place, a columnar structure can be obtained. At elevated temperatures above $T_s/T_m > 0.5$, the mobility of atoms leads to equiaxed grains, typical for a Zone III structure. Hereby, atoms migrate towards surface vacancies, became covered by succeeding vapour particles, and each initial grain carries on growth (this effect is important especially for multicomponent films). An illustration is given in Fig. 3.11.

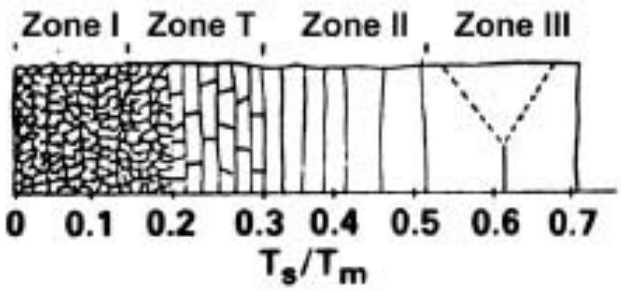

Figure 3.11: Modified SZM after Grovenor et al. with a film structure in the nanoscale regime in Zone I [Gr84].

Hugh changes can be obtained for incorporated contaminations or additional phase formation. The tendency of zone changes is reciprocal to the amount of contaminations

and a high number of impurities inhibits zone transformation, due to hindered diffusion processes. According to that, Zone I is delayed to higher temperatures at the expense of Zone T and Zone II, respectively. On the other hand, high amounts of incorporations stabilize Zone III even at low temperatures at the expense of Zone T and Zone II. As a special case, Zone I is neighboured by Zone III and a nanocrystalline morphology can be observed for both zones at low temperatures [Ba97,Gr84,Sm90].

Messier et al. suggested an influence of energetic particle bombardment to the coating structure. A shift of the boundary between Zone I and Zone T to lower T_s/T_m in combination with origin of lattice defects can be achieved by enhanced particle energy (Fig. 3.9b). Therefore, the use of ion bombardment while film growth is an effective way to enhance coating properties of films, deposited at low temperatures.

The interactions of energetic particle bombardment with a growing film are shown in Fig. 3.12a, and formed lattice defects are illustrated in Fig. 3.12b.

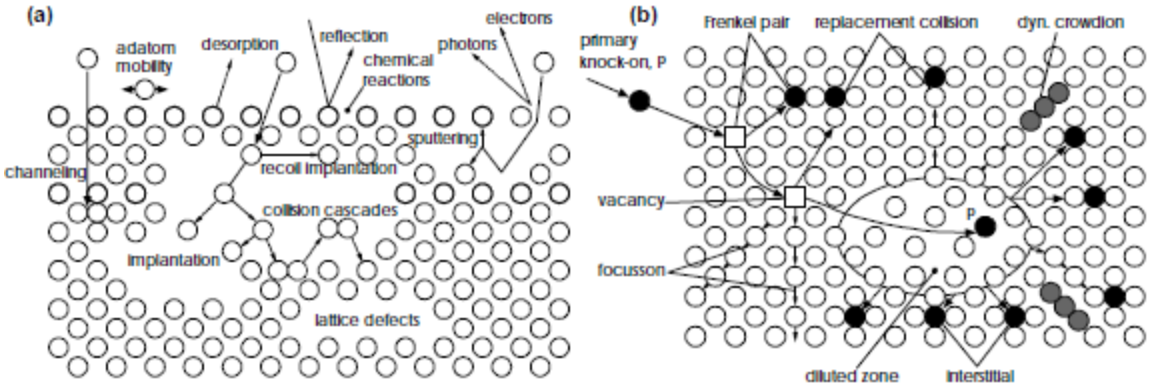

Figure 3.12: (a) Effects of ion bombardment on a growing film [En97,Ma89], **(b)** possible lattice defects created by an impinging energetic atom [Ha78].

Impacting atoms and ions with enough kinetic energy are able knock out atoms from their lattice positions. Secondary collisions take place which results in cascades of collisions. Contrary to high energetic bombardment, these collisions are not isotrop, i.e. the primary knock-on atom absorbs most of the energy. The powerful atomic motion along the trajectory of the ions affects a re-assembly of the crystal lattice. The impacting particles may also be physically implanted and but also surface species may be recoil implanted into the surface near lattice. If the energy of the particles, which are involved into the collision, is strong enough, the formation of lattice channels can occur [En97]. A higher number of vacancies and residual interstitials can be achieved by increasing the energy and flux of the impacting ions because atomic displacements are generated in the collision cascades (Fig. 3.12b). A row of atoms along a densely packed direction with an additional atom is termed crowdion, which is a line defect and a result of focusson. This array is able to move by exchange collisions. An extensive focussed transport of atoms takes place only for interstitial atoms, but not for vacancies. For this reason, the end of a displacement cascade can be localized in a zone of reduced lattice density. In turn, point

defects result in a higher density of extended defects and enlarge the number of point-, line-, planar, and bulk defects. Typical planar defects (like grain-, subgrain-, or twin boundaries) and bulk defects (like clusters of point defects, cracks, voids, bubbles and particles of a different orientation or structure) and their combination decrease the total strain energy of the crystal lattice [Ba80,En97,Gr93,Ha97,Sc96].

Additionally to the point defects, known from metals or other monoatomic materials (vacancies, interstitials, or substituted atoms), for ionic lattices other point defects are possible:

Schottky defects: same number of vacancies of cationic and anionic atoms of the lattice on the condition of quasi-neutrality.

Anti-Schottky defects: same number of vacancies of cationic and anionic atoms at interstitial places on the condition of quasi-neutrality.

Frenkel defects: vacancies at the cationic part of the lattice and same number of cations at interstitial lattice sites on the condition of quasi-neutrality.

Anti-Frenkel defects: vacancies at the anions of the lattice and same concentration of anions at interstitial lattice sites on the condition of quasi-neutrality.

Additionally to defect formation, described above, secondary effects, induced by ion bombardment occur. Herby, a higher mobility of the species in the lattice, radiation enhanced diffusion and the emission of secondary electrons can be set as an example. The later may have important influences to the chemical reactivity of the surface.

Collisions in surface near regions can be responsible for emission of atoms in the outer atomic layers. This kind of re-sputtering process may lead both to a reduction of the growth rate and changes in the chemical composition. An enrichment of the compound with the lower sputtering yield and higher binding energy, respectively, can take place. Furthermore, the emitted atoms can be adsorbed again on the surface as adatoms or act as new nuclei. With an increase of the number of nuclei density on the surface, interactions of these emitted atoms with the growth kinetics is probable. The films own lower porosity, dense and equiaxed grains at the expense of a columnar structure. Moreover, ion bombardment treatment while film growth can also govern the adatom mobility, the defect density of the crystal lattice, and the crystallographic orientation as well as the chemical reactivity and dissociation of gaseous molecules for reactive deposition techniques. This can result in a film densification (similar to heat treatment), or incorporation of energetic gaseous particles. The particular amount of effectiveness for changes of the film properties depends on several parameters like substrate temperature, material properties, ion flux, bias voltage, etc.. Nevertheless, ion bombardment treatment is an effective way to improve and enhance coating behaviour [En97,Ma89,Gr93,Sm90,Ro92b].

4 Coating materials

4.1 Hard coatings

4.1.1 General

In the last decades, the number of known hard coating materials has tremendously increased. At the beginning, transition metal carbides, nitrides, oxides and borides like TiN, CrN, ZrN, TiC, Cr-C, WC, Al_2O_3, ZrO_2, ZrB_2, TiB_2, CrB_2, etc., were state of the art and have achieved the highest level of commercial success. More recent approaches also include metastable structures, with impurities and additives doped coatings, or tenary and quaternary coating systems as well as nanostructured materials [Su86].

Hard coatings can be subdivided by several ways. First, they can be classified according to their chemical bonding (metallic, covalent, and ionic, see Fig.4.1) and second, to their hardness, respectively. Hereby, hard coatings (> 20 GPa), superhard coatings (> 40 GPa) and ultrahard coatings (> 80 GPa) can be distinguished [Ho89b,Ve99].

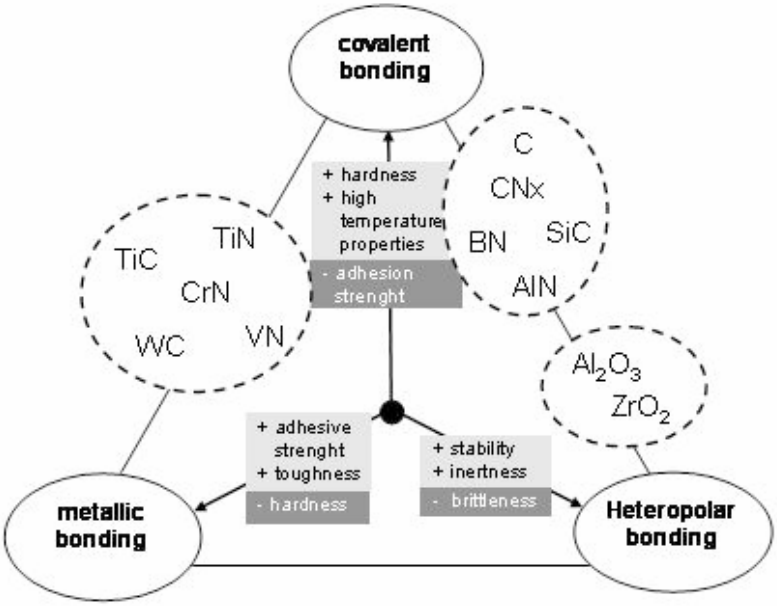

Figure 4.1: Classification of hard coatings corresponding to their bonding character and effects in properties [Ho89b].

Depending on the used deposition technique, a plenty of varieties of different microstructures (grain size and orientation, texture, morphology, etc.) can be obtained. Such an example of a PVD-TiN coating can be seen in Fig. 4.2. The transmission electron microscopy image (TEM) of this film, deposited by magnetron sputtering, shows elongated grains forming a columnar structure [Pe89,Pe03].

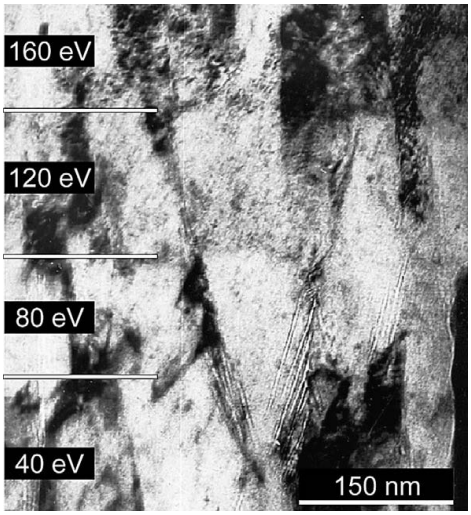

Figure 4.2: Cross section TEM image of a PVD-TiN film deposited with different ion bombardment conditions. Different image contrasts are a result of defects and strained areas [Pe89,Pe03].

Hereby, the ion bombardment was increased in steps of 40 eV. A columnar structure with open columnar boundaries can be observed for ion bombardment < 80 eV. An increased ion bombardment at 120 eV results in film densification and disappearance of voids along columnar boundaries. Thereby, incorporation of residual damage from point defects and dislocation aggregates takes place and is elevated at higher voltages. Further increasing of the ion bombardment up to 160 till 200 eV results in renucleation due to local epitaxial growth on single columns [Pe89,Pe03].

Films, prepared with plasma assisted, low temperature techniques for industrial applications, normally exhibit inhomogeneities and gradients over the film thickness and often are in non-thermodynamic equilibrium. This is used for preparation of artificial structures (nanocolumnar, nanolaminar and nanocomposite structures) and metastable phases. With annealing of deposited coatings recovery and stress relaxation, recrystallization, interdiffusion or phase transformation can be achieved, depending on the nature of the film. All of these phenomena and their influences to the material properties are responsible for the widespread use of hard coating materials beyond the classical tool application [Ma06]. For the majority of PVD films, classical mechanism of hardening, based on the providing of obstacles for dislocation movement, are valid and they can be subdivided into: (1) elevated density of defects (point and line) formed during growth, (2) internal boundaries (grain, phase, and column), (3) second phase particles, and (4) solutes [Ca96,Ma03,Po00]. An additional effect for increased hardness compared to the corresponding bulk material can be found in the formation of metastable phases, e.g. supersaturated solid solutions [Ma02c].

New approaches in surface engineering provide the development and improvement of PVD coatings according for their individual need and application. For example, an addition of carbon to TiN films under formation of a stable Ti(C,N) solid solution improves the tribological behaviour and corrosion resistance. On the other hand, an addition of Al leads

to the formation of (Ti,Al)N coatings with a supersaturated TiN-based solid solution with additional Al [Mü86,Su85]. Another example is the combination of unique properties like e.g. superhardness and high toughness, or self-adapting effects for low friction applications [Ve99,Vo00].

The mechanical properties of thin films depend on their microstructure and their individual bonding nature within the grain-interface system. When plastic deformation takes place, atoms are displaced with respect to each other, and the more they are able to move, the more ductile is the coating. This effect also can be observed for creep processes (dislocation climb, diffusion, and mechanisms like grain boundary sliding). For dislocation climbing, lattice defects and their diffusion have to be necessary, and in contrast to glide processes, this act of motion depends on thermal activity [Sc96].

For classical metallic materials, work hardening (strengthening during plastic deformation) can be observed by an enhancement of the dislocation density, and the hardness increases as the interaction between dislocation increases. This effect can also be seen by increasing the grain boundary fraction (implies reduction of the grain size), which increases the barrier to dislocation motion. Therefore grain refinement in the nanoscale regime decreases the density of dislocations (necessary for plastic deformation), and thus small-grained crystalline films (nanocrystalline coatings) exhibit improved strengthening [Ar98,Ca96,Ma03]. The hardness H (determined by Vickers indentation) is often used as an estimate of the strength of the coating. For ductile films, hardness relates roughly to the yield strength (yield strength ~ 3H), and for hard materials, additionally the elastic modulus E and the Poisson ratio m are taken next to the yield strength to estimate hardness (yield strength ~ E/10). The prediction for hardness certainly exhibits great variance due to the existence of crystal imperfections, microscopic defects, and cracks [Ke86,Ma64,Ro95a,Ta51]. In nanocrystalline systems, two kinds of atoms exist. The first class are atoms which are embedded into the lattice and neighboured by atoms like themself, and the second class are boundary atoms with random orientation and a variety of interatomic spacings. Contrary to single-phase materials, nanocrystalline materials consist of a high value of interfaces and consequently a high number of atoms within them or in their near. This is the reason for degraded density in the interfacial component [Ma06,Su95]. In single phase PVD films, typically a one- or two-dimensional orientation of the nanostructure is predominant, but depending on the deposition parameters (ion bombardment, substrate temperature, simultaneous growth of a second phase, or addition of doping atoms), a three-dimensional orientation can be obtained [Ma06,Mu98].

The Hall-Petch formula describes the relation between the average grain size and the material strength.

$$\sigma_y = \sigma_0 + k_y \frac{1}{\sqrt{d}} \qquad \textbf{(4.1)}$$

where σ_y is the yield stress, σ_0 is a materials constant for the starting stress for dislocation movement ("friction stress") and k_y is the strengthening coefficient, also termed Hall-Petch factor (a constant unique for each material) [Ha51,Pe53]. It can be seen, that strength increases reciprocal to the square of the grain size. The Hall-Petch strengthening is limited by the critical grain size d_c. Beloy d_c, this effect may cease or even reverse (inverse Hall-Petch effect), depending on the individual material parameters. Further reasons can be found in a suppression of dislocation pile-ups, grain boundary sliding, or elevated porosity at small grain sizes (cp. Fig. 4.3) [Ar98,S98,Ki98].

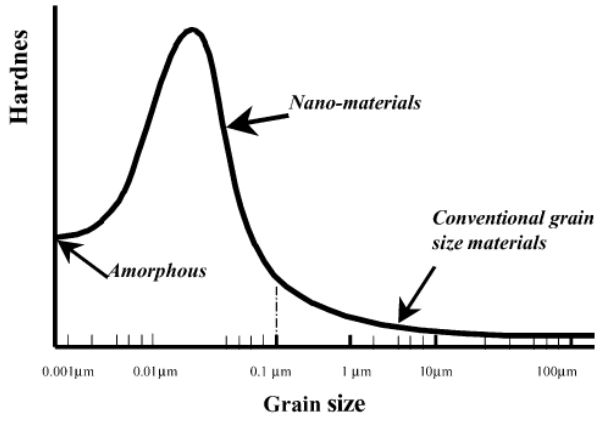

Figure 4.3: Relationshp between hardness and grain size [Sc01].

4.1.2 Single component hard coatings

As mentioned in the chapter before, the microstructure which is determined during film growth, mainly influences the mechanical properties. Some of these interactions will be discussed in the following, using the most studied single-phase model coatings like CrN and TiN.

Densification and/or modification of the morphology of the material can be achieved by appliance of ion bombardment at low temperatures. Stresses in the film are generated via impinging energetic particles during plasma processes. Ions are accelerated by a negative substrate bias potential to the growing film. As a result, increased defects can be observed (cp. chap. 3.4.2) [Ma89].

Typical microstructural defects occuring in single phase thin films, are demonstrated in Fig. 4.4 – Fig. 4.6. This representative TiN film was prepared non-reactively and the investigations were done by employing a high-resolution transmission electron microscope (HR-TEM). Dislocations, as shown in Fig. 4.4a, induce long-range stress fields and diffuse lattice regions. An enlarged view of the dislocation at the bottom of Fig. 4.4a is presented in Fig. 4.4b. Hereby, the strained region is the result of the interjectional lattice plane and results in a lower density in the near of this dislocation [Ma02c,Ma06].

Systematically arranged dislocations are able to build up low-angle grain boundaries, also called subgrain boundaries (Fig. 4.5a).

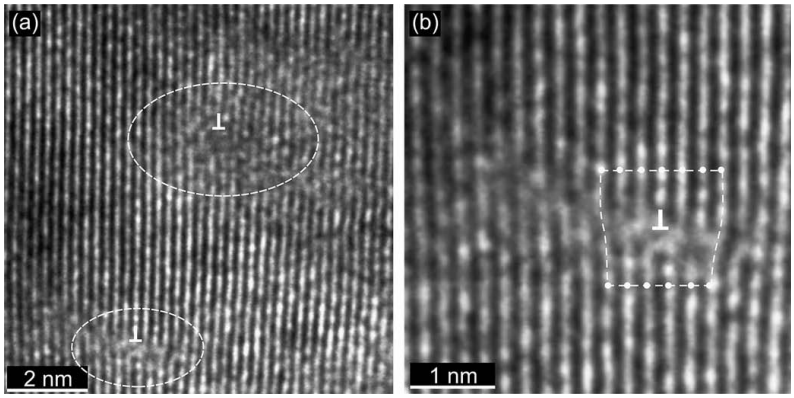

Figure 4.4: HR-TEM image of dislocations within the TiN lattice [Ma04,Ma06].

They are composed of an array of dislocations with a misorientation of less than 15 degrees and interjectional lattice planes. An enlarged view of the subgrain boundary including the participating dislocations is shown in Fig. 4.5b. An exceeding of the misorientation degree higher than 15 degrees causes the formation of high-angle grain boundaries (Fig. 4.6). In certain cases, a coincidence-site lattice can be observed. It is constructed by taking two lattices with a common orgin, and allowing them to pentrate all space. Those lattice points, common to both lattices, are named coincidence points [Ca96,Go01,Ma06,Sc96].

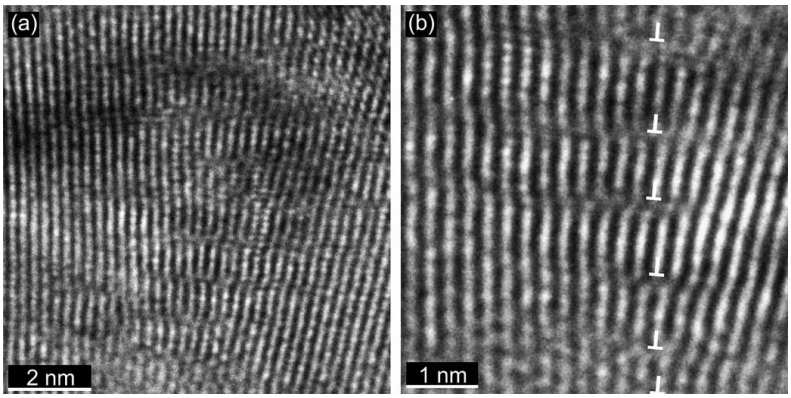

Figure 4.5: HR-TEM image of low-angle grain boundary [Ma03,Ma06].

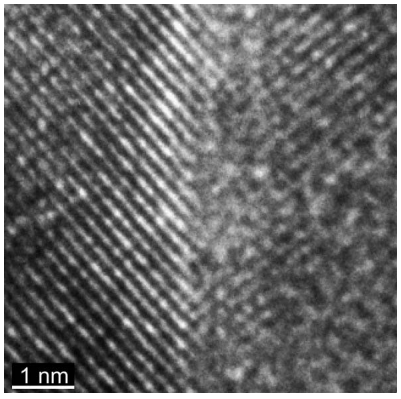

Figure 4.6: HR-TEM image of high-angle grain boundary [Ma03,Ma06].

Microstructural defects like point-, line-, and area- defects also can be investigated with X-ray detection (XRD) or indirectly by stress measurements. Peak position, maximum intensity and full width at half maximum (FWHM) are significant parameters for interpretation of XRD patterns. Broadening of line profiles indicates defects in generally, but especially by three-dimensional defects like subgrains, and finite grain size. Asymmetrical line profiles or orientation dependence of the diffraction peak shapes are indications for lattice faulting/twinning, pronounced dislocation density, and dislocation distributions. A shift of XRD reflections relative to their standard values (equates to a displacement to smaller or larger diffraction angles), based on a change in the unit cell parameters, points towards compressive or tensile intrinsic stresses [Kl98,Ma06,Mi04].

Defects play an important role for the constitution of residual stresses but also act as obstacles for dislocation movement. Consequently, a high defect density causes strain hardening and increases the hardness of coatings, compared to their equivalent bulk material. For several single-phase coating systems, a linear relationship between hardness and residual stresses has been reported (e.g. TiN, Ti(C,N), or CrN) and is shown in Fig. 4.7 for CrN and TiN. The Hall-Petch relationship can be applied to both systems, but for CrN, the critical grain size d_c is reached at around 10 nm. Beneath this grain size, a further refinement yields an increase in hardness, according to the inverse Hall-Petch effect [Ma01a,Ma02c,Ma06,Ka02,Ka98].

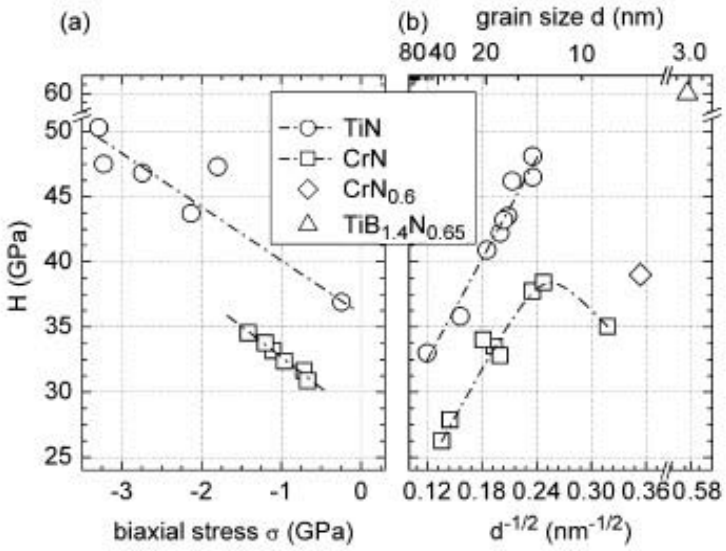

Figure 4.7: Interrelationship between **(a)** hardness and biaxial stresses and **(b)** hardness and grain size for single phase CrN and TiN hard coatings [Ma01a,Ma02c,Ma06].

The mechanisms, responsible for this effect, are not clearly understood yet, but as suggested by Carlton, they can be subdivided into four classes: (1) dislocation based, (2) diffusion based, (3) grain boundary shearing based, and (4) two-phase based [Ca07]. Nevertheless, a conversion from dislocation-dominated plastic deformation to grain boundary sliding appears at a critical grain size when the stress, necessary for dislocation

movement or formation, is higher than for grain boundary sliding. For most of those coating materials, which do not behave according to the Hall-Petch relation, a correlation between macrostress and hardness can be found (cf. CrN in Fig. 4.7a). Summing up, both the grain size and the residual stresses are responsible for the hardness of simple phase coatings [Ma06].

4.1.3 Composite hard coatings

With preventing the motion and multiplication of dislocations, grain boundary sliding, and the growth of microcracks, the hardness of coating materials can be improved dramatically by generation of extremely small grains. Several coating systems are known up to now, which statisfy these requirements like Ti-Si-N and Ti-B-N, and exhibit high hardnesses up to 70 GPa. Their mechanical properties are unique and no critical grain size d_c for a softening effect can be noted. They can be generated by energetic ion bombardment during deposition or by spinodal phase decomposition; both approaches support the formation of stable nanostructures by self-organisation [Ve05].

Materials, which indicate different phases and at least one of them is nanosized in all three dimensions, are called nanocomposites. Some typical types concerning their structure can be classified as composed of (1) amorphous-(a) and nanocrystalline-(nc) phases (nc-TiN/a-Si_3N_4/a-$TiSi_2$, nc-TiC/a-C), (2) nanocrystalline biphases (nc-TiB_2/nc-TiN, see Fig. 4.8), and (3) nanocrystalline phases in combination with metals (ZrN/Ni, ZrN/Cu, CrN/Ni, etc.). As further requirement for biphase nanocomposites, the phase system has to be immiscible (i.e. they must display thermodynamically driven segregation during deposition) and the cohesive energy at the interface between both phases has to be high. At least, the second nanocrystalline (or amorphous) phase must exhibit high structural flexibility to balance the coherency strain without building dangling bonds, voids, or flaws. The hardness of such materials can be improved even for average grain sizes below 6 -10 nm, i.e. coatings with a hardness of 20 GPa can reach superhardness > 40 GPa. [Kn96,Ma05,Ma06,Mi99,Mu00,Mu02,Mu99,Ve05,Ve95,Ve99].

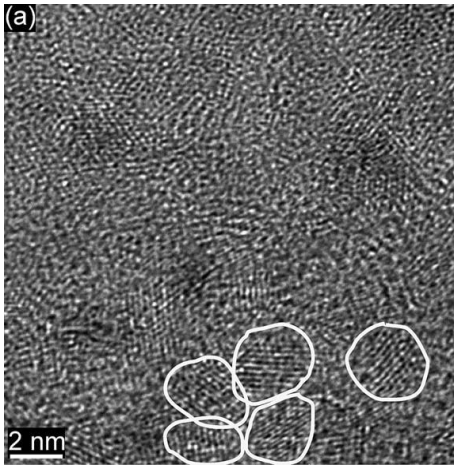

Figure 4.8: HR-TEM image of a nc-TiB_2/nc-TiN film. Some nanograins are marked by white lines [Ma06].

A typical represantive for a nc-/a- system achieving superhardness can be found in stable, refractory transition metal nitrides M_nN (M = Ti, Zr, Hf, V, Nb, Ta, and Cr), because all of them crystallize during deposition at low temperatures below 100°C [Fi87,Ja85,Sa69,Sa94]. Silicon nitride, on the other hand, exhibits the necessary structural flexibility due to its nature of chemical bonding (threefold coordination of N combined with the fourfold coordination of Si) but grows amorphous even at 1100°C. Other transition metal compositions like silicides, borides and carbides possess a high Gibbs free energy of formation and a high composition flexibility.

A more advanced approach for formation of superhard nanocomposite materials consists in the combination of transition metal nitrides with aluminium nitrides or boron nitrides, respectively. Because silicon dissolves in many metals, the choice of boron nitride, aluminium nitride, and other materials as the grain boundary material, offers potential and advantages with respect to many applications (machining, high temperature stability, etc.) [Ve99]. Till now, various different types of nanocomposite coatings have been prepared and are presented in Table 4.1 [Mu00].

Tab. 4.1: Different nanocomposite hard coating systems [Mu00].

composition	representative	Ref.
nc-MeN/a-nitride	nc-MeN/a-Si_3N_4 (Me = Ti, W, V)	[Di98], [Mu86], [Ve98]
nc-MeN/nc-nitride	nc-TiN/nc-BN	[Ve98]
nc-MeC/a-C	nc-TiC/DLC	[Vo98]
nc-MeN/metal	nc-ZrN/Cu	[Mu99]
nc-MeN or MeC/a-boron compounds	nc-Ti(B,O)/quasi-a-(TiB_2, TiB and B_2O_3)	[Mi98c]
nc-WC + nc-WS_2/DLC	nc-WC + nc-WS_2/DLC	[Vo99]
nc-MeC/a-C + a-nitride	nc-Mo_2C/a-C + a-Mo_2N	[Be99]

Nanocomposites can be produced by several ways, employing the range of different CVD and PVD techniques. For the formation of nanostructures, generated during deposition and thermodynamically driven segregation, the activity of nitrogen must be high and the substrate temperature as low as possible, but high enough to support diffusion during film growth. Compared with CVD and its application of halogenated transition metals, PVD has the advantage of being a halogen-free process. On the other hand, it is more complicated to reach the high chemical activity, necessary for phase separation and formation of nanocomposites [Le91,Kn86,Kn92,Ta92].

As an example, for TiBN coatings, a higher substrate temperature and bias voltage enforce phase segregation and result in higher hardness. Additionally, the hardness of such films depends strongly on the chemical composition. A maximum can be obtained for a composition of $TiB_{0.6-1}N_{0.5}$, where a very fine, almost isotropic, nanocrystalline microstructure can be found [Gi94,Ha94]. This corresponds to a BN phase amount of about 20 %. Consequently the maximum hardness depends on the nitrogen partial

pressure, the substrate temperature, and the negative bias voltage applied. As example for TiBN films, the highest hardness (~ 50 GPa) was achieved with a substrate temperature of 300 - 400°C, an ion energy of 126 eV and a N_2 partial pressure below 15 %. An increase of the N_2 partial pressure resulted in a decrease in hardness (~ 20 GPa) due to the formation of h-BN and a composition of TiB_2N_2 [Gi97,Lo97b,Mi98c]. On the other hand, increasing the substrate temperature, plasma density and negative bias voltage resulted in formation of superhard nc-TiN/BN nanocomposites at an expense of formation of h-BN [Ho00b].

Nanostructured superhard nanocomposites are able to sustain much larger strain than conventional hard coatings and this is due to several reasons. In nanostructured materials with average grain sizes of 3 – 5 nm of equiaxed nanocrystals, the extension of the stress-induced flaws is at the scale »1 nm, i.e. at a scale comparable with interatomic bond distance. The high elastic strength can be explained by the “reversible non-linear flexing” mechanism and is schematically demonstrated in Fig. 4.9.

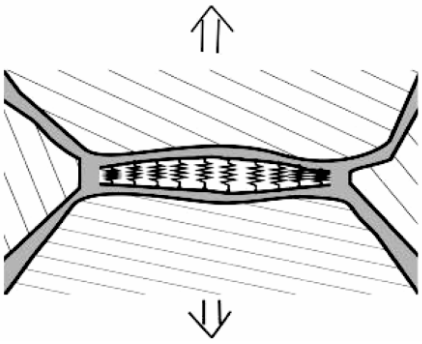

Figure 4.9: Flexing of the bonds across the interface between nanocrystals [Ve01].

If the elastic strain energy associated with the elastic deformation of the attached nanocrystals remains less than the energy of flexing of the bonds across the interface, the system will continue to be stable and reversible and the energy of flexing of the entire system will fully recover upon unloading. Compared with the linear elastic deformation of conventional materials, the energy density of flexing per unit of the flexed volume is not very high for nanocomposites, due to their high fraction of interface volume. This effect explains the high elastic energy and the property of high elastic recovery.

The high resistance of nanocomposites against crack formation can also be explained in terms of crack generation (but scaled down to a dimension of 1 – 2 nm). Due to the high interface fraction, the stress, required for nanocrack-formation, has to be very high. Furthermore, the spread of those nanocracks in the three dimensional nanocomposite involves much deflection and branching of the plane of the cracks. These cracks again hinder the growth of the nanocracks. Therefore, the self-organization of the system, based on thermodynamically driven segregation, results in a very low concentration of built-in flaws. Thus, the unique high resistance of these nanocomposites against crack formation

can easily be understood in terms of a high threshold for the initiation of larger microcracks, which would lead to their growth [Ve00a,Ve01].

Nanocomposite hard coatings often exhibit a high thermal stability, sometimes in combination with a “self-hardening” effect. Both, the crystallite size and the hardness are stable up to 1000°C for nc-TiN/a-BN coatings and up to 1100°C for nc-TiN/a-Si_3N_4. The lower stability of nc-TiN/a-BN is based on partial oxidation of BN and loss of boron by sublimation of BO_x. The highest thermal stability for TiN/a-BN composites can be obtained at the optimum composition, when the coverage of TiN crystallites with BN is around one monolayer [Ka03,Ka04]. A temporary self hardening effect was observed for $(Ti_{1-x}Al_x)N$ coatings at temperatures of about 800 – 900°C, based on formation of an intermediate metastable cubic c-AlN phase and c-TiN. These phases are built by spinodal decomposition of a supersaturated $(Ti_{1-x}Al_x)N$ solid solution. A further increase in annealing temperature < 900°C results in formation of h-AlN and coating softening [Ma05,Ve05].

4.2 Solid lubricant coatings

4.2.1 General

Solid lubricating coatings are mainly applied to control friction and wear under critical conditions, where conventional liquid lubricants and/or greases cannot be used for (high temperatures, high loads, high speeds, and vacuum). Up to now, no single phase coating can fulfil low friction and wear resistance over a broad range of applications; furthermore the lifetime of solid lubricant coatings is limited. Solid lubricants are defined as materials with low shear strength and when applied on a sliding surface, they are able to reduce friction and wear. According to their mechanical properties (hardness more or less than 10 GPa), they can be subdivided into (a) soft and (b) hard lubricants (see Fig. 4.10). Hard solid lubricant coatings include some carbon-, oxygen-, and nitrogen-based coatings, whereas inorganic soft solid lubricant coatings primarily are based on soft metals, laminar structured solids, and transition-metal dichalcogenides [Bh01,Do04,Do95,Ho94].

Soft metallic lubricants own a crystal structure with multiple slip planes and do not work-harden during sliding contact. Point defects and dislocations formed by sliding deformation are quickly merged due to friction heat production.

Inorganic laminar structured materials like graphite, hexagonal boron nitride (h-BN), or MoS_2 owe their lubricity to their layered structure. Atoms, lying on the same layers, are closely packed and strongly bonded to each other, whereas the layers themselves are relatively far apart. Therefore, the bonds between these layers align themselves parallel to the direction of sliding motion, which provides low friction. Friction coefficients of laminar lubricants are between 0.002 and 0.7, those of soft metals between 0.15 and 0.35, for oxide based coatings friction coefficients between 0.05 and 1 were observed, depending on contact conditions.

Hard coatings Hardness higher than ≈ 10 GPa	Soft coatings Hardness lower than ≈ 10 GPa
Nitrides TiN, CrN, ZrN, BN, $BaSO_4$	**Soft metals** Ag, Pb, Au, In, Sn, Cr, Ni, Cu
Carbides TiC, WC, CrC	**Lamellar solids** MoS_2, WS_2, Graphite H_3BO_3, HBN, GaS, GaSe
Oxides Al_2O_3, Cr_2O_3, TiO_2, ZnO, CdO, Cs_2O, PbO, Re_2O_7	**Halides sulfates, sulfur** CaF_2, BaF_2, PbS, $CaSO_4$, $BaSO_4$
Borides TiB_2	**Polymers** PTFE, PE, Polyimide Polymerlike DLC
DLC & Diamond a-C, ta-C, a-C:H, ta-C:H, CN_x a-C:X(:H), (nc-)diamond	

DLC = diamondlike carbon
a= amorphous
ta = tetrahedral amorphous
X = a metal
nc = nanocrystalline
PTFE = polytetrafluorethylene
PE = polyethylene

Figure 4.10: Classification of tribological coatings, depending on the nature of constituting materials [Do04].

Lubricity of these laminar solids in ambient air at elevated temperatures is controlled by their tendency to resist oxidation. Furthermore, the presence of humidity, water vapour or oxygen decrease or annihilate the ability to lubricate due to the destruction of the laminar structure. For this work, inorganic laminar structured materials were used, thus they are described in more detailed in the following chapters (see chap. 4.2.3 and 4.2.4) [Bu99,Er00a].

For thin film technology, the evolution of single and multicomponent solid lubricating films is graphically summarized in Fig. 4.11. The “first” generation of solid lubricating coatings was evolved by refinement of the microstructure and chemical composition of single compound self lubricating coatings like MoS_2 [Do04,Sp69,Sp71,Sp80,St81]. Coatings of the “second” generation with multifunctional faculties like hybrid, duplex or multiplex film architecture were firstly synthesized in the middle of the nineties [Be97,Bi96,Ma02a,Ma97,Ye99]. Investigations exhibited that the use of an intermediate layer enables to increase corrosion resistance and toughness, while the top layer can provide low friction. Generally the second generation is fabricated by combining a solid lubricant with another soft or hard layer, like TiN and MoS_2 in a dual, multicoating architecture or as multicomponent composition. Nanostructured coatings including nanocrystalline films with grain sizes of a few nanometer and nanocomposite films can be

imputed to the “third” generation. Nanocomposites include structures that join amorphous with crystallized phases [Be97,Gi98,Ho94,Ma97,Ve99,Za00].

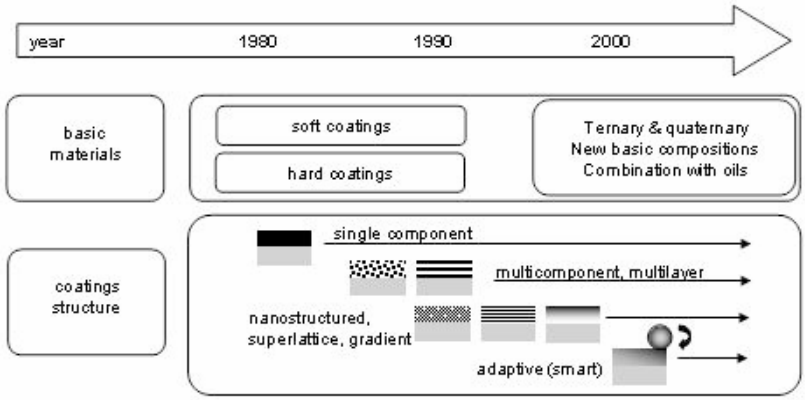

Figure 4.11: Historical development of tribological coatings and solid lubricant films [Do04].

For example, investigations of randomly oriented Mo–W–S–Se films after tribological contact exhibit a self-arrangement of laminar structures parallel to the sliding direction. Hereby, a surface material modification occurs by atomic rearrangements in the sliding interface, which results in the recrystallization and reorientation of a film with a thickness of a few atomic layers (5-10 nm). This results in friction coefficients of about 0.02 [Hu08].

Another improvement in solid lubricant coatings embraces the fabrication of nanolayered superlattice coatings, which is a continuation of the multilayer concept mentioned above. Coatings of the fourth generation have the capability to adapt to operating conditions and to change their properties, respectively. As examples the most lately developed cutting-tool coating (based on Ti-Al-N alloyed with yttrium or chromium) form a stable oxide during cutting at high temperature, which increases their wear resistance. The second example is a composite coating synthesized within the system W-C-S, which consists of 1–2 nm WC and 5–10 nm WS_2 grains embedded in an amorphous DLC matrix. These WC/DLC/WS_2 nanocomposites show self-adaptation phenomena promising for aerospace systems [Sa99,Vo00,Vo95,Vo99].

4.2.2 Diamond-like carbon based coatings

Diamond-like carbon (DLC) films are synthetic and metastable materials used for mechanical, tribological, optical, and electronic applications. The term describes carbon based coatings without a dominant crystal structure (in opposition to diamond or graphite) and with various amounts of hydrogenated as well as non-hydrogenated carbon. The H content rules coating structure, which is amorphous and consists of a mixture of sp^3 (diamond) (Fig. 4.12b) and sp^2 (graphite) (Fig.4.12c) bonded carbon. In Fig. 4.12a, the ternary phase diagram of hydrogenated carbon based materials is illustrated. Several types and compositions are known, but the most popular structure of DLC is called a-C:H. In that case, an amorphous hydrogenated a-C:H film with a high H content (up to ~ 50

at.%) and only moderate sp^3 content can be observed. For DLC coatings without H, two types with different binding structures are known and investigated: (1) tetragonal amorphous C with a high amount of sp^3 hybridization of up to 85 % (also called ta-C) and (2) amorphous C showing a predominance of sp^2 hybridization [Er01,Gr99].

Lots of vapour deposition techniques for production of DLC coatings are established, whereby arc evaporation, laser ablation, and magnetron sputtering are common for non-hydrogenated types. On the other hand, for hydrogenated types, plasma-assisted CVD techniques are more suitable and applied [Er01].

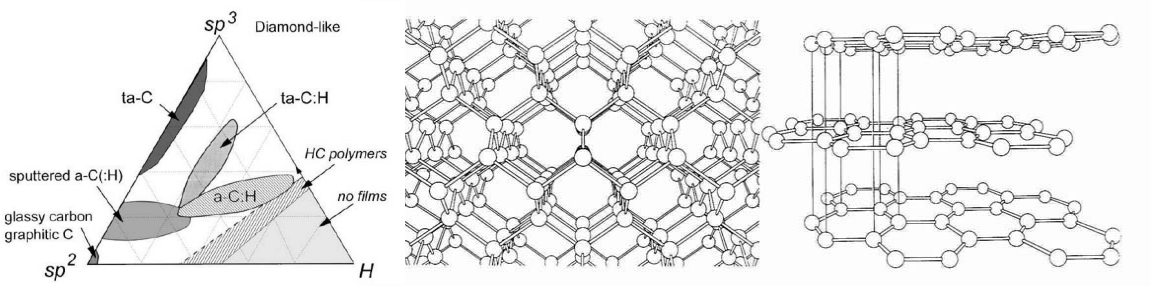

Figure 4.12: (a) Ternary phase diagram of hydrogenated carbon based materials [Ja93], **(b)** 3-d structure of sp^3 hybridisated diamond, and **(c)** and sp^2 hybridisated graphite [Ho94].

Graphitization of DLC starts at around 250°C and a rapid loss of hydrogen with a simultaneous formation of sp^2-configuration can be obtained at around 400°C, depending on the DLC type. This process plays a crucial role for tribological applications at elevated temperatures and/or high loads [Do98,Ta95].

Depending on the conditions of tribotesting and the properties of DLC coatings, friction coefficients (cof.) are typically between 0.01 and 0.5. An interfacial transfer layer, generated during sliding contact, is responsible for this friction behaviour. Hereby, a layer of shear strength with sp^2 hybridization is formed on the surface region of the DLC film. Generally, hydrogenated a-C:H coatings exhibit higher cof. than hydrogen-free (ta-C) films. For ta-C coatings, a shear-induced graphitization ($sp^3 \rightarrow sp^2$) in the contact zone and the origin of a graphitized tribolayer is identified as mechanism, resulting in a decreased friction coefficient. The mechanism of layer-formation and its frictional behaviour is strongly influenced by humidity (cof. between 0.05 and 0.30 at 20 % – 60 % relative humidity in ambient air). This effect is based on the formation of a condensed water layer in the contact zone including cooling. Therefore, the temperatures, necessary for graphitization, can not be reached and the mechanism of sp^2-tribolayer formation is inhibited, respectively. Moreover, oxidation processes may take place and affect the generation of C-O bonds. Nevertheless, no graphitization with reduced friction coefficients were observed at very high humidity [Do98,Gr99,Ho94,Ki9,Li96].

The tribological behaviour of DLC coatings in inert gas atmospheres like nitrogen or vacuum show ambivalent characters with friction coefficients of less than 0.01 and above

0.5, respectively. It is more likely that different hydrogen contents, which highly influence the friction behaviour, also influence the adhesion of the coating to other counterpart materials. This results in different tribological mechanisms. The friction behaviour for DLC coatings can be recapitulated as followed:

(1) The friction behaviour of DLC coatings equates to that of diamond in vacuum, but not in the presence of humidity. (2) The friction coefficient increases from very low (~ 0.01) with increasing humidity in air, nitrogen and oxygen up to very high (~ 0.5). (3) Annealing and dehydrogenation in vacuum leads to increased friction coefficients in vacuum. (4) During sliding, the formation of a transfer layer is presumable [Gr99].

An addition of metal atoms (10 – 40 %) like chromium, silicon, titanium, or tungsten to the DLC composition improves humidity resistance. This is based on the formation of nanocrystalline metal carbides in the DLC matrix [Be93,Ga05,Ga97,Li96,Mi98b,Ze00].

4.2.3 Hexagonal boron nitride coatings

Hexagonal boron nitride (h-BN) is a promising candidate in thin film technology due to its unique and widespread applications. It has applications for optical devices from the ultraviolet to infrared spectra region and for exciton-based quantum information processing due to its wide bandgap energy of 5.97 eV and large excitation binding energy of 149 meV. Hexagonal BN is an electrical insulator and thermal conductor, but also exhibits piezoelectric potentials, which promises application of h-BN films in the field of surface acoustic wave technology [Bo99,Ho84,Ko07,Lo99,Su98,Ta89,Yo99].

Hexagonal BN is an excellent lubricant (as solid or powder) for reducing wear and friction, due to its graphitic structure. Even at elevated temperatures, it can be used in metal machining based on its high inertness against oxygen. It also can be added to other materials to produce vibrational damping [Oo06].

Preparation of thin films of h-BN can be done by the whole range of coating techniques. Coatings can be deposited by thermally activated condensation and thermal decomposition, employing an ion gun, of borazine ($B_3N_3H_6$) [Au99,Na96], or by CVD (also plasma enhanced CVD) of halogenated boranes or B_2H_6 in an N_2/Ar atmosphere, or in combination with ammonia [Ch99,Wi99,Zh02]. Evaporation with several heating sources like ion beam assisted deposition (IBAD), pulsed laser deposition (PLD), hollow cathode arc evaporation, or plasma activated reactive evaporation of solid B in a reactive atmosphere or non-reactively, using a h-BN vapour source, are reported for h-BN film production [Fu97,Mc96,Re99,Ul03,Wi98]. Reactive sputter deposition of B or non-reactively of h-BN targets is also a suitable way to generate h-BN films [Gi96,Wi99,Zh02].

In analogy to carbon, stoichiometric boron nitride has a polymorph nature and thus is able to form four different structures: (1) cubic (c-BN), (2) hexagonal (h-BN), (3) wurtzite (w-BN), and (4) rhombohedral (r-BN), wherby the first two modifications are the most stable forms of BN under standard conditions (see Fig. 4.13). The crystal structure (e.g. lattice

parameters) of h-BN and r-BN can be compared to that of graphite, whereas c-BN and w-BN (the wurzite structure is a member of the hexagonal crystal system) are built up of tetrahedrally coordinated boron and nitrogen atoms [Mi97]. Additionally to the four structures mentioned above, two artificial modifications can be produced by high pressure and high temperature transformation (HP-HT-synthesis): turbostratic BN (t-BN) and amorphous BN (a-BN), which are disordered. According to the particular bond type (diamond-like sp^3 bonded or graphite-like sp^2 bonded planes), BN is able to form a hard or soft phase [Hu00,Le00].

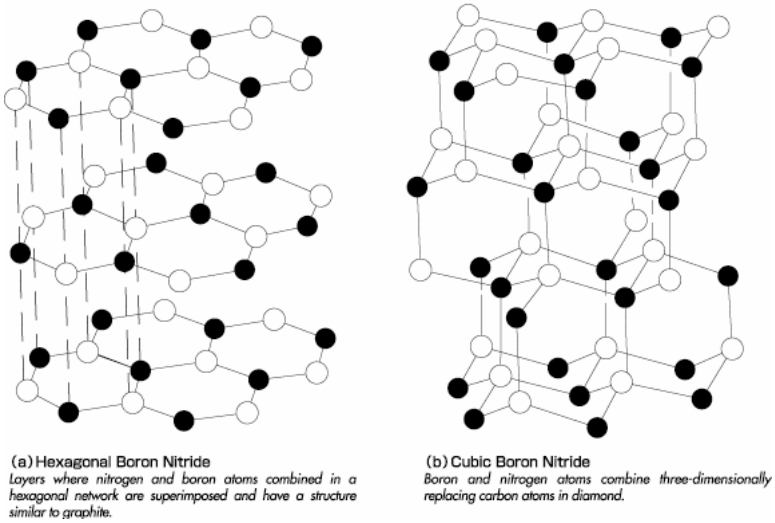

Figure 4.13: Structures of the equilibrium phases of sp^2 bonded h-BN and sp^3 bonded c-BN [Me00].

Despite of the excellent tribological properties and the thermal stability of h-BN, even in ambient air atmosphere, investigations were mainly conducted for electronic applications, including growth mechanism, bonding and structure morphology, and their influences on their optical and electrical properties. Up to now, there are no studies or indications for low-friction properties of h-BN films, or compositions consisting of h-BN, respectively, deposited by plasma assisted vapour deposition [Mo96].

4.2.4 Transition-metal dichalcogenides coatings

Layered transition metal dichalcogenides coatings like MX_2, where M is molybdenum or tungsten and X is sulphur, selenium, or tellurium have been investigated extensively in the last decades. For example, MoS_2 and WS_2 are used or own high potential as absorber material for thin film solar cells, catalysts, solid lubricants, semiconductors (bandgap of 1–2 eV), or as matrix material in intercalation batteries [Al00,Ma02,Re96]. Several crystal structures are known for MoS_2 and WS_2, respectively, like rhombohedra (or trigonal), monocline, and hexagonal, whereas the later one is the most common [Sc81]. Their hexagonal structure is characterized by individual sheets of sulphur and transition metal atoms (see Fig. 4.14). The interactions between the (S-M-S)-(S-M-S) layer units are weak

van der Waals interactions and due to these weak bonds, sliding takes place easily between sulphur layers [Do96,Hi96]. The following discussion mainly focuses on MoS_2, however, particularly WS_2 shows a similar tribological behaviour [Co98,Ra05,Si92,Wa04].

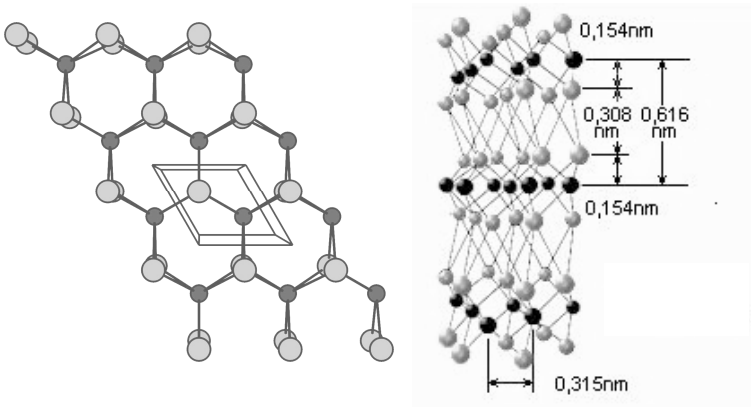

Figure 4.14: Laminar structures of MoS_2 solids with view **(a)** on the planes and **(b)** perpendicular to the planes [Scie].

Composition, microstructure and morphology of sputtered MoS_2 coatings depend on deposition parameters and the presence of oxygen or humidity. Substoichiometric compositions can be obtained ($x \leq 2$, where x is the value in MoS_x) by long substrate-target distances or intense ion bombardment, using a MoS_2 target. For the later, a probable interpretation is that some of the Mo from the MoS_2 is being implanted into the crystal and forming isolated islands of molybdenum as “Mo(0)” [Li89]. The distance between the S-Mo-S layers can vary with a range of few tenth of one nm; this may have two reasons. First, the S-Mo-S layers become thicker as a result of the dispositioning of coordinated atoms surrounding the molybdenum atom due to dislocation relaxation, deformation, and oxygen substitution for sulphur, resulting in local electrostatic imbalances. The second cause is, accordingly, that the S-S distances between double layers become longer. This can be associated with sulphur atoms substituted by more electronegative oxygen atoms in the film. Additionally, an increased oxygen content in the films decreases the order (i.e. increases the defect density) in the film crystallites. This increased disorder results in crystallite size reduction, which in turn results in denser films. Increasing values of x in the $MoS_{2-x}O_x$ phase correlates with increasing friction. Increased x values also result in increased film densification which correlates with increasing film wear resistance. Moreover, the H_2O residual pressure during deposition seems to be an important parameter affecting morphology. Lower partial pressures result in crystalline structures and increasing the H_2O level yields amorphous coatings [Co92,Hi96,Li89,Li95,We97].

In vacuum, dry or inert conditions, the friction coefficient of MoS_2 coatings is very low (0.002 - 0.05) but increases up to 0.2 in humid air. The formation of a transfer film of MoS_2

on the counterbody (adhesive wear) is one reason, leading to this ultra low friction behaviour. The second cause is the formation of a friction-induced orientation of the (0001) basal planes of grains in the contact region, parallel to the sliding direction. On the contrary, the presence of humidity and oxygen degrades the friction coefficient of MoS_2 coatings. This is based on the formation of oxides in the contact zone and water condensation, respectively [Do93,Do96].

An improvement in friction and wear for MoS_2 films can be obtained by addition of titanium atoms (up to ~ 20 at.%), also termed MoS_2(Ti). Hereby, titanium atoms are in solid solution but also form nanocrystallites in the MoS_2 matrix. Moreover, this matrix is assumed to consist of bundles of curved basal planes. This titanium induced distortion results in hardness enhancement (from ~ 4 GPa up to 10 – 20 GPa) and increased wear resistance. An additional benefit can be found in reduced sensitivity to water vapour, this allows applications up to 50 % humidity [Ca03,Er01,Ji04,Re00,Re01,Te01].

The thermal range of lubricity depends on the structure of the MoS_2 films. Turbostratic coatings with open-ended basal planes start oxidising at lower temperatures than high-ordered structures (for the later, temperatures of around 400 – 500 °C are reported) [Er01,Hi96].

Applications of MoS_2 coatings can be found in cutting processes and metal-forming, where top layers are deposited on hard underlayers (TiN, CrN, Ti(C,N)) or as nanocomposites, forming a nanodispersion in a hard solid. They have also been suggested for aerospace applications, e.g on bearings [Gi98,Re01,Vo99].

5 Experimental details

5.1 Coating deposition

All coatings, discussed in this work, were deposited in a laboratory-scale unbalanced magnetron sputtering system (a modified Leybold-Univex 300), which is exhibited in Fig. 5.1. A very detailed explanation and description of the equipment involved can be found in references [Lo98,Ma01,Mi94].

Figure. 5.1: Picture of the PVD system used for coating deposition.

The depositon procedure for all coatings was kept similar and included the following steps:

- Sample mounting: The substrates were mounted on the substrate holder parallel to the target surface at a distance of 10 cm above the target and the chamber was sealed air-tight via a hand crank.
- Chamber evacuation: The chamber was evacuated till reaching a pressure of 0.1 Pa, heated via the substrate heater up to 350°C and the temperature was hold for 30 min. After this treatment, further steps were started when the pressure reached 1-2 mPa.
- Target precleaning: To remove surface contaminations like oxides or nitrides from other depositions, the target was cleaned via sputtering for 10 min with a current of

1.5 A and a gas flow of 15 sccm Ar, wherby the substrates were protected by a shutter, positioned between the target and the substrates.

- Substrate etching: To clean the substrate surfaces, an argon plasma was ignited between the substrates and the shutter. The etching voltage was set to -1250 V and the etching current to ~ 30 – 40 mA at ~ 30 Pa (equivalent to ~ 170 sccm Ar flow). After 30 min of etching the corresponding depostion temperature was reached; the target discharge was ignited and the shutter opened.
- Coating deposition: After adjusting the chosen deposition parameters (bias voltage and gas composition), the coatings were deposited with a constant total gas pressure (p_{Ar} or $p_{Ar} + p_{N2}$) of 0.4 Pa, controlled by a calibrated thermocouple as well as a capacitive gauge. The sputter power density on the target was set to ~ 4 W/cm^2.
- After deposition, the chamber was cooled down to temperatures below 80°C to avoid thermal oxidations and finally vented.

All coatings, discussed in this work, were deposited with the targets materials listed in Tab. 5.1. The films within the systems Cr-MoS_2-N and Cr-WS_2-N were deposited using a Cr-target with circular holes (diameters of 8 mm and depths of 4 mm) in the sputter track. According to the chosen target composition, these holes were filled with inlays of MoS_2 and WS_2, respectively, or Cr inlays. A picture of this mosaic Cr-target is shown in Fig. 5.2.

Tab. 5.1: Employed target materials and their dimension.

target material	supplier	purity (%)	dimension (mm)
Cr	Mateck	99.95	152.4x6
CrB2	Chemco	99.5	150x6
Cr80/B20	Plansee		152.4x6
MoS2	Mateck	99.9	150x4
WS2	Chemco	99.8	150x4
Cr-rod	GFE	99.9	8 ø

Figure 5.2: Cr-target used for deposition of coatings within the system Cr-MoS_2-N and Cr-WS_2-N.

As substrate materials mirror-polished silicon (100) (20x7x0.45 mm) and AISI M2 high-speed steel (HSS) disks (DIN 1.3343, ø=30×10 mm) with a hardness of 65 HRC were used. Films on silicon substrates were used for fracture cross-section images, electron probe micro analysis (EPMA), X-ray photo electron spectroscopy (XPS), X-ray diffraction (XRD), and biaxial stress temperature measurement (BSTM). The hardness as well as the tribological behaviour of the coatings were investigated employing coated HSS substrates. The coatings investigated within this work were deposited with the parameters listed in Tab. 5.2.

Tab. 5.2: Table of the chosen parameters for the films, discussed in this work. B is the bias voltage, I is the deposition current, P is the deposition power, T_D is the deposition temperature, p_{N2} is the N_2 partial pressure, DT is the deposition time, and GR is the growth rate.

target	B (-V)	I (A)	P (W)	T_D (°C)	Ar (sccm)	N_2 (sccm)	p_{N2} (%)	Ø (µm)	DT (min)	GR (nm/min)
CrB_2	50	0.171	8.55	**450**	15	0	**0**	4.3	70	61
CrB_2	50	0.147	7.35	**450**	15	0.6	**9**	4.2	60	70
CrB_2	50	0.093	4.65	**450**	14	1	**11**	4.9	60	82
CrB_2	50	0.103	5.15	**450**	13	2	**17**	4.5	60	75
CrB_2	53	0.095	5.035	**436**	12	3	**22**	4.6	60	77
CrB_2	52	0.1	5.2	**450**	11	4	**28**	4.7	60	78
CrB_2	52	0.108	5.616	**450**	11	5	**32**	4.5	60	74
CrB_2	57	0.102	5.814	**450**	9	7	**43**	3.0	60	50
CrB_2	60	0.109	6.54	**428**	7	10	**56**	2.2	60	37
CrB_2	63	0.107	6.741	**435**	5	10	**64**	1.6	60	27
Cr + 20 % B	55	0.207	11.385	**450**	15	0	**0**	2.5	60	41
Cr + 20 % B	57	0.202	11.514	**450**	15	0.6	**9**	2.6	60	44
Cr + 20 % B	52	0.176	9.152	**450**	14	1	**11**	2.7	60	45
Cr + 20 % B	55	0.198	10.89	**450**	13	2	**17**	2.7	60	45
Cr + 20 % B	58	0.21	12.18	**450**	12	3	**22**	2.8	60	46
Cr + 20 % B	70	0.256	17.92	**450**	11	4	**28**	1.9	60	31
Cr + 20 % B	58	0.206	11.948	**450**	11	5	**32**	2.1	60	34
Cr + 20 % B	60	0.18	10.8	**450**	9	7	**43**	1.1	60	19
Cr + 20 % B	62	0.158	9.796	**450**	7	10	**56**	0.8	60	13
Cr + 20 % B	64	0.094	6.016	**450**	5	10	**64**	1.0	60	16
Cr/MoS_2 25 %	50	0.142	7.1	**300**	14	1	**11**	4.5	60	75
Cr/MoS_2 25 %	50	0.125	6.25	**300**	12	3	**22**	3.5	60	58
Cr/MoS_2 25 %	50	0.122	6.1	**300**	11	4	**28**	1.2	60	20
Cr/WS_2 25 %	50	0.167	8.35	**300**	15	0	**0**	7.4	60	123
Cr/WS_2 25 %	50	0.193	9.65	**300**	14	1	**11**	7.4	60	123
Cr/WS_2 25 %	50	0.174	8.7	**300**	11	4	**28**	6.5	60	109
Cr/WS_2 37.5 %	50	0.218	10.9	**300**	15	0	**0**	7.1	60	118
Cr/WS_2 37.5 %	50	0.222	11.1	**300**	14	1	**11**	6.4	60	106
Cr/WS_2 37.5 %	50	0.211	10.55	**300**	11	4	**28**	10.3	60	171

5.2 Scanning electron microscopy (SEM)

An electron beam, generated by an electron gun, gets accelerated towards the anodes, afterwards bunched by a condenser lens and finally focussed as a small spot onto the surface of a sample by an objective lens (see Fig. 5.3). Deflecting coils within the objective lens and in the near of the electron gun are supplied by varying voltages and generate a magnetic field influencing the electron beam and effecting a periodic movement in a controlled two dimensional direction, also termed raster scan pattern [Al97,Fl95].

The electron beam impacts onto the sample surface and generates secondary electrons. This happens by an interaction of electrons, emitted by the electron gun, with weakly bonded electrons from the conduction band of the sample atoms in a specific volume segment. The emitted secondary electrons are entrapped by a detector (consisting of a scintillator, a Faraday cage, a photomultiplier, and a preamplifier), converted into an electrical potential and finally amplified. The electrical potential is displayed on a screen and changes the brightness of the monitor picture element (= pixel).

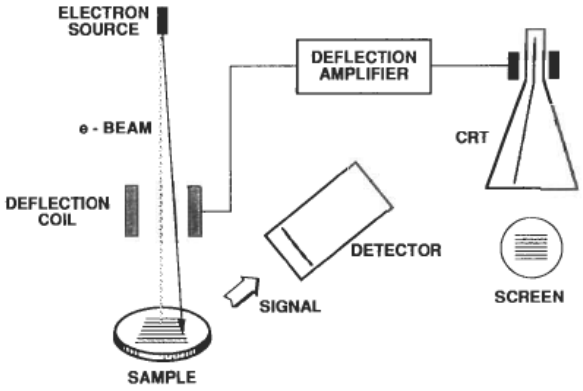

Figure 5.3: Schematic representation of the configuration of a SEM [Br92].

If primary electrons strike at a definite time e.g. on an elevation of the sample surface, a higher number of secondary electrons becomes generated and emitted, which results in a higher electrical potential and increases the brightness of the monitor picture element. On the other hand, a smaller number of secondary electrons are emitted from a recess in the sample surface and consequently less brightness can be observed for this region (also called edge effect). The displayed general view consists of thousands of picture elements and mirrors the surface topography of the investigated sample [Al97,Fl95].

The obtained resolution depends on the area from which secondary electrons are generated and normally, this area is bordered by the spot area. Increasing the accelerating voltage effects backscattered electrons, which are emitted from a larger area of the sample and interact with the surface-near sample material. They generate secondary electrons even further away from the original spot size and reduce the resolution of the image. Several other factors influencing the image resolution are the

density of the sample, the electrical conductivity, the working distance, or the angle of impinging electrons [Al97,Fl95].

Within this work, all fracture cross-section images of deposited coatings on Si-substrates were investigated employing a Zeiss EVO 50 with working distances between 5 and 10 mm and a constant acceleration voltage of 25 kV.

5.3 Electron probe micro analysis (EPMA)

Electron probe micro analysis (EPMA) is a spatially resolved, quantitative elemental analysis technique. Hereby, characteristic X-rays are generated by a focused beam of energetic electrons. With EPMA, concentrations in the range of parts per million (ppm) can be detected; furthermore, an element mapping based on the use of the electron beam can be done which is a useful tool for surface investigations [Br92].

Interactions of energetic electrons with solid matter can be subdivided into elastic and inelastic scattering. Elastic scattering causes significant angular deviation of the electron trajectories, whereby inelastic scattering reduces the energy of the electrons. Mechanisms of inelastic scattering involve the formation of secondary electrons, inner shell ionization, bremsstrahlung (X-rays), long-wavelength electromagnetic radiation in the infrared, visible and UV range, electron-hole pairs, phonons (lattice vibrations), and plasmons (electron oscillations). An electron vacancy is formed by impacting energetic electrons, this leads to inner shell ionizations and this vacancy is filled up by a transition involving one or more outer shell electrons (see Fig. 5.4) [Br92].

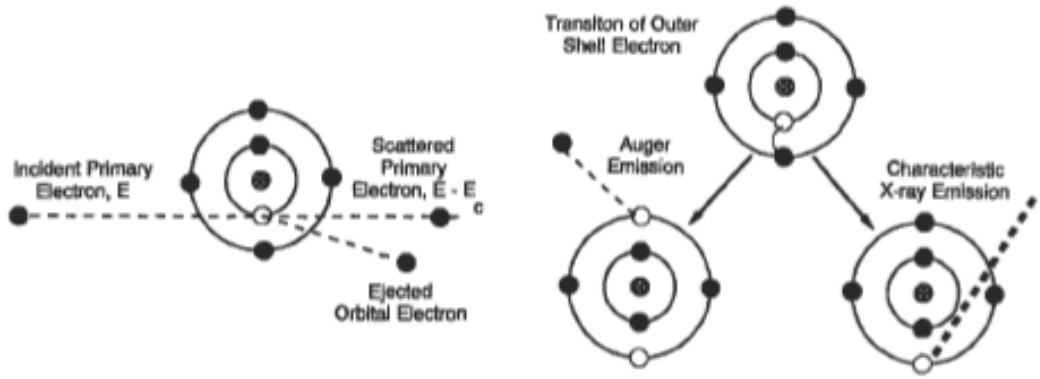

Figure 5.4: Schematic of inner shell ionization and the formation of Auger emission and X-ray emission on the other hand [Br92].

As a result, X-rays or Auger electrons with a well defined energy become emitted and can be attributed to the respective element species. Depending on the atomic number, different families of X-ray energies ($K_{\alpha,\beta}$, $L_{\alpha,\beta,\gamma}$, etc.) occur and can be separated by different filter systems.

The limiting factor for the spatial resolution of EPMA can be determined in the spread of the electrons through the specimen and not in the diameter of the incident probe. A focused electron beam carrying sufficient electron current for EPMA can be obtained with

a diameter that is ~ 5 - 10 times smaller than the dimension of the interaction volume [Br92].

The emitted X-rays can be detected by two methods: energy-dispersive spectrometry (EDS) and wavelength dispersive spectrometry (WDS), whereby both systems are based on different physical effects for measurement of the X-ray energy and intensity. In EDS, the element distribution can be calculated by the phenomena of photoelectric absorption in a semiconductor crystal. The energy of the X-rays becomes proportionally transformed into charge through inelastic scattering of the photoelectron and is detected by an electronic circuit which is connected with a multichannel analyzer [Br92].

With the WDS, the X-ray radiation is split by diffraction by natural or synthetic crystals into their spectral components. The spectrometer is always put on a wavelength and the characteristic X-ray radiation of an element is analysed. The diffraction phenomena is based on the Bragg formula (Equ. 5.1), where λ is the wavelength equivalent of the X-ray energy E (λ(nm) = 1.2398/E(keV)), d is the crystal spacing for the diffracting planes, and θ_B is the angle at which constructive interference occurs (i.e., the Bragg angle). For a complete spectrum the different wavelength areas must be scanned successively, and afterwards, the chemical composition can be calculated.

$$n\lambda = 2d \sin\theta_B \qquad \textbf{(5.1)}$$

Compared with EDS, the detection limit of WDS is around an order of magnitude better. At the same time a clearly higher spectral resolution of the X-ray spectrum can be reached. Advantage of measurements with EDS is the simultaneous measurement of the whole X-ray spectrum and with it the concurrent analysis of all elements, therefore, based on the lower analysis time, it is more often used for industrial applications [Br92].

Within this work, all EPMA measurements were preformed employing a MICROSPEC WDS-3PC WDS analysis system.

5.4 Transmission electron microscopy (TEM)

In transmission electron microscopy (TEM), an electron beam, generated by a filament within an electron gun, is accelerated, influenced by lens and condenser systems and impinges onto a very thin sample (around 200 nm thickness). Deflected as well as undeflected electrons, which penetrate the sample, are collected with a detector like a CCD camera or a fluorescent screen.

In principle, the construction of a TEM can be compared with a conventional light microscope, whereby the role of optical lenses is substituted by electrical lenses. Their generated magnetic field is able to spread and/or focus the electrons within the beam path. Depending on the type of electrons penetrating the sample (scattered or non-scattered electrons), the interpretation of results can usually be done by diffraction patterns or position-space images. Based on the highly energetic beam of electrons (300 -

400 kV), their interaction with the sample material and the formation of characteristic particles and radiations, several further techniques for investigations are known, i.e. electron energy loss spectroscopy (EELS), energy filtered TEM (EFTEM), high resolution TEM (HR-TEM), etc. A simple schematic of a TEM system is shown in Fig. 5.5 [Al97,Br92,Fl95].

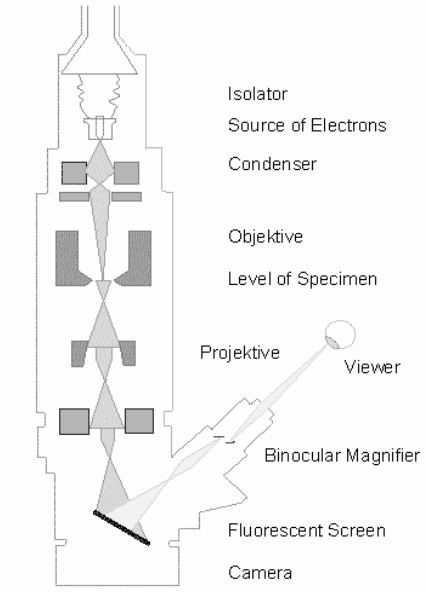

Figure 5.5: Schematic of a TEM [Biol].

In TEM, the high spatial resolution is based on the sum of some technical aspects. A highly focused electron beam (spot-size is in the µm range or below) with very coherent, monoenergetic electrons in combination with their high acceleration voltage (i.e. the wavelength of 100 kV electrons is only 0.0037 nm, thus much smaller than X-rays or neutrons) and the very thin samples allow magnifications up to 10^6. A further increase of the acceleration voltage up to 400 kV (corresponds to TEM systems in commercial practice) results in a minimized wavelength of 0.0016 nm (the theoretical instrumental point-to-point resolution is proportional to $\lambda^{3/4}$) and enables point-to-point resolutions better than 0.2 nm. Additionally, with the employment of modern computional applications like FFT (fast Fourier-Transformation), mathematical algorithms are used to enhance the quality of information. This technique enables e.g. to measure distances between atomic planes in HR-TEM images [Al97,Br92,Fl95].

As mentioned above, TEM offers two techniques of structure investigations. First, the image mode depicts the analysed sample where contrasts are based on differences in mass, thickness, density, crystallinity, and phase. Electron diffraction patterns enable to make statements about crystallinity. Single crystals form spot patterns on the screen, polycrystalls or powder produce ring patterns and glassy or amorphous materials generate series of diffuse halos. By distance measurements of points or rings, the phase composition can be determined. The SAED method (selected area electron diffraction) is based on this effect. There electron diffraction pattern are recorded only from areas as

small as several hundred nanometers in size, contrary to XRD, were the area is in the cm^2-range [Al97,Br92,Fl95].

Within this work, TEM investigations were peformed using a Philips CM20 operating at 200 kV, and a JEOL 3010 (HR-TEM) operating at 300 kV.

5.5 X-ray photoelectron spectroscopy (XPS)

X-ray photo electron spectroscopy (XPS), also called electron spectroscopy for chemical analysis (ESCA), is an analysis technique which is based on the photoelectric effect. It is an effective method for investigation of the chemical composition, the binding state of elements, as well as the oxidation number, or functionalities of solid surfaces. Due to its high sensitivity and the large number of obtainable chemical information, XPS is one of the most widespread surface analysis methods in material, polymer, semiconductor, and tool science [St08].

In this technique, the energy of a characteristic X-ray photon is transferred to a core electron of a sample atom. This results in an emitted photoelectron with a certain kinetic energy (E_{kin}) which can be measured with an energy analyzer. This process is described by the photoelectric effect, postulated by Einstein, with the following equation, which is also visualized in Fig. 5.6:

$$h\nu = E_{bind} + E_{kin} + \phi \qquad \textbf{(5.2)}$$

There hν is the energy of the X-ray photon, E_{bind} is the binding energy of the emitted core electron (photoelectron) and Φ is the spectrometer work function induced by the analyzer. This energetic term of Φ is necessary for the transfer from the Fermi level (E_F) to the vacuum level (E_{vac}) and depends on the respective used system; therefore this work function is calibrated using a reference metal such as Au or Pt [St08].

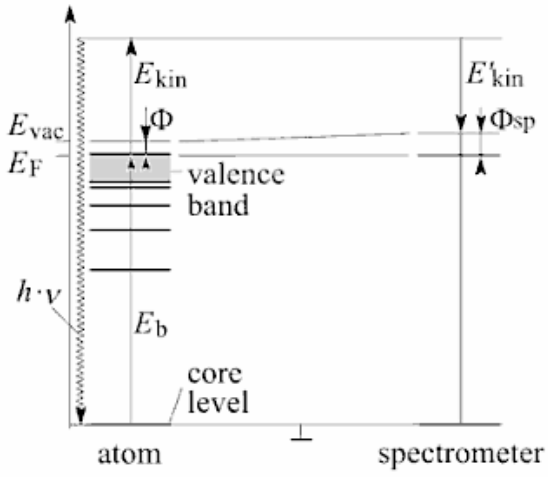

Figure 5.6: Energy schemata of the photoelectron emission process for XPS [St08].

The binding energy of a core electron depends not only on the electronic configuration of the particular atom, but also on the neighbouring atoms and binding partners. Hence, this

enables to make statements about the chemical composition and the binding situation of the constituent elements (chemical environment), respectively. The later one is based on a shift in the effective charge by liberation of the emitted core electron. This results in a deformation of the geometry of the valence orbitals and a change in the electronegativity of the involved atom partners. Furthermore, relaxation of the core electron vacancy influences the electronic state of the atom neighbourhood [St08].

XPS systems consist of an X-ray source, whereby usually the $K\alpha_{1,2}$ radiation of Al or Mg in combination with a crystal monochromator for line refinement is used. After escaping of photoelectrons from the sample surface, they get catched usually in a hemispherical anlyser to determine their kinetic energies. There, an electric field is applied and forces the linearly moving photoelectrons on a circular path. Corresponding to their kinetic energy and the varying applied field strength, a separation of the photoelectrons is done and their particular number is counted. All of these components are operating in ultra-high vacuum (UHV) below 10^{-8} mbar to prevent interactions and energy transfers to gas molecules, respectively [St08].

XPS measurement, presented in this work, were performed with an Omicron Multiprobe analysis system using a monochromized Al Kα X-ray beam with a resolution of > 0.2 eV.

5.6 X-ray diffraction (XRD)

In modern material science, X-ray diffraction (XRD) is one of the most used and most powerful methods for non-destructive characterization and identification of structural properties like strain state, grain size, phase composition, preferred orientation, texture, and defect structure.

Until now, around 75,000 diffraction patterns of different crystalline phases have been recorded and collected as standards for the main use of XRD, which is to identify crystalline structures in a sample by a search/match procedure. Another advantage of this technique can be found in the fact that the peak areas are related to the amount of each phase contained in the sample [Br92].

In an alternating electromagnetic field, every electron oscillates with the same frequency as the field. When an X-ray beam impinges on an atom, the frequency of the X-ray beam induces an equivalent oscillation of the electrons in the shell. As long as there is no ordered structure of the atoms as like in amorphous samples, the combining waves are out of phase in all directions, a destructive interference occurs and there is no resultant energy leaving the material. On the other hand, crystals are arranged in regular and periodic structures and patterns. Hence, in a very few directions, constructive interferences can be found. This results in the formation of waves which are in phase and leaving the material in various directions. Therefore, a diffracted beam can be explained as a beam composed of a large number of scattered rays mutually reinforcing one another. This phenomena also can be interpreted macroscopically by a reflexion of the incoming X-ray beam onto lattice planes and was postulated first 1912 by Bragg. The

Bragg´s law is cited in Equ. 5.1. In a typical experiment, the diffracted intensity is measured as a function of 2θ and the orientation, resulting in a diffraction pattern (see Fig. 5.7) [Br92,KL98].

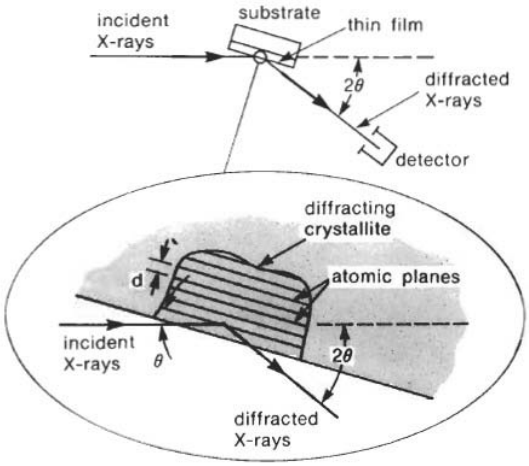

Figure 5.7: Schematic representation of the principle of XRD. Incoming X-rays get reflected on lattice planes and a detector counts their intensity [Br92].

Several techniques of XRD are established in physics, chemistry, life science or powder technology and depending on the technical performance and limits, they find more or less pronounced uses in the particular applied sciences. In thin film technology, the instrumentation and methods aim to maximise diffraction intensity in combination with minimized background noises due to the small sample thickness. The most common technique of XRD for investigation of preferentially and randomly orientated polycrystalline films is the Bragg-Brentano geometry. Hereby, slits collimate the incident X-rays which impinge on the specimen at an angle θ. After passing through receiving slits, the diffracted X-rays are detected. The specimen is rotated at one half the angular velocity of the detector (see Fig. 5.8) [Br92,Kl98].

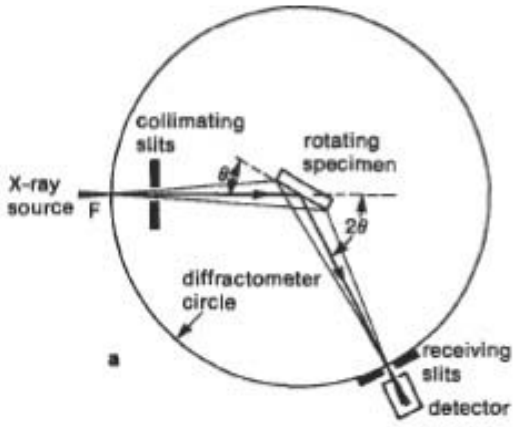

Figure 5.8: Geometry of the Bragg-Brentano mode [Br92].

The instrumentation of a Bragg-Brentano XRD unit consists typically of an X-ray source, a slit system to focus the beam, and a detector. The X-ray wavelength λ, emitted from an X-ray tube (anode material is usually Cu, Mo, or W) ranges typically at around 0.7-2 Å which corresponds to X-ray energies (E = 12.4 keV/Å) of ~ 6 - 17 keV.

Within this work, microstructural investigations were performed by Bragg-Brentano X-ray diffraction (XRD, Siemens D500) using Cu Kα radiation. The so obtained patterns were simulated by Rietveld analysis using the Topas 2.1 software package.

5.7 Hardness measurement

The hardness of materials is usually defined as resistance to permanent indentation. The general principle of hardness tests is that a hard indenter is pressed into the surface of a material to be tested under a specific load for a definite time interval, and a measurement is made of the size or depth of the indentation [Ly69].

The hardness (H_c) and elastic modulus (E_c) of coatings are commonly measured by elastic-plastic depth sensing indentation methods. Hereby, the load of an indenter with well-defined geometry is increased/decreased in small steps while the displacement is recorded at every increment. The material properties H and E are determined from a complete cycle of loading and unloading (see Fig. 5.9).

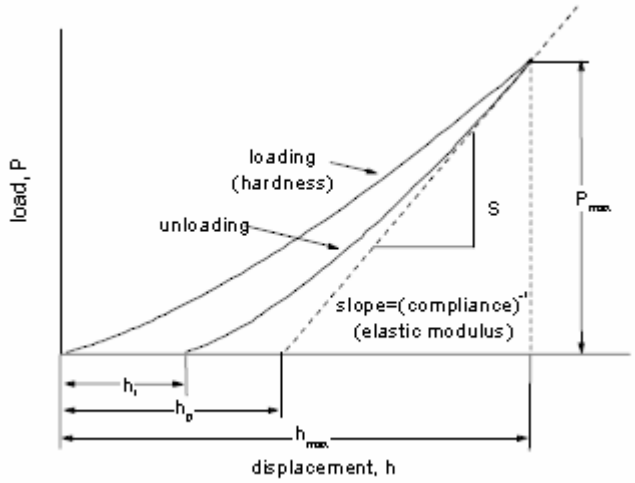

Figure 5.9: Schematic of a depth sensing indentation load-displacement curve [Ma01b].

The hardness of coatings can be calculated with the following equation:

$$H_c = \frac{P}{A} \qquad \textbf{(5.3)}$$

where A is the contact area at peak load P. On the other hand, the elastic modulus of the coatings E_C, also termed Young´s modulus, can be calculated from Equ. 5.4:

$$E_C^* = \frac{E_C}{1 - \nu_c^{\,2}} \qquad \textbf{(5.4)}$$

where E_c^* is the reduced elastic modulus and v is the Poisson´s ratio. Experimentally, E_c^* is determined from the slope of the unloading curve in Fig. 5.9.

For ceramic hard coatings on steel or silicon substrates, the indentation depth should be in the range of 10 % of the coating thickness to prevent interactions with the substrate material and minimize substrate interference which would result in destorted results [Bü61].

Within this work, all hardness and elastic modulus measurements were performed using a computer aided Fischerscope H100C equipped with a Vickers diamond indenter which was calibrated following the built-in procedures on fused silica. The maximum load was varied between 15 and 50 mN to achieve an indentation depth of about 10 % of the coating thickness.

5.8 Biaxial stress temperature measurement (BSTM)

Residual stresses represent a polyaxial and elastic state of stress, formed without outer force effects, and can be subdivided into an intrinsic and extrinsic amount. Intrinsic stresses are generated during deposition based on nucleation and growth processes (see chap. 3.4); on the other hand, extrinsic stresses are the result of different coefficients of linear thermal expansion of the substrate and the coating and vary with temperature.

Stresses always act in all three dimensions. For very thin coatings (substrate thickness is hundred or more times higher than the coating thickness), the amount of stresses in the z-directions can be neglected and the residual stresses only act in the x- and y-direction. In this case the residual biaxial stresses can be calculated with the modified Stoney equation:

$$\sigma = \frac{E_S}{1 - v_S} \frac{{t_S}^2}{6 t_C} \left(\frac{1}{r} - \frac{1}{r_0} \right) \qquad \textbf{(5.5)}$$

There, σ is the biaxial stress, $E_S/1\text{-}v_S$ is the biaxial elastic modulus, E_S is the elastic modulus of the substrate, v_S is the Poisson´s ratio of the substrate, t_S and t_C are the substrate and coating thickness, respectively, and r_0 and r are the initial radius and the curvature radius measured with BSTM at the respective temperature [Ho76,Wi69].

BSTM can be performed by means of the substrate curvature method at different temperatures. Hereby a sample (Si-substrate), coated on one side, is placed with the coated side onto a heatable glass plate within a measurement chamber. This chamber can be heated up to determine the biaxial stresses at different temperatures. Normally this measurement takes place in an evacuated atmosphere to avoid oxidation of the coating. To determine the curvature of the coating-substrate-system, two parallel laser beams with their distance d_0 first are reflected from the backside of the polished substrate and afterwards reflected again from a mirror, placed on the top of the measurement equipment. After these two reflections, the beams are screened onto the measurement

plane and the distance can be determined. A schematic of such a BSTM unit is shown in Fig. 5.10.

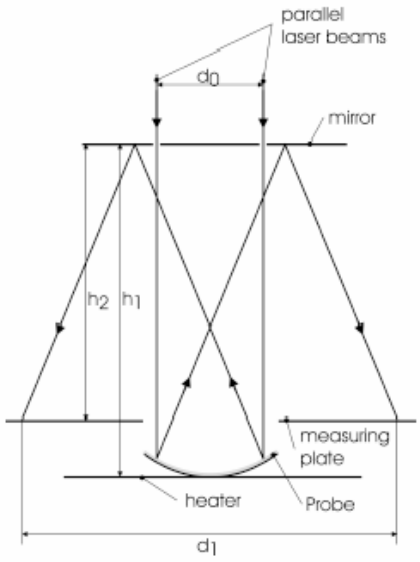

Figure 5.10: Schematic of the substrate curvature method [Ma01b].

The curvature radius r, essential for the Stoney equation, can be calculated by the geometric condition:

$$r = \frac{2(h_1 + h_2)d_0}{d_0 - d_1} \qquad \textbf{(5.6)}$$

There, h_1 is the distance between sample plane and the mirror, h_2 is the distance between measurement plane and mirror, d_0 is the distance between the two laser beams, and d_1 is the distance of the two projected laser beams on the measurement plane after their reflections.

Within this work, BSTM was performed with a homemade equipment used for continuous stress-temperature investigations up to 700°C; a more detailed description can be found in Ref. [Wi97].

5.9 Ball-on-disk measurement

The tribological behaviour of the coatings, discussed in this work, were investigated with dry sliding ball-on-disk tests at room temperature and a humidity of around 40 % using a CSM tribometer. A schematic representation of a tribometer is shown in Fig. 5.11. There are several types in use but in generally, they are based on the same concept. A substrate is mounted and fixed on a rotating sample holder and contacted by a counterbody (pin, ball, cone, disk, etc.). Typical parameters for tribotests are the rotation velocity, the radius of the wear track and length of sliding distance, the type and geometry of the counterbody, the contact force as well as the temperature or the environmental

medium (ambient air, water, oil bath, etc.). The output data describe the respective friction coefficient as a function of the distance.

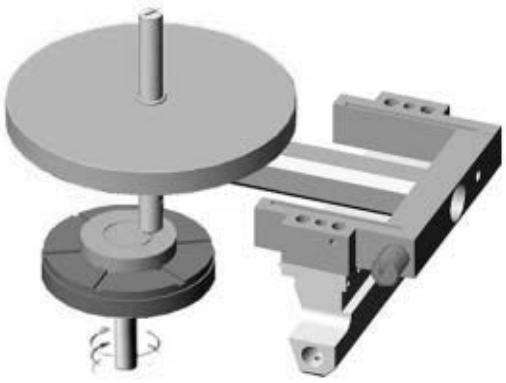

Figure 5.11: Schematic of a ball-on-disk tribometer [csmi].

The tribotests were performed with coated high speed steel (HSS) substrates and alumina balls with 6 mm diameter as counterbody. The sliding distance was chosen between 300 and 500 m, the rotation velocity was kept constant with 10 cms^{-1} and the load was varied between 2 and 5 N.

5.10 White light interferometry

After ball-on-disk tests, the wear tracks were investigated with a white-light interferometer, also termed optical profiler. With this technique, the surface topography can be visualised by a three-dimensional surface profile measurement in a non-contact mode which allows the quantification of important parameters like roughness, evenness, depth profiles etc. Modern white light interferometers consist of a source of light with a coherence length in the µm-range (i.e. tungsten halogen light), a beam splitter, a reference surface (mirror), and a CCD camera with an objective system. Additionally, several optical gears like lenses, blends, and filters are involved (see Fig. 5.12).

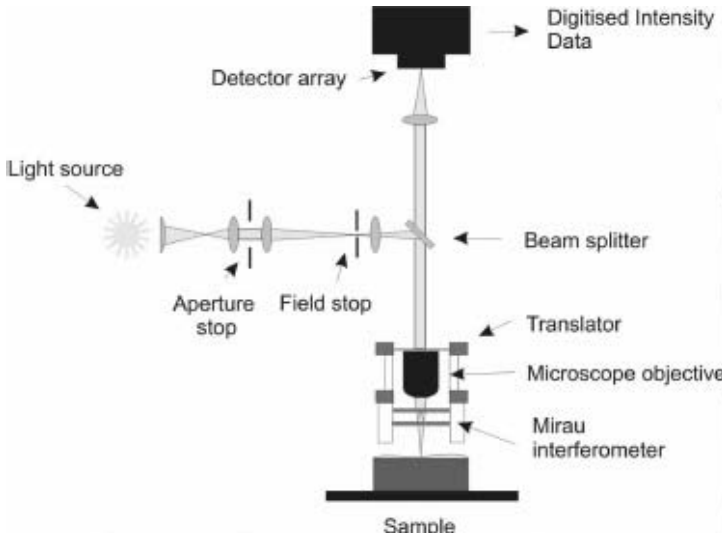

Figure 5.12: Schematic of a white light interferometer [mntg].

The interferometer beam splitter reflects half of the incident beam to the reference mirror within the interferometer. The beams reflected from the sample surface and the reference surface recombine and form interferences fringes. For measurement, a piezoelectric transducer linearly moves the reference surface in small, known steps which causes a phase shift between the reference and the sample beams. Hereby, at every point of the sample surface, differing relative to the reference surface, interference occurs. A detector system within the CCD camera records the intensity of the formed interference pattern at many different relative phase shifts. The evaluation is provided by a conversion of the intensity to wave front (phase) data by integrating the intensity data. The software evaluates these variations and assigns a height value for every recorded pixel [Ve00b].

Within this work, a qualitative evaluation of surfaces of coated HSS-substrates after tribotesting was performed with a Veeco NT 1100 optical profiler system and magnifacitions were chosen between 1:5 and 1:50. This system is able to measure topographic structures between 150 nm and 1 mm, depending on the adjusted interferometry mode (shifting or scanning mode).

6 Summary and conclusions

CrN protective coatings grown by physical vapour deposition (PVD) are widely used in tool applications due to their advantageously wear resistance, corrosion inertness, and oxidation behaviour. These properties are also the reason for their use in automotive applications as protective coatings for piston/liner systems and in drivetrain. Nevertheless, in these applications, a permanent improvement of the frictional behaviour including friction reduction is necessary to achieve decreased CO_2 as well as particle emission.

Within this work, as strategy to reduce the friction coefficient of CrN-based coatings, films with different BN and MS_2 (M = Mo, W) contents were reactively deposited on a laboratory-scale unbalanced magnetron sputter system. For synthesis of these composite films, several target materials (CrB_2, Cr with 20 at.% B, and a Cr target with inlays of MoS_2 and WS_2) were taken and deposited in an Ar/N_2 atmosphere with varying partial pressures of N_2 (between 0 and 64 % of the total pressure). Selected coatings were investigated employing scanning electron microscopy (SEM), electron probe micro analysis (EPMA), X-ray photoelectron spectroscopy (XPS), X-ray diffraction (XRD), high resolution transmission electron microscopy (HR-TEM), microindentation, biaxial stress temperature measurements, ball-on-disk dry sliding tests, and white-light optical profilometry.

The main findings, resulting from these investigations, were released in four publications, which are presented in the attachement to this work. Furthermore, a short overview of the chosen strategies including their main handicaps to achieve the low friction and self-lubricating properties, respectively, is shown in Figure 6.1 and will be discussed in this chapter.

CrBN coatings, deposited employing a CrB_2 target, exhibit a structural evolution depending on the nitrogen partial pressure p_{N2}. Without nitrogen a columnar hexagonal CrB_2 structure can be obtained wich transforms into a nc-CrB_2/a-phase, further into a dual-phase amorphous structure and finally into a nc-CrN/a-BN phase by increasing p_{N2}. This evolution coincides with conducted XPS, XRD and TEM investigations, and reflects the obtained mechanical properties. Within the CrBN-system, most promising candidates with self-lubricating properties due to the amount of CrN and BN are coatings deposited at high p_{N2}. However, FFT-HR-TEM studies showed that the formed BN phase is highly distorted with no preferred orientation and hexagonal domains extending only over a few atomic layers (cp. Fig. 6.1, where these domains are marked in the HR-TEM images on the upper left side of this schematic). Consequently, this BN phase is not able to develop a low-friction effect by easy shearing during tribological contacts.

Based on these attainments, as second way to achieve self-lubricating CrBN coatings, the use of a Cr-target with addition of 20 at.% B was chosen. There, an amorphous Cr-rich structure is obtained at lower p_{N2}, which transforms to a nano-crystalline nitride-based structure within the Cr_2N–CrN–BN phase field. Beyond that, the nitrogen concentration saturates resulting in CrN crystals embedded in an amorphous BN matrix (see also Fig.

6.1 for the XRD patterns indicate a saturated CrN structure, where the existence of BN was proven by XPS).

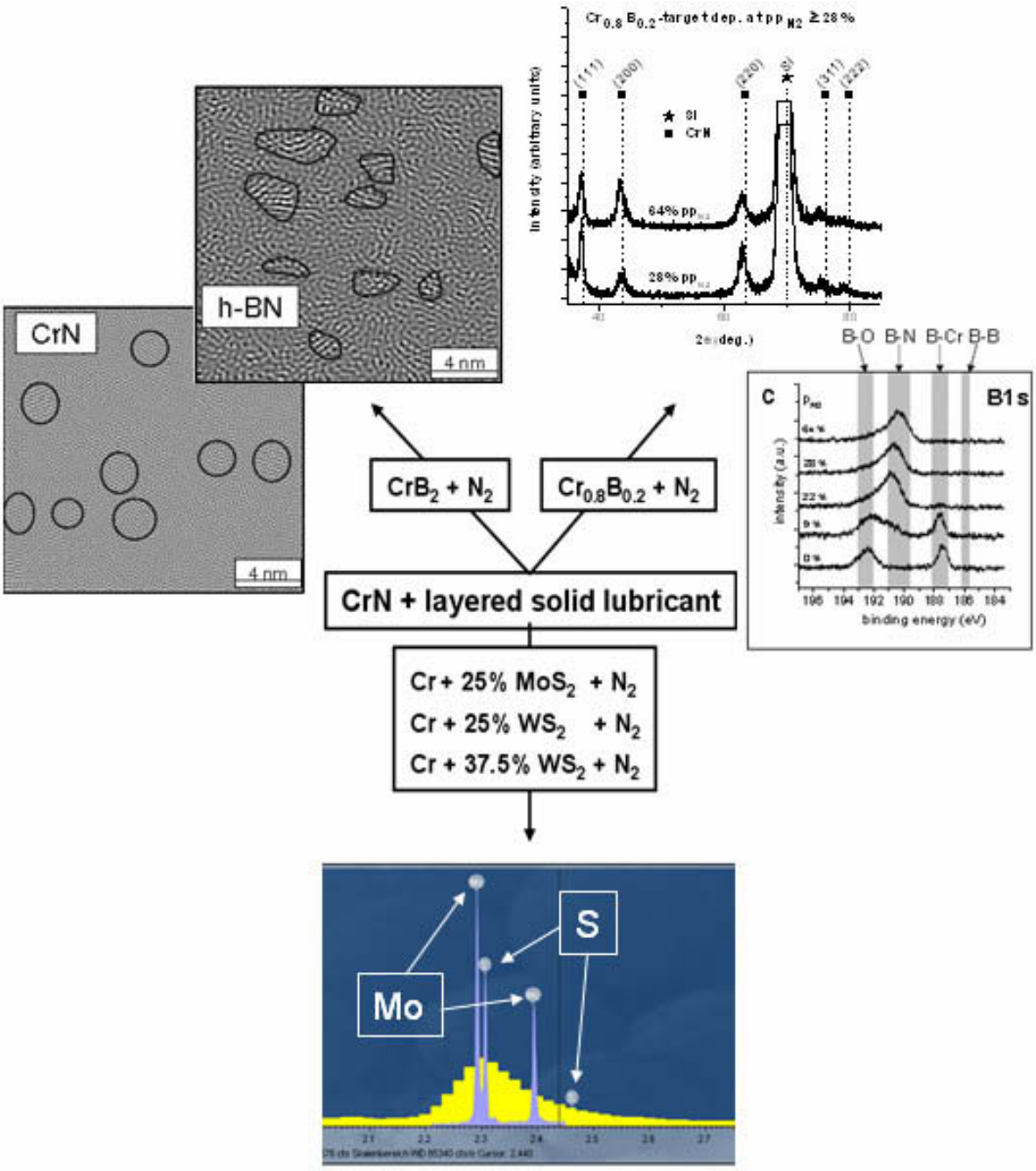

Figure 6.1: Schematic showing the chosen strategies to obtain self-lubricating CrN-based hard coatings. The representative selected pattern and diagrams visualize the structural evolution within these systems.

The understoichiometric coatings deposited at low p_{N2} exhibit only moderate hardness and elatic modulus, respectively, which is maintained even for the coating within the ternary Cr_2N–CrN–BN phase field presumably due to the large fraction of amorphous BN. However, a dramatic increase in hardness is obtained as soon as the nitrogen concentration saturates for the CrN–BN dual phase structure, whereas the elastic modulus increases only moderately. This can be understood by the nano-composite

structure of these coatings where sub-10 nm CrN grains are surrounded by a few monolayers of BN. For that reason, the hardness of the CrBN coatings synthesized at high p_{N2} exceeds the values commonly observed for CrN substantially. The BN phase, on the other hand, does not provide for a solid lubrication effect, as the coefficient of friction is comparable to pure CrN coatings.

As second strategy to achieve self-lubricating hard coatings, the combination of CrN with transition-metal dichalkogenide structures was investigated within this work. Irrespective of the chosen type (MoS_2 and WS_2) and target inlay area coverage (25 and 37.5 %), the results obtained for both systems are very similar. With increasing p_{N2}, the structure transforms from a Cr dominated one via Cr_2N and finally reaches an understoichiometric CrN_x based structure. According to the predominant morphology, the hardness and elastic modulus reach their lowest values for coatings deposited without N_2 and the highes values for CrN dominated structures. Indications for the presence of Mo-S and W-S bondings in the coatings were found by XPS and XRD, but did not affect the mechanical properties as well as the tribological behaviour of the investigated coatings. This is based on the substoiciometric composition of the MS_x phase, which is representatively shown in the lower part of Fig. 6.1. Increasing p_{N2} fosters the substoiciometry resulting in a nearly complete loss of sulphur in the films. This phenomenon results in the impossibility of formation of nanoscaled layered grains, which enable self-lubrication.

The friction coefficients for all coatings, deposited and discussed in this work, were in the range of ~ 0.5 – 0.7 due to low BN grain size and understoichiometry of MeS_2 and not suitable for friction reduction as well as self-lubricity. Nevertheless, the Cr-B-N system has been shown to be suitable to increase wear resistance, compared to standard CrN.

As a basic principle of this work, the interrelationship between growth, microstructure, and properties was investigated scientifically for a new class of materials which might show high future potential for several applications.

7 References

[Al00] A. Albu-Yaron, C. Lévy-Clément, A. Katty, S. Bastide, R. Tenne, Thin Solid Films, 361-362, 223, 2000.

[Al97] H. Alexander, Physikalische Grundlagen der Elektronenmikroskopie, B, G. Teubner, Stuttgart, 1997.

[An97] R.A. Andrievski, J. Solid State Chem., 133, 249, 1997.

[Ar91] R.D. Arnell, P.B. Davis, J. Halling, T.L. Whomes, Tribology, Springer, New York, 1991.

[Ar98] E. Arzt, Acta Mater., 46, 5611, 1998.

[As04] M.N.R. Ashfold, F. Claeyssens, G.M. Fuge, S.J. Henley, Chem. Soc. Rev., 33, 23, 2004.

[Au99] W. Auwärter, T.J. Kreutz, T. Greber, J. Osterwalder, Surf. Sci., 429, 229, 1999.

[Ba00] F.W. Bach, T. Duda, Moderne Beschichtungsverfahren, WILEY-VCH, 2000.

[Ba02] R.G. Bayer, Wear Analysis for Engineers, HNB, New York, 2002.

[Ba80] C.S. Barrett, T.B. Massalski, Structure of Metals, Pergamon Press, Oxford, 1980.

[Ba97] P.B. Barna and M. Adamik, in Y. Pauleau, P.B. Barna (Eds.), Protective Coatings and Thin Films: Synthesis, Characterization, and Applications, Kluwer Academic Publishers, Dordrecht, 279, 1997.

[Ba98] P.B. Barna, M. Adamik, Thin Solid Films, 317, 27, 1998.

[Be93] K. Bewilogua, H. Dimigen, Surf. Coat. Technol., 61, 144, 1993.

[Be97] T. Bell, New Directions in Tribology, eds. I.M. Hutching, Mechanical Engineering Publications, London, 1997.

[Be99] M. Benda, J. Musil, Vacuum, 55, 171, 1999.

[Bh01] B. Bushan, Modern Tribology Handbook, Vol. II, CRC Press, Boca Raton, 2001.

[Bh99] B. Bushan, Principles and Applications of Tribology, John Wiley, New York, 1999.

[Bi96] M. Bin-Sudin, A. Leyland, A.S. James, A. Matthews, J. Housden, B. Garside, Surf. Coat. Technol., 81, 215, 1996.

[Biol] http://www.biologie.uni-hamburg.de/b-online/d03/03e.htm#resolel, 27.07.2009.

[Bl89] P.J. Blau, Friction and Wear Transitions of Metals, Noyes Publications, New Jersey, 1989.

[Bo01] F.P. Bowden, D. Tabor, The Friction and Lubrication of Solids, Clarendon Press, Oxford, 2001.

[Bo50] F.P. Bowden, D. Tabor, Friction and Lubrication of Solids, Clarendon Press, Oxford, Part I, 1950, Part II, 1964.

[Bo92] R. L. Boxman, S. Goldsmith, Surf. Coat. Technol., 52, 39, 1992.

[Bo99] J. Boudiombo, J.C. Loulergue, A. Bath, P. Thevenin, Mater. Sci. Eng., B, 59, 244, 1999.

[Br92] C.R. Brundle, C.A.E. Evans, S. Wilson, Encyclopedia of Materials Testing, Surfaces, Interfaces, Thin Films, Elsevier Butterworth-Heinemann, Stoneham, 1992.

[Bu00] R.F. Bunshah, Handbook of Hard Coatings: Deposition Technolgies, Properties and Applications, Noyes Publications, 2000.

[Bu04] B. Bushan, M. Nosonovsky, Acta Materialia, 52, 8, 2004.

[Bü61] H. Bückle, VDI-Ber., 41, 14, 1961.

[Bu85] R.F. Bunshah, C.V. Deshpandey, J. Vac. Sci. Technol. A, 3,553, 1985.

[Bu87] P.J. Burnett, D.S. Rickerby, Thin Solid Films, 148, 41, 1987.

[Bu96] J.S. Burnell-Gray, P.K. Datta, Surface Engineering Casebook, Woodhead Publishing Limiting, Cambridge, 1996.

[Bu99] B. Bushan, Principles and Applications of Tribology, John Wiley, New York, 1999.
[Ca03] S. Carrera, O. Salas, J.J. Moore, A. Woolverton, E. Sutter, Surf. Coat. Technol., 167, 25, 2003.
[Ca07] C. Carlton, P.J. Ferreira, Mater. Res. Soc. Symp. Proc., Vol. 976, 2007.
[Ca96] R.W. Cahn, P. Haasen, Physical Metallurgy, 4th ed. Cambridge Univ Press, 1996.
[Ch80] B.N. Chapman, Glow Discharge Processes, John Wiley, New York, 1980.
[Ch84] F.F. Chen, Plasma Physics and Controlled Fusion, Plenum Press, New York, 1984.
[Ch92] X. Chu, M.S. Wong, W.D. Sproul, S.L. Rohde, S.A. Barnett, J. Vac. Sci. Technol. A, 10, 1604, 1992.
[Ch99] B. Choi, Mater. Res. Bull., 34, 14/15, 2215, 1999.
[Co92] Q. Cong, D. Yu, J. Wang, Y.J. Ou, Thin Solid Films, 209, 1, 1992.
[Co98] S.R. Cohen, L. Rapoport, E.A. Ponomarev, H. Cohen, T. Tsirlina, R. Tenne, C. Levy-. Clement, Thin Solid Films, 324, 190, 1998.
[csmi] http://www.csm-instruments.com/en/Tribometer, 16.05.2009.
[Di98] M. Diserens, J. Patscheider, F. Levy, Surf. Coat. Technol., 108/109, 241, 1998.
[DI-a] DIN 1.3505
[Do04] C. Donnet, A. Erdemir, Tribological Letters, Vol. 17, No.3, 2004.
[Do95] C. Donnet, Condensed Matter News, 4(6), 9, 1995.
[Do96] C. Donnet, J.M. Martin, T. Le Mogne, M. Belin, Tribol. Int., 29, 123, 1996.
[Do98] C. Donnet, Surf. Coat. Technol.,100–101, 180, 1998.
[Ei01] G. Eisenbrand, M. Metzler, Toxikologie für Naturwissenschaftler und Mediziner, Georg Thieme, Stuttgart, 2001.
[El01] A. El-Yadouni, A. Soltani, A. Boudrioua, P. Thevenin, A. Bath, J.C. Loulergue, Opt. Mater., 17, 319, 2001.
[En97] W. Ensinger, Nucl. Instr. Meth. Phys. Res. B, 127/128, 796, 1997.
[Er00a] A. Erdemir, Tribology Letters, 8, 97,2000.
[Er00b] A. Erdemir, O.L.Eryilmaz, G.Fenske, J. Vac. Sci. Technol. A, 18, 1987, 2000.
[Er00c] A. Erdemir, O.L. Eryilmaz, I.B. Nilufer, G. Fenske, Diamond Relat. Mater., 9, 632, 2000.
[Er01] A. Erdemir, C. Donnet, In: B. Bhushan, editor. Modern Tribology Handbook, Vol. II, CRC Press, Boca Raton; 2001.
[Er40] H. Ernst, M.E. Merchant, Surface -Friction between Metals – a basic factor in the metal cutting process, Proc. Special Summer Conf. on Fricton and Surface Finish, MIT Press, Cambridge,1940.
[Er96] A. Erdemir, C. Bindal, G.R. Fenske, C. Zuiker, R. Csencsits, A.R. Gruen, D.M. Gruen, Diamond Films and Technology, 6, 31, 1996.
[Es93] M.L. Escrivao, A.M.C. Moutinho, M.J.P. Maneira, Journal of Nuclear Materials, 200, 300, 1993.
[Fi87] H. Fischmeister and H. Jehn, Hartstoffschichten zur Verschleissminderung, DGM Informationsgesellschaft, Stuttgart, 1987.
[Fl95] S.L. Flegler, J.W. Heckman, K.L. Klomparens, Elektronenmikroskopie-Grundlagen-Methoden-Anwendungen, Spektrum Akademischer Verlag, Heidelberg,1995.
[Fr90] G. Franz, Oberflächentechnologie mit Niederdruckplasmen, Springer, Berlin, 1994.
[Fu97] W. Fukarek, O. Kruse, A. Kolitsch, W. Möller, Thin Solid Films, 308-309, 38,1997.
[Ga05] G. Gassner, P. Mayrhofer, C. Mitterer, J. Kiefer, Surf. Coat. Technol., 200, 1147, 2005.
[Ga87] K.-H. Zum Gahr, Microstructure and Wear of Materials, Elsevier, Amsterdam, 1987.
[Ga91a] F.S. Galasso, Chemical Vapor Deposited Materials, CRC Press, Boca Raton 1991.
[Ga91b] J. Ganz, Metalloberfläche, 45, 11, 1991.

[Ga97] A.K. Gangopadhyay, P.A. Willermet, M.A. Tamor, W.C. Vassell, Tribol. Int., 30, 9, 1997.
[Gi94] W. Gissler, Surf. Coat. Technol., 68/69, 556, 1994.
[Gi96] S. Gimeno, J.L. Andújar, E. Bertran, A. Lousa, Diamond. Rel. Mater., 5, 535, 1996.
[Gi97] W. Gissler, M.A. Baker, J. Haupt, P.N. Gibson, R. Gilmore, T.P. Mollart, Diamond Films Technol., 7, 165, 1997.
[Gi98] R. Gilmore, M.A. Baker, P.N. Gibson, W. Gissler, M. Stoiber, P. Losbichler, C. Mitterer, Surf. Coat. Technol.,108-109, 345, 1998.
[Go01] G. Gottstein, Physikalische Grundlagen der Materialkunde, Springer, Berlin/Heidelberg, 2001.
[Go98] R.J. Goldston, P.H. Rutherford, Plasmaphysik – Eine Einführung, Friedr. Vieweg, Braunschweig/Wiesbaden, 1998.
[Gr52] W.R. Grove, Phil. Trans. Roy. Soc., London, 142, 87, 1852.
[Gr84] C.R.M. Grovenor, H.T.G. Hentzell, D.A. Smith, Acta Metall., 32(5), 773, 1984.
[Gr93] J.E. Greene, In D.T.J. Hurle (ed.), Handbook of Crystal Growth, Vol. 1, Elsevier Science Publishers, Amsterdam, 640, 1993.
[Gr94] A. Grill, Cold Plasma in Materials Fabrication, IEEE Press, New York, 1994.
[Gr99] A. Grill, Diamond Rel. Mater., 8, 428, 1999.
[Gu96] Y.Y. Guu, J.F. Lin, C.-F. Al, Wear, 194, 12, 1996.
[Ha51] E.O. Hall, Proc. Phys. Soc. B, 64, 747, 1951.
[Ha78] P. Haasen, Physical Metallurgy, Cambridge University Press, London, 1978.
[Ha87] R.A. Haefer, Oberflächen und Dünnschicht-Technologie, Springer, Berlin, 1987.
[Ha92] I.P. Hayward, I.L. Singer, L.E. Seizman, Wear,157, 215, 1992.
[Ha94] P. Hammer, A. Steiner, R. Villa, M. Baker, P.N. Gibson, J. Haupt, W. Gissler, Surf. Coat. Technol., 68/69, 194, 1994.
[He87] U. Helmersson, S. Todorova, S.A. Barnett, J.E. Sundgren, L.C. Markert, J.E. Greene, J. Appl. Phys., 62, 481, 1987.
[Hi96] J.P. Hirvonen, J. Koskinen, J.R. Jervis, M. Nastasi, Surf Coat Technol., 80, 139, 1996.
[Ho00a] K. Holmberg, H. Ronkainen, A. Matthews, Ceramics Int., 26, 787, 2000.
[Ho00b] P. Holubar, M. Jilek, M. Sima, Surf. Coat. Technol., 145, 133, 2000.
[Ho01] K. Holmberg, A. Matthews, in: B. Bhushan (ed.), Modern Tribology Handbook, Vol. II, CRC, Boca Raton, 2001.
[Ho76] R.W. Hoffmann, Thin Solid Films, 34, 185, 1976.
[Ho84] D.M. Hoffman, G.L. Doll, P.C. Eklund, Phys. Rev. B, 30, 6051, 1984.
[Ho85] Holleman-Wiberg, Lehrbuch der Anorganischen Chemie, 91-100. Auflage, Walter de Gryter Verlag, Berlin/New York, 1985.
[Ho89a] M.G. Hocking, V. Vasantasree, P.S. Sidky, Metallic and Ceramic Coatings, Longman Scientific & Technical, Essex, 1989.
[Ho89b] H. Holleck, Metall, 43/7, 614,1989.
[Ho94] K. Holmberg, A. Matthews, Coating Tribology: Properties, Techniques and Applications in Surface Engineering, Elsevier, Amsterdam, 1994.
[Ho98] K. Holmberg, A. Matthews, H. Ronkainen, Tribol. Int., 31(1-3), 107, 1998.
[Hu00] J. Huang, Y.T. Zhu, Defects and Diffusions Forum, 186-187, 1, 2000.
[Hu08] J.J. Hu, R. Wheeler, J.S. Zabinski, P.A. Shade, A. Shiveley, A.A. Voevodin, Tribol. Lett., 32, 49, 2008.
[Hu96] T. Hurkmans, D.B. Lewis, J.S. Brooks, W.D. Münz, Surf. Coat. Technol., 86/87, 192, 1996.
[Iv94] I. Ivanov, P. Kazansky, L. Hultman, I. Petrov, J.-E. Sundgren, J. Vac. Sci. Technol. A, 12(2), 314, 1994.

[Ja85] JANAF Thermochemical Tables, 3rd ed., edited by M.W. Chase, C.A. Davies, J.R. Downey, D.J. Fruip, R.A. McDonald, and A.N. Syverud, J. Phys. Chem. Ref. Data., 14, 1985.

[Ja93] W. Jacob, W. Moller, Appl. Phys. Lett., 63, 1771, 1993.

[Je92] H.A. Jehn in W. Gissler, H.A. Jehn (eds.), Advanced Techniques for Surface Engineering, Kluwer, Dordrecht, 1992.

[Ji04] Y. Jing, J. Luo, S. Pang, Thin Solid Films, 461, 288, 2004.

[Jü87] B. Jüttner, IEEE Trans. Plasma Sci., 15, 474, 1987.

[Ka00a] K. Kato, Wear, 241, 151, 2000.

[Ka00b] L. Karlsson, L. Hultman, J.E. Sundgren, Thin Solid Films, 371, 167, 2000.

[Ka02] L. Karlsson, A. Hörling, M.P. Johansson, L. Hultman, G. Ramanath, Acta Mater., 50, 5103, 2002.

[Ka03] P.Karvankova, Superhard nc-TiN/a-BN/a-TiB_2 and nc-MnN/a-metal nanocrystalline composite coatings, PhD thesis, Technical University Munich, 2003.

[Ka04] P. Karvankova, M.G.J. Veprěk-Heijman, M. Zawrah, S. Veprěk, Thin Solid Films, 467, 133, 2004.

[Ke86] A. Kelly, N.H. MacMillan, Strong Solids, Clarendon Press, Oxford, 1986.

[Ke99] E. Kelesoglu, C. Mitterer, M.K. Kazmanli, M. Ürgen, Surf. Coat. Technol., 116-119, 133, 1999.

[Ki91] D.S. Kim, T.E. Fischer, B. Gallois, Surf. Coat. Technol., 49, 537, 1991.

[Ki95] G. Kienel, K. Röll, Vakuumbeschichtung 2, Verfahren und Anlagen, VDI-Verlag, Düsseldorf, 1995.

[Ki98] H.S. Kim, Scripta Mater., 39, 57, 1998.

[Kl98] W. Kleber, H.J. Bautsch, J. Bohm, Einführung in die Kristallographie, 18. Auflage, Verlag Technik Berlin, 1998.

[Kn86] O. Knotek, M. Böhmer, T. Leyendecker, J. Vac. Sci. Technol. A, 4, 2695, 1986.

[Kn92] O. Knotek, A. Schrey, J.W. Schultze, B. Siemensmeyer, Werkst. Korros., 43, 511, 1992.

[Kn96] O. Knotek, E. Lugscheider, F. Löffler, B. Bosserhoff, S. Schmitz, Mater. Sci. Eng. A, 209, 394, 1996.

[Kn97] O. Knotek, F. Löffler, C. Barimani, G. Kraemer, in R.P. Agarwala (Ed.), Surface Coatings for Advanced Materials, Trans. Tech. Publications, New Hampshire, 61, 1997.

[Ko07] Y. Kobayashi, T. Nakamura, T. Akasaka, T. Makimoto, N. Matsumoto, J. Crystal. Growth, 298, 325, 2007.

[Ko70] J.S. Koehler, Phys. Rev. B, 2, 547, 1970.

[Ku05] K. Kutschej, Wear Resistant, Low Friction Hard Coatings for Cutting Applications, PhD thesis, University of Leoben, 2005.

[Kv78] I. Kvernes, P. Fartum, Thin Solid Films, 53, 259, 1978.

[La96] M. Larsson, P. Hollman, P. Hedenqvist, S. Hogmark, U. Wahlström, L. Hultman, Surf. Coat. Technol., 86/87, 351, 1996.

[Le00] Y. LeGodec, D. Martinez-Garcia, V.L. Solozhenko, M. Mezouar, G. Syfosse, J.M. Besson, J. Phys. Chem. Solids, 61, 1935, 2000.

[Le91] T. Leyendecker, O. Lemmer, S. Esser, J. Ebberink, Surf. Coat. Technol., 48, 175, 1991.

[Li89] J.R. Lince, T.B. Stewart, M.M. Hills, P.D. Fleischauer, J.A. Yarmoff, A. Taleb-Ibrahimi, Surf. Sci., 210, 387, 1989.

[Li94] M.A. Lieberman, A.J. Lichtenberg, Principles of Plasma Discharges and Materials Processing, John Wiley, New York, 1994.

[Li95] J.R. Lince, M.R. Hilton, A.S. Bommannavar, Thin Solid Films, 264, 120, 1995.

[Li96] Y. Liu, A. Erdemir, E.I. Meletis, Surf. Coat. Technol., 86-87, 564, 1996.
[Lo97a] P. Losbichler, C. Mitterer, Surf. Coat. Technol., 97, 567, 1997.
[Lo97b] P. Losbichler, C. Mitterer, P.N. Gibson, W. Gissler, F. Hofer, P. Warbichler, Surf. Coat. Technol., 94/95, 297, 1997.
[Lo98] P. Losbichler, Ultraharte PVD-Schichten im System Ti-B-N, PhD thesis, University of Leoben, 1998.
[Lo99] K.P. Loh, I. Sakaguchi, M.N. Gamo, S. Tagawa, T. Sugino, T. Ando, Appl. Phys. Lett., 74, 28, 1999.
[Ly69] V.E. Lysaght, A. DeBellis, Hardness testing handbook, American Chain and Cable Co., Page-Wilson Corporation, USA, 1969.
[Ma01a] P.H. Mayrhofer, G. Tischler, C. Mitterer, Surf. Coat. Technol., 142–144, 78, 2001.
[Ma01b] P.H. Mayrhofer, Materials Science Aspects of Nanocrystalline PVD Hard Coatings, PhD thesis, University of Leoben, 2001.
[Ma02a] A. Matthews, Vacuum, 65, 237, 2002.
[Ma02b] I. Martin-Litas, P. Vinatier, A. Levasseur, J.C. Dupin, D. Gonbeau, F. Weill, Thin Solid Films, 416, 1, 2002.
[Ma02c] P.H. Mayrhofer, F. Kunc, J. Musil, C. Mitterer, Thin Solid Films, 415, 151, 2002.
[Ma03] P.H. Mayrhofer, A. Hörling, L. Karlsson, J. Sjölén, C. Mitterer, L. Hultman, Appl. Phys. Lett., 83, 10, 2049, 2003.
[Ma04] P.H. Mayrhofer, Nanostructural Design of Hard Thin Films, University of Leoben, Habilitation thesis, 2004.
[Ma05] P.H. Mayrhofer, C. Mitterer, J.G. Wen, J.E. Greene, I. Petrov, Appl. Phys. Lett., 86, 131909, 2005.
[Ma06] P.H. Mayrhofer, C. Mitterer, L. Hultman, H. Clemens, Prog. Mater. Sci., 51, 2006.
[Ma64] D.M. Marsh, Proc. R. Soc. Lond. A, 279, 420, 1964.
[Ma83] L.I. Maissel, in L.I. Maissel (Ed.), Handbook of Thin Film, McGraw-Hill, New York, 1983.
[Ma89] D.M. Mattox, J. Vac. Sci. Technol. A, 7/3, 1105, 1989.
[Ma96] A. Matthews, in J.S. Burnell-Gray, P.K. Datta (eds.), Surface Engineering Casebook, Woodhead Publishing, Cambridge, 23, 1996.
[Ma97] A. Matthews, Protective Coatings and Thin Films, eds. Y. Pauleau, P.B. Berna, Kluwer Academic, Dordrecht, 1997.
[Mc94] A.E. McHale (Ed.), Phase Equilibria Diagrams, Borides Carbides and Nitrides, Vol. X, Amer. Ceramic Society, Westerville, OH, 1994.
[Mc96] W.D. McFall, D.R. McKenzie, R.P. Netterfield, Surf. Coat. Technol., 81,72, 1996.
[Me00] http://www.mext.go.jp/english/news/2000/04/s000406.htm, 17.4.2009.
[Me01] K.W. Mertz, H.A. Jehn, Praxishandbuch moderne Beschichtungen – Advanced Surface Coatings, Carl Hanser, München/Wien, 2001.
[Me84] R. Messier, A.P. Giri, R.A. Roy, J. Vac. Sci. Technol. A, 2, 500, 1984.
[Mi04] E.J. Mittemeijer, P. Scardi, Diffraction analysis of the microstructure of materials, Springer, Berlin/Heidelberg, 2004.
[Mi93] K. Miyoshi, J. Appl. Phys., 74, 4446, 1993.
[Mi94] C. Mitterer, Herstellung dekorativer Hartstoffschichten auf Boridbasis durch Hochleistungskathodenzerstäubung, PhD thesis, University of Leoben, 1994.
[Mi95] C. Mitterer, J. Komenda-Stallmaier, P. Losbichler, P. Schmölz, W.S.M. Werner, H. Störi, Vacuum, 46, 11, 1281, 1995.
[Mi96] C. Mitterer, H.M. Ott, J. Komenda-Stallmaier, P. Schmölz, W.S.M. Werner, H. Störi, Journal of Alloys and Compounds, 239, 2,183, 1996.

[Mi97] P.B. Mirkarimi, K.F. McCarty, D.L. Medlin, Mater. Sci. Eng. R., 21, 47, 1997.

[Mi98a] C. Mitterer, P.H. Mayrhofer, W. Waldhauser, E. Kelesoglu, P. Losbichler, Surf. Coat. Technol., 108/109, 230, 1998.

[Mi98b] T. Michler, M. Grischke, K. Bewilogua, H. Dimigen, Thin Solid Films, 322, 206, 1998.

[Mi98c] C. Mitterer, P. Losbichler, F. Hofer, P. Warbichler, P.N. Gibson, W. Gissler, Vacuum, 50, 313, 1998.

[Mi99] C. Mitterer, P.H. Mayrhofer, M. Beschliesser, P. Losbichler, P. Warbichler, F. Hofer, Surf. Coat. Technol., 120–121, 405, 1999.

[mntg] http://mnt.globalwatchonline.com/epicentric_portal/binary/com.epicentric.contentmanagement.servlet.ContentDeliveryServlet/MNT/Knowledge%2520Centre/Focus%2520Groups/MNT%2520Laser%2520Documents%2520%2526%2520Downloads/03%2520Presentations/NWLEC%2520Poster%2520-%2520Veeco%2520Wyko%2520NT1100%2520white%2520light%2520optical%2520profiling%2520system.pdf, 13.07.2009.

[Mo69] B.A. Movchan, A.V. Demchisin, Phys. Metals Metallogr., 28(4), 83, 1969.

[Mo94] J. Moser, F. Levy, F. Bussy, J. Vac. Sci. Technol. A, 12, 494, 1994.

[Mo96] T.P. Mollart, J. Haupt, R. Gilmore, W. Gissler, Surf. Coat. Technol., 86-87, 231, 1996.

[Mu00] J. Musil, Surf. Coat. Technol., 125, 322, 2000.

[Mu02] J. Musil, J. Vlček, P. Zeman, Y. Setsuhara, S. Miyake, S. Konuma, Jap. J. Appl. Phys., 41, 6529, 2002.

[Mu05] A. Mubarak, E. Hamzah, M.R.M. Toff, Jurnal Mekanikal, 20, 42, 2005.

[Mü86] W.D. Münz, J. Vac. Sci. Technol. A, 4, 2717, 1986.

[Mu98] J. Musil, J. Vlček, Mater. Chem. Phys., 54, 116, 1998.

[Mu99] J. Musil, P. Zeman, H. Hruby, P.H. Mayrhofer, Surf. Coat. Technol., 120–121, 179, 1999.

[Na96] A. Nagashima, N. Tejima, Y. Gamou, T. Kawai, C. Oshima, Surface Science, 357-358, 307, 1996.

[Ne83] C. A. Neugebauer, in L.I. Maissel (Ed.), Handbook of Thin Film, McGraw-Hill, New York, 1983.

[Oh02] M. Ohring, The Materials Science of Thin Films, Academic Press, London, 2002.

[Oo06] N. Ooi, V. Rajan, J. Gottlieb, Y. Catherine, J.B. Adams, Mat. Sci. Eng., 14, 515, 2006.

[Pa03] S. PalDey, S.C. Deevi, Mat. Sci. Eng. A, 342, 58, 2003.

[Pe03] I. Petrov, P.B Barna, L. Hultman, J.E. Greene, J. Vac. Sci. Technol. A, 21, 5, 117, 2003.

[Pe53] N.J. Petch, J. Iron Steel Inst., 174, 25, 1953.

[Pe89] I. Petrov, L. Hultman, U. Helmersson, J.E. Sundgren, J.E. Greene, Thin Solid Films, 169, 229, 1989.

[Pe92] I. Petrov, F. Adibi, J.E. Greene, W.D. Sproul, W.D. Münz, J. Vac. Sci. Technol. A, 10(5), 3238, 1992.

[Po00] D.A. Porter, K.E. Easterling, Phase transformations in metals and alloys, Stanley Thornes, Cornwall, 2000.

[Ra05] L. Rapoport, N. Fleischer, R. Tenne, J. Mater. Chem., 15, 1782, 2005.

[Ra65] E. Rabinowicz, Friction and Wear of Materials, Willey, Ney York, 1965.

[Ra95] E. Rabinowicz, Friction and Wear of Materials, 2nd edition, John Wiley, New York, 1995.

[Ra97] A.K. Ray, in R.P. Agarwala (Ed.), Surface Coatings for Advanced Materials, Trans.Tech. Publications, New Hampshire, 61, 1997.

[Re00] N.M. Renevier, N. Lobiondo, V.C. Fox, J. Witts, D.G. Teer, Surf. Coat. Technol., 123,

84, 2000.
[Re01] N.M. Renevier, J. Hampshire, V.C. Fox, J. Witts, T. Alllen, D.G. Teer, Surf. Coat. Technol., 142–144, 67, 2001.
[Re96] M. Regula, C. Ballif, J.H. Moser, F. Lévy, Thin Solid Films, 280, 67, 1996.
[Re99] G. Reisse, S. Weissmantel, Thin Solid Films, 355-356, 105, 1999.
[Ri87] K.U. Riemann, in H. Fischmeister, Hartstoffschichten zur Verschleißminderung, DGM, Oberursel, 113, 1987.
[Ro92a] B. Rother, J. Vetter, Plasmabeschichtungsverfahren und Hartstoffschichten, Deutscher Verlag für Grundstoffindustrie, Leipzig, 1992.
[Ro92b] R. Roy, Surf. Coat. Technol., 51, 203, 1992.
[Ro95a] A.E. Romanov, Nanostruct. Mater., 6, 125, 1995.
[Sa69] G.W. Samsonow, Nitridi, (Naukova Dumka, Kiev), 1969. (in Russian)
[Sa94] S. Sambasivan, W.T. Petuskey, J. Mater. Res., 9, 2362, 1994.
[Sa99] A. Savan, E. Pfluger, R. Goller, W. Gissler, Surf. Coat. Technol., 126, 159, 1999.
[Sc01] J. Schiotz, Proceeding of the 22th Riso International Symposium on Materials Science, Roskilde, Denmark, 127, 2001.
[Sc81] H. Schröcke,. K.L. Weiner, Mineralogie, Walter de Gruyter, Berlin, 1981.
[Sc96] W. Schatt, H. Worch (Eds.), Werkstoffwissenschaft, Deutscher Verlag für Grundstoffindustrie, Stuttgart, 1996.
[Sc98] J. Schiøtz , F.D. Di Tolla, K.W. Jacobsen, Nature, 391, 561, 1998.
[Scie] http://www.science.uwaterloo.ca/~kleinke/ss_jpg.html, 10.07.2009.
[Se95] M. Setoyama, A. Nakayama, T. Yoshioka, T. Nomura, A. Shibata, M. Chudou, H. Arimoto, Sumimoto Electr. Ind., 146, 91, 1995. (in Japanese)
[Se96] M. Setoyama, A. Nakayama, M. Tanaka, N. Kitagawa, T. Nomura, Surf. Coat. Technol., 86/87, 225, 1996.
[Sh49] M.C. Shaw, E.F. Macks, Analysis and Lubrication of Bearings, McGraw-Hill, New York, 1949.
[Sh92] M. Shinn, L. Hultman, S.A. Barnett, J. Mater. Res., 7, 901, 1992.
[Si92] I.L. Singer, In: I.L. Singer, H.M. Pollock, editors: Fundamentals of Friction: Macroscopic and Microscopic Processes, Dordrecht, Kluwer, 1992.
[Sm90] F.A. Smidt, Int. Mat. Reviews, 35(2), 61, 1990.
[Sm99] R.E. Smallman, R.J. Bishop, Modern Physical Metallurgy and Materials Engineering, 6th edition, Butterworth-Heinemann, Oxford, 1999.
[Sp69] T. Spalvins, ASLE Trans., 12, 36, 1969.
[Sp71] T. Spalvins, ASLE Trans., 14, 267, 1971.
[Sp80] T. Spalvins, Thin Solid Films, 73, 291, 1980.
[Sp91] W.D. Sproul, Surf. Coat. Technol., 49, 284, 1991.
[Sp96a] W.D. Sproul, Surf. Coat. Technol., 86/87, 170, 1996.
[Sp96b] W.D. Sproul, Science, 273, 889,1996.
[St00] T.A. Stolarski, Tribology in Machine Design, Butterworth-Heinemann, Oxford, 2000.
[St08] M. Stamm, Polymer Surfaces and Interfaces, Characterization, Modification and Applications, Springer, Berlin, 2008.
[St81] B.C. Stupp, Thin Solid Films, 84, 257, 1981.
[Su81] N.P. Suh, H.C. Sin, Wear, 69, 1981.
[Su85] J.E. Sundgren, Thin Solid Films, 128, 21, 1985.
[Su86] J.E. Sundgren, H.T.G. Henzel, J. Vac. Sci. Technol. A, 4, 5, 2259, 1986.
[Su95] C. Suryanarayana, Int. Mater. Rev., 40, 41, 1995.

[Su98] T. Sugino, K. Tanioka, S. Kawasaki, J. Shirafuji, Diamond Relat. Mater., 7, 632, 1998.
[Ta51] D. Tabor, The Hardness of Metals, Clarendon Press, Oxford, 1951.
[Ta89] C. Tarrio, S.E. Schnatterly, Phys. Rev. B, 11, 7852, 1989.
[Ta92] Y. Tanaka, T.M. Gür, M. Kelly, S.B. Hagstrom, T. Ikeda, K. Wakihira, H. Satoh, J. Vac. Sci. Technol. A, 10, 1749, 1992.
[Ta95] D.R. Tallant, J.R. Parmeter, M.P. Siegal, R.L. Simpson, Diamond Relat. Mater., 4, 191, 1995.
[Te01] D.G. Teer, Wear, 251, 1068, 2001.
[Th74] J.A. Thornton, J. Vac. Sci. Technol., 11, 666, 1974.
[Th75] J.A. Thornton, J. Vac. Sci. Technol., 12, 830, 1975.
[Th77] J.A. Thornton, Rev. Mater. Sci., 7, 239, 1977.
[Ul03] L. Ulrich, M. Gross, A. Lunk, Surf. Coat. Technol., 174-175, 1116, 2003.
[Ur97] M. Urgen, A.F. Cakir, Surf. Coat. Technol., 96, 236, 1997.
[Ve00a] S. Veprěk, A. Niederhofer, K. Moto, P. Nesladek, H. Männling, T. Bolom, Mater. Res. Soc. Symp. Proc., 581, 321, 2000.
[Ve00b] Veeco Metrology Group, WYKO NT1000 Setup Guide, Version 2.21, 2000.
[Ve01] S. Veprěk, A.S. Argon, Surf. Coat. Technol., 146-147, 175, 2001.
[Ve05] S. Veprěk, M.G.J. Veprěk-Heijman, P. Karvankova, J. Prochazka, Thin Solid Films, 476, 1, 2005.
[Ve75] J.A. Venables, G.L. Price in J.W. Matthews (ed.), Epitaxial Growth, Academic Press, New York, 381, 1975.
[Ve95] S. Veprěk, S. Reiprich, Thin Solid Films, 268, 64, 1995.
[Ve98] S. Veprěk, P. Nesládek, A. Niederhofer, F. Glatz, M. Jílek, M. Šíma, Surf. Coat. Technol., 108/109, 138, 1998.
[Ve99] S. Veprěk, J. Vac. Sci. Technol. A, 17, 2401, 1999.
[Vo00] A.A. Voevodin, J.S. Zabinski, Thin Solid Films 370, 223, 2000.
[Vo95] A.A. Voevodin, M.S. Donely, J.S. Zabinsky, J.E. Bultman, Surf. Coat. Technol., 77, 534, 1995.
[Vo98] A.A. Voevodin, J.S. Zabinski, Diamond Relat. Mater., 7, 463, 1998.
[Vo99] A.A. Voevodin, J.P. O'Neull, J.S. Zabinski, Surf. Coat. Technol., 116–119, 36, 1999.
[Wa04] S. Watanabe, J. Noshiro, S. Miyake, Surf. Coat. Technol., 183, 347, 2004.
[Wa95] W. Waldhauser, C. Mitterer, J. Laimer, H. Störi, Surf. Coat. Technol., 74/75, 2, 890, 1995.
[We01] G. Wei, A. Rar, J.A. Barnard, Thin Solid Films, 398-399, 460, 2001.
[We70] G.K. Wehner, G.S. Anderson, The Nature of Physical Sputtering, ed. by L.I. Maissel, R. Glang, McGraw Hill, New York, 1970.
[We97] G. Weise, N. Mattern, H. Hermann, A. Teresiak, I. Bächer, W. Brückner, H.-D. Bauer, H. Vinzelberg, G. Reiss, U. Kreissig, M. Mäder, P. Markschläger, Thin Solid Films, 298, 98, 1997.
[Wi69] J.D. Wilcock, D.S. Campbell, Thin Solid Films, 3, 3, 1969.
[Wi86] B. Window, N. Savvides, J. Vac. Sci. Technol. A, 4(3), 453, 1986.
[Wi96] B. Window, Surf. Coat. Technol., 81, 92, 1996.
[Wi97] D. Winkler, Diploma thesis, University of Leoben, 1997.
[Wi98] P. Widmayer, D. Schwertberger, M.J. Wenig, P. Ziemann, A. Bergmaier, G. Dollinger, Diamond Relat. Mater., 7, 1503, 1998.
[Wi99] T. Wittkowski, J. Jorzick, K. Jung, B. Hillebrands, Thin Solid Films, 353, 137, 1999.
[Wr77] A.W. Wright, Am. J. Sci. 13 (3rd ser.) (1) 49, 1877.

[Ye99] A.L. Yerokhin, X. Nie, A. Leyland, A. Matthews, S.J. Dowey, Surf. Coat. Technol., 122, 73, 1999.

[Yo99] Y. Yokota, S. Tagawa, T. Sugino, J. Vac. Sci. Technol. B, 17, 642, 1999.

[Za00] J.S. Zabinski, J.H. Sanders, J. Nainaparampil, S.V. Prasad, Tribol. Lett., 8, 103, 2000.

[Ze00] T. Zehnder, J. Patscheider, Surf. Coat. Technol., 133–134, 138, 2001.

[Zh02] H. Zhou, R.Z. Wang, A.P. Huang, M. Wang, H. Wang, B. Wang, H. Yan, J. Cryst. Growth, 241, 261, 2002.

8 Publications

8.1 List of included publications

I Effect of nitrogen-incorporation on structure, properties and performance of magnetron sputtered CrB_2, K.P. Budna, P.H. Mayrhofer, J. Neidhardt, É. Hegedũs, I. Kovács, L. Tóth, B. Pécz, C. Mitterer, Surface & Coatings Technology 202 (2008) 3088–3093.

II Synthesis–structure–property relations for Cr–B–N coatings sputter deposited reactively from a Cr–B target with 20 at.% B, K.P. Budna, J. Neidhardt, P.H. Mayrhofer, C. Mitterer, Vacuum 82 (2008) 771–776.

III Synthesis and characterisation of sputtered hard coatings of Cr–N/MoS_x, K. P. Budna, C. Walter, R. Spicak and C. Mitterer, Surface Engineering, 4, 5 (2008) 350-354.

IV Synthesis and characterisation of sputtered hard coatings within the system Cr-N/WS_x, K.P. Budna, C. Mitterer, submitted for publication.

8.2 Publications related to this thesis

V Transmission electron microscopy of nanocomposite Cr–B–N thin films, É. Hegedũs, I. Kovács, B. Pécz, L. Tóth, K.P. Budna, C. Mitterer, Vacuum 82 (2008) 209-213.

8.3 My contribution to the included publications

	Conception and planning*	Experiments	Analysis and interpretation	Manuscript preparation*
Publication I	80	70	40	80
Publication II	90	90	60	80
Publication III	100	90	60	80
Publication IV	100	100	100	100

*Guidance by my supervisors is not included.

Publication I

Effect of nitrogen-incorporation on structure, properties and performance of magnetron sputtered CrB_2

K.P. Budna[a], P.H. Mayrhofer[b], J. Neidhardt[c], E. Hegedũs[d], I. Kovacs[d], L. Toth[d], B. Pecz[d], C. Mitterer[b]

a. Materials Center Leoben Forschung GmbH, Franz-Josef-Strase 13, A-8700 Leoben, Austria
b. Department of Physical Metallurgy and Materials Testing, University of Leoben, Franz-Josef-Strase 18, A-8700 Leoben, Austria
c. Christian Doppler Laboratory for Advanced Hard Coatings, Department of Physical Metallurgy and Materials Testing, University of Leoben, Franz-Josef-Strase 18, A-8700 Leoben, Austria
d. MFA Research Institute for Technical Physics and Materials Science, Konkoly-Thege u. 29-33, H-1121 Budapest, Hungary

Abstract

Transition metal (TM) boron nitrides are promising candidates for protective coatings with self-lubricating abilities as they can combine properties of TM diborides with the lubricity of hexagonal boron nitride (h-BN). Here, we report on Cr-B-N coatings prepared by unbalanced DC magnetron sputtering of a CrB_2 target in argon/nitrogen atmosphere at 450°C. By varying the nitrogen partial pressure (p_{N2}) between 0 and 64 % of the total pressure ($p_{Ar} + p_{N2}$), the N-content in our coatings could be increased from 0 to 47 at.%. The results obtained from X-ray diffraction, transmission electron microscopy and X-ray photoelectron spectroscopy show that for $p_{N2} \leq 11$ % a CrB_2-based structure type develops, whereas with increasing p_{N2} the microstructure becomes then X-ray amorphous and finally CrN is detected as the sole crystalline constituent. With increasing p_{N2} from 0 to 11 %, the hardness and indentation modulus rapidly decrease from 40.6 and 397 GPa for CrB_2 to 13.4 and 108 GPa for $CrB_{2.0}N_{0.5}$. All coatings investigated yield only a moderate friction coefficients between 0.5 and 0.7. Based on detailed high-resolution TEM studies, we canconclude that the missing h-BN based lubricity is due to a lack of a significant long-range order.

Keywords: magnetron sputtering, Cr-B-N, microstructure, XRD, TEM

1. Introduction

Protective thin coatings improving the mechanical and tribological performance of tools and components are of increasing importance for industrial applications. This is based on their excellent properties like high corrosion resistance, high thermal stability and favourable friction and wear behaviour. For automotive components like piston rings, wear resistant coatings with low friction coefficients or even self-lubricating ability are desired to e.g., decrease fuel consumption [1]. Candidates for self-lubricating coatings are transition

metal boron nitrides (TM-B-N), as they could combine the properties of transition metal (TM) diborides with those of hexagonal boron nitride (h-BN). For example, TiB_2 and CrB_2 are well known for their high hardness and excellent oxidation resistance up to 900°C in ambient air [2]. h-BN on the other hand is a common solid-lubricant due to its easily activated hexagonal shear systems with possible application temperatures up to 770°C [2]. Consequently, TM-B-N type coatings are thoroughly investigated, like Zr-B-N [3,4],Ti-B-N [5-11] and Cr-B-N [12-18]. Although there is conclusive evidence that h-BN can be formed in TM-B-N thin coatings [19], their reported lack of self-lubricating properties remains largely unexplained. Thus, a detailed characterisation of chemical composition as well as bonding- and microstructure of magnetron sputtered Cr-B-N coatings is presented here and correlated to their mechanical and tribological properties, in order to provide an explanation for the missing lubricity of BN containing coatings.

2. Experimental details

Cr-B-N coatings were synthesized by unbalanced reactive magnetron sputtering of a sintered CrB_2 target (Chemco GmbH, Bad Soden-Salmunster, Germany, 99.5 % pure, ∅ 150 × 6 mm) in an Ar/N_2 atmosphere (99.999 % pure) in a laboratory-scale unbalanced DC magnetron sputtering system [19] with a base pressure < $1x10^{-3}$ Pa. Mirror-polished silicon (100) (20 x 7 x 0.45 mm^3) and AISI M2 high-speed steel disks (DIN 1.3343, ∅ 40 × 10 mm) with a hardness of 65 HRC were used as substrates. Prior to mounting on the substrate holder parallel to the target surface at a distance of 10 cm above the target (see reference [20] for more details), the substrates were ultrasonically pre-cleaned in acetone and ethanol. The target was pre-sputtered for 5 min at a current of 1.5 A in Ar atmosphere at 0.4 Pa, and the substrates were ion-etched using an Ar glow discharge with -1250 V at 2.6 Pa. During deposition, the substrate temperature as well as total gas pressure ($p_{Ar}+p_{N2}$) was kept constant at 450°C and 0.4 Pa as controlled by a calibrated thermocouple as well as a capacitive gauge, respectively, while the nitrogen partial pressure p_{N2} was varied stepwise from 0 to 64 %. The sputter power density on the target was set to ~ 4 W/cm^2 and a constant substrate bias of -50 V was applied. The 60 min deposition time results in a thickness of ~ 4.5 µm for coatings synthesized at lower p_{N2} < 32 % while the increasing target poisoning at higher p_{N2} reduces the deposition rate by almost 60 %. The composition of selected coatings as well as their chemical bonding structure was determined by X-ray photoelectron spectroscopy (XPS) performed with an Omicron Multiprobe analysis system using a monochromized Al Kα X-ray beam with a resolution of < 0.2 eV. The composition was determined after 2500 eV Ar ion sputter cleaning for 40 min using calibrated sensitivity factors for the specific elements [21]. The core level for bonding evaluation were recorded without initial sputter cleaning to avoid structural rearrangement and subsequently fitted using the Unifit Software package [22]. Microstructural investigations were performed by Bragg-Brentano X-ray diffraction (XRD, Siemens D500) using Cu Kα radiation. The so obtained patterns were simulated by

Rietveld analysis using the Topas 2.1 software package. A Philips CM20 transmission electron microscope (TEM) operated at 200 kV was used for studies of the average particle size utilizing bright- and dark-field modes. The overall crystal structure was investigated by selected area electron diffraction (SAED) patterns. On selected sample cross-sections, high-resolution transmission electron microscopy (HRTEM) was conducted with a JEOL 3010 operating at 300 kV (ideal point-to-point resolution of 0.17 nm). Some high-resolution micrographs were first Fourier-transformed using the FFT (Fast Fourier Transformation) routine included in GATAN DigitalMicrograph software package and then filtered by a ring mask, thus selecting a range of lattice spacing values. After back-transformation of the filtered FFT, these selected spacings are significantly enhanced on the processed image irrespective of their direction. The cross-sectional samples for TEM analysis were mechanically ground, polished and subsequently thinned by ion milling at 10 keV by Ar^+ ions. In order to minimize the ion beam damage, the energy was decreased to 3 keV in the final stage. Indentation modulus (E) and universal plastic hardness (H) of our coatings on steel substrates were determined from the loading and unloading segments during 25 computer-controlled micro-indentations (Fischerscope H100C). The maximum load applied to the Vickers indenter was 30 mN for the thicker coatings deposited at low N_2 partial pressures and 15 mN for those synthesized at partial pressures higher than 43 % to limit the indentation depth to a maximum of 10 % of the coating thickness. Ball-on-disk dry sliding tests in ambient atmosphere (humidity ~ 45 %) of the coated steel disks were conducted at room temperature using a CSM tribometer and sintered alumina balls (∅ = 6 mm) as counterparts. A constant velocity of 10 cm/s, a sliding distance of 300 m and a wear track radius of 5 mm were used. The resulting wear tracks were analyzed by white-light-optical profilometry (Veeco NT 1100).

3. Results and discussion

3.1. Chemical composition

Fig. 1(a) shows the coating composition in the simplified Cr-B-N triangular phase diagram, where major ternary phase fields like Cr + CrB_2 + CrN (I), B + CrB_2 + BN (II), N + BN + CrN (III), and CrN + BN+ CrB_2 (IV) are indicated, while the impurity level for O and C in the bulk is below 1 at.%. With increasing N_2 partial pressure, the coating composition changes from the single phase CrB_2 via the ternary CrN + BN + CrB_2 phase field to the quasi-binary CrN-BN tie-line at the highest partial pressure of 64 %. The reliability of the measurement, e.g., in terms of the calibrated XPS sensitivity factors is indicated by the fairly constant Cr/B ratio of 0.47 ± 0.04, see Table 1. The rapidly increasing supply of activated nitrogen (ions and radicals originating from the plasma) with increasing partial pressure leads to a sharp increase in N concentration and, thus, the formation of CrN and BN on the expense of CrB_2.

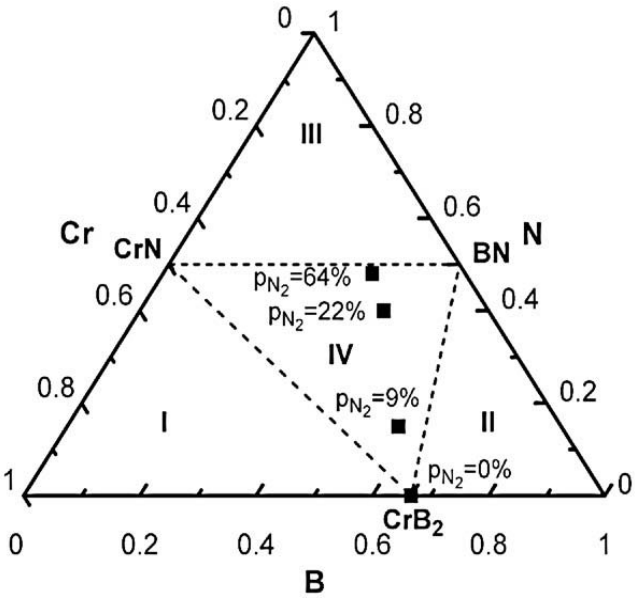

Figure 1: Chemical composition of the deposited coatings within the simplified Cr-BN triangular phase diagram (after [12]) with indicated major ternary phase fields like Cr + CrB_2 + CrN **(I)**, B + CrB_2 + BN **(II)**, N + BN + CrN **(III)**, and CrN + BN + CrB_2 **(IV)**.

Table 1: Composition of the Cr-B-N coatings for various p_{N2} determined by XPS alongside with the calculated equilibrium ratios of the main constituents (CrB_2, CrN, BN).

p_{N2} (%)	Composition (at.%)				Calculated phase composition (mol%)		
	Cr	B	N	Cr/B	CrB_2	CrN	BN
0	33.7	66.3	0	0.51	100	0	0
9	28.1	57.4	14.5	0.49	62	11.6	26.4
22	17.9	42.3	39.8	0.42	14.5	23.9	61.6
64	16.3	36.3	47.4	0.45	3.5	29.7	66.8

This is also corroborated by the much larger Gibbs free energy of -117.1 kJ/mol (CrN) and -250.5 kJ/mol (BN) of the nitrides compared to just -94.1 kJ/mol (CrB_2) for the boride [23]. Since non-equilibrium thermodynamic growth conditions are inherent to PVD thin film growth, the equilibrium phase composition purely derived from the respective elemental concentrations, as shown in Table 1, might be offset. Thus, XPS core level spectra of the respective elements were recorded to qualitatively support the presented trends by the observed chemical shift characteristic for a certain bonding environment. The spectra were recorded from as-deposited samples without any initial sputter-cleaning to avoid unintentional rearrangement of the bonding states. Fig. 2 shows the respective Cr 2p, B 1s and N 1s spectra together with the reported binding energies of the contributing main bonding configurations [24,25]. Oxygen related contributions can be detected for Cr and B at higher binding energies due to its high electro-negativity indicating surface oxidation, which do, however, not overlap with B, Cr or N related features. Besides Cr-O, Cr-B and Cr-N bonding states can be detected for the Cr 2p duplet (1/2 and 3/2) according to references for CrB_2 and CrN as well as Cr_2N [24,25] (Fig. 2a). The small difference between the two binding energies allows for an indication of a shift from a boride to a

nitride-dominated environment with increasing partial pressure. Also for B 1s (Fig. 2b) B-N and B-Cr bonding states are present. At low partial pressures only one peak at ~ 188 eV could be detected, which corresponds fairly well to CrB_2 at 187.5 eV [24]. With increasing N_2 fraction, the B-N related contribution emerges at 190.5 eV (BN ~ 191 eV [24]) indicating the already mentioned formation of BN. By additional investigations of the N 1s core levels (Fig. 2c), a corresponding tendency can be found. With increasing N content in the Cr-B-N coatings, a broad feature at ~ 397.6 eV emerges with an increasing shoulder towards lower binding energies, due to the overlap of N-Cr and N-B contributions at approximately 396.7 and 398.1 eV [15], respectively. In summary, without N_2 in the discharge exclusively Cr-B bonds are present, while at increasing p_{N2}, contributions from Cr-N as well as B-N emerge until no Cr-B bonds can be detected any more by XPS for the highest p_{N2} of 64 %. This corroborates the already presented notion (Table 1) that the boride dominated structure fully transforms into the CrN + BN dual phase, as already suggested by the stoichiometry and the phase diagram.

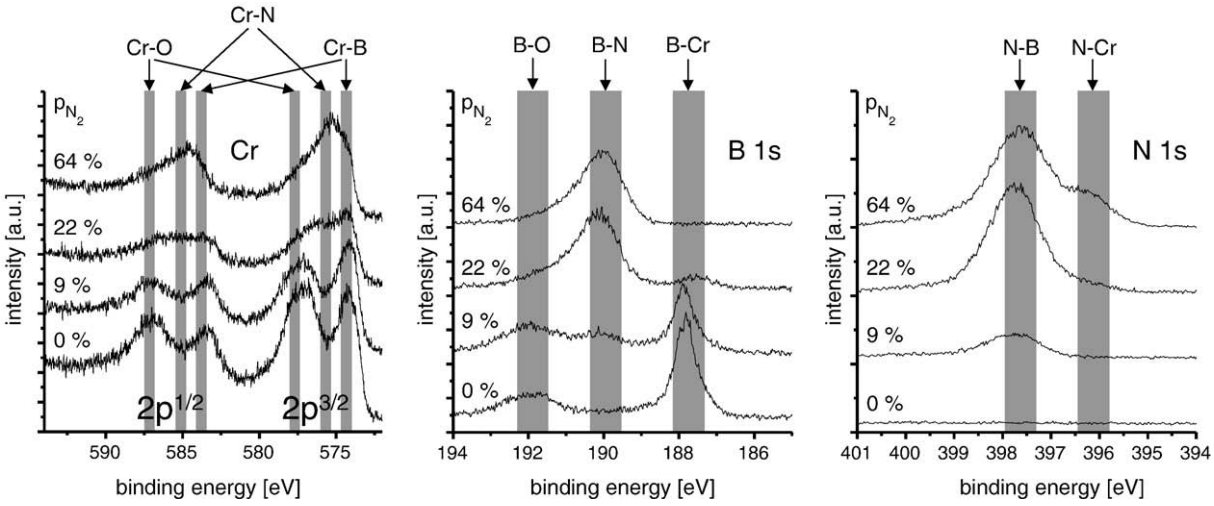

Figure 2: XPS Cr 2p, B 1s and N 1s core level spectra of Cr-B-N-coatings synthesized at various p_{N2} fractions. The grey regions indicate binding energies of the respective reference compounds [21,22].

3.2. Structure and morphology

X-ray diffractograms of the Cr-B-N coatings on Si substrates, with their (200) reflection at 32.9° 2θ, are presented in Fig. 3 as a function of p_{N2}. The standard 2θ positions for cubic CrN (JCPDS #11-0065) and hexagonal CrB_2 (JCPDS #34-0369) are added. For the coating deposited without nitrogen, only the rather narrow reflections at 29.8 and 61.3° 2θ attributable to (001) and (002) CrB_2 can be detected suggesting a strongly textured film growth as reported also for TiB_2 in Ref. [26] with a rather large domain size. With increasing N-content, the CrB_2 reflections decrease in intensity and broaden. The additional (100) and (101) reflections for CrB_2 at 34.9 and 46.5° 2θ for the coatings prepared with p_{N2} = 9 and 11 %, respectively, indicate that the preferred growth orientation of CrB_2 is suppressed and the crystallinity deteriorates substantially. For the Cr-B-N

coatings, deposited between 17 and 33 % p_{N2}, an X-ray amorphous structure evolves showing a broad low intensity coating reflection ranging from 37 – 58° 2θ. For coatings prepared at p_{N2} > 43 %, reflections attributed to CrN (111), (200), and (220) can be detected. Consequently, the evolution of crystalline phases of the Cr-B-N coatings can be subdivided into CrB_2 dominated (for $p_{N2} \leq 11$ %), X-ray amorphous (for p_{N2} between 17 – 43 %), and CrN dominated (for p_{N2} > 43 %).

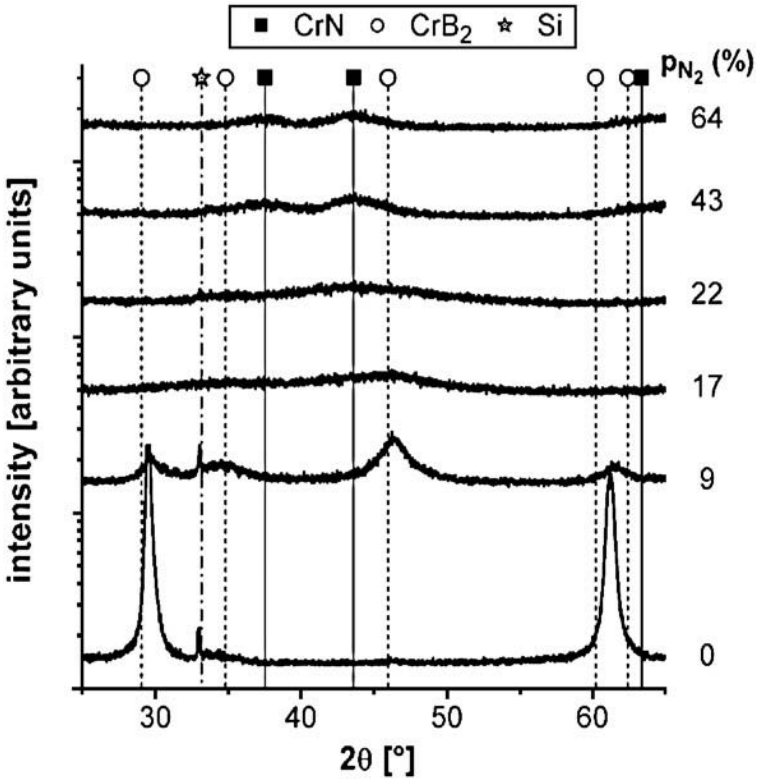

Figure 3: XRD patterns of Cr-B-N coatings on Si(100) substrates with increasing p_{N2}.

Quantitative Rietveld analysis conducted for representative Cr-B-N coatings, deposited at p_{N2} = 9 or 64 %, respectively, yield an average domain size of 2-5 nm. TEM dark-field images of CrB_2 and three representative Cr-B-N (p_{N2} = 9, 22, 64 %) coatings are displayed in Figs. 4(a), (b), (c) and (d), respectively. The small inserts show the corresponding SAED patterns and indicate a good agreement to the conducted XRD investigations. The CrB_2 coating (Fig. 4a) exhibits a columnar growth with diameters of ~ 10 nm comparable to Ref. [27,28]. The SAED pattern indicates the hexagonal CrB_2 phase and due to the strong texture an almost single-crystalline pattern. For the Cr-B-N coatings, the dark-field images show a pronounced reduction of the crystallite size and suppression of the columnar growth with increasing p_{N2}. Hexagonal CrB_2 can still be found for the coating prepared at p_{N2} = 9 %. The broad SAED rings as well as the featureless micrograph at p_{N2} = 22 % corroborate the amorphous nature of the coatings synthesized at intermediate N_2 fractions. For the coating deposited at p_{N2} = 64 % (Fig. 4d), the CrN structure evolves which is consistent with the SAED pattern. For all coatings investigated, no laminar structures or small crystals of h-BN could be identified.

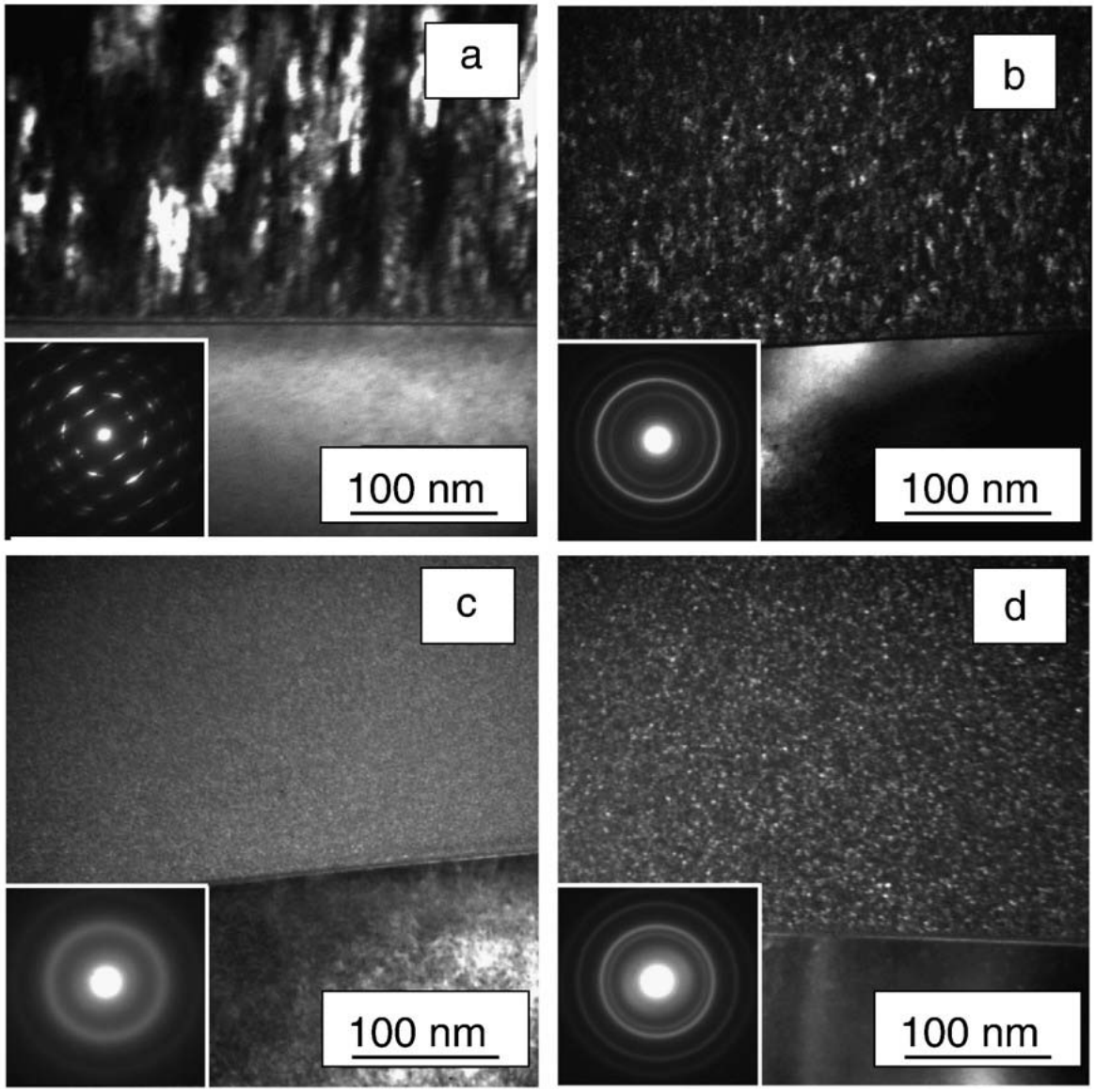

Figure 4: Cross-sectional dark-field TEM micrographs of Cr-B-N coatings deposited at **(a)** p_{N2} = 0 %, **(b)** 9 %, **(c)** 22 %, and **(d)** 64 %, alongside with their respective SAED patterns taken near the interface.

Based on the TEM investigations, we can conclude that with increasing p_{N2} the coating structure changed from columnar to equiaxed. For p_{N2} between 17 and 43 %, an amorphous structure can be found, and for p_{N2} > 43 %, the structure is dominated by CrN, in agreement to the XRD studies, as well as amorphous fractions – most likely BN, as indicated by XPS. A detailed report on the respective TEM investigations can be found in [29].

3.3. Mechanical and tribological properties

The indentation modulus (E) and hardness (H) of the Cr-B-N coatings are presented in Fig. 5 as a function of p_{N2}. A maximum in hardness and modulus of 40.6 and 397 GPa, respectively, is obtained for the CrB_2 coating. Very high hardness values for borides are

reported due to their nanocolumnar structure and the strong covalent bonds within the B network, see, e.g., Ref. [26] for TiB_2 as well as Ref. [28] for CrB_2. With increasing nitrogen content, hardness and modulus of the Cr-B-N coatings rapidly decrease via intermediate values of 26 and 300 GPa at p_{N2} = 9 % down to 14 and 120 GPa for p_{N2} > 30 %. This drop in mechanical properties coincides with the preferred formation of a large fraction of amorphous BN phase as indicated by XPS (see Table 1) and TEM, presumably with less advantageous mechanical properties.

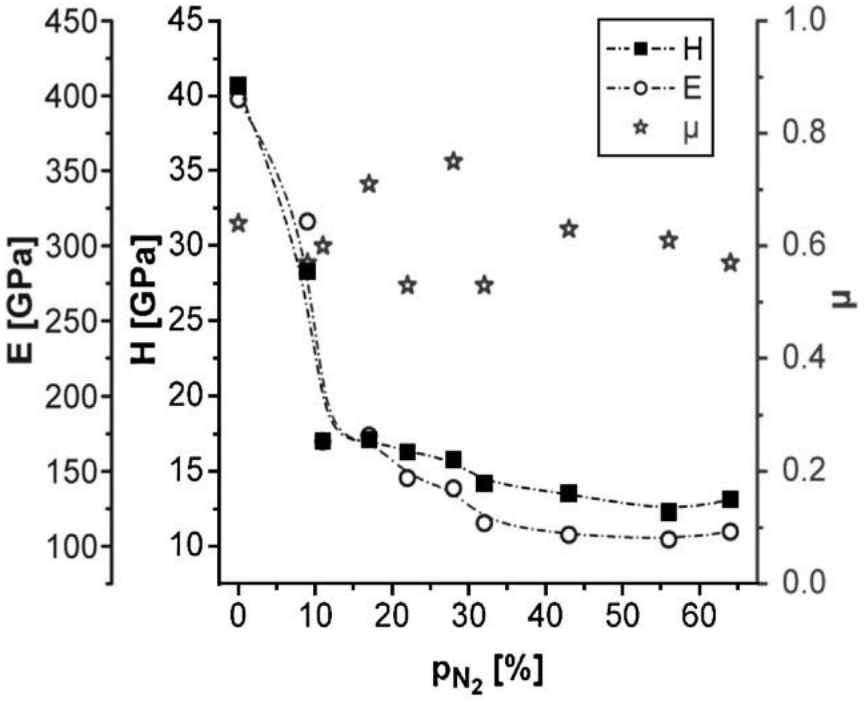

Figure 5: Hardness and elastic modulus, obtained by micro-indentation, as well as friction coefficients obtained for Cr-B-N coatings as a function of p_{N2}. The total error for H and E as obtained from the standard deviation of the indentation data is app. ± 5 %.

For a lower N_2 fraction of 9 %, ~ 26 mol% amorphous BN is assumed to be formed surrounding the small equiaxed CrB_2 crystallites resulting in intermediate hardness values. With increasing p_{N2}, the BN fraction saturates rapidly at values ≥ 60 mol% giving rise to a further deterioration of the mechanical properties. Hereby, the coating structure changes from completely amorphous (p_{N2} ~ 22 %) to an almost quasi-binary structure built of nanocrystalline CrN embedded in an amorphous BN matrix. The low mass density of BN hereby results in an even higher volume fraction of rather soft amorphous BN, which does not provide a significant resistance to plastic deformation. Surprisingly, the tribological investigation of Cr-B-N coatings shows only minor differences of their friction coefficients (μ), which are rather constant at ~ 0.6 ± 0.15 (see Fig. 5) regardless the amount of BN phase fraction. Even for coatings which contain dominantly BN (obtained by XPS, see Table 1), no low-friction effect could be observed. These results suggest that the formed BN phase lacks morphology and/or structure which could support shearing and, hence, lower the friction coefficient.

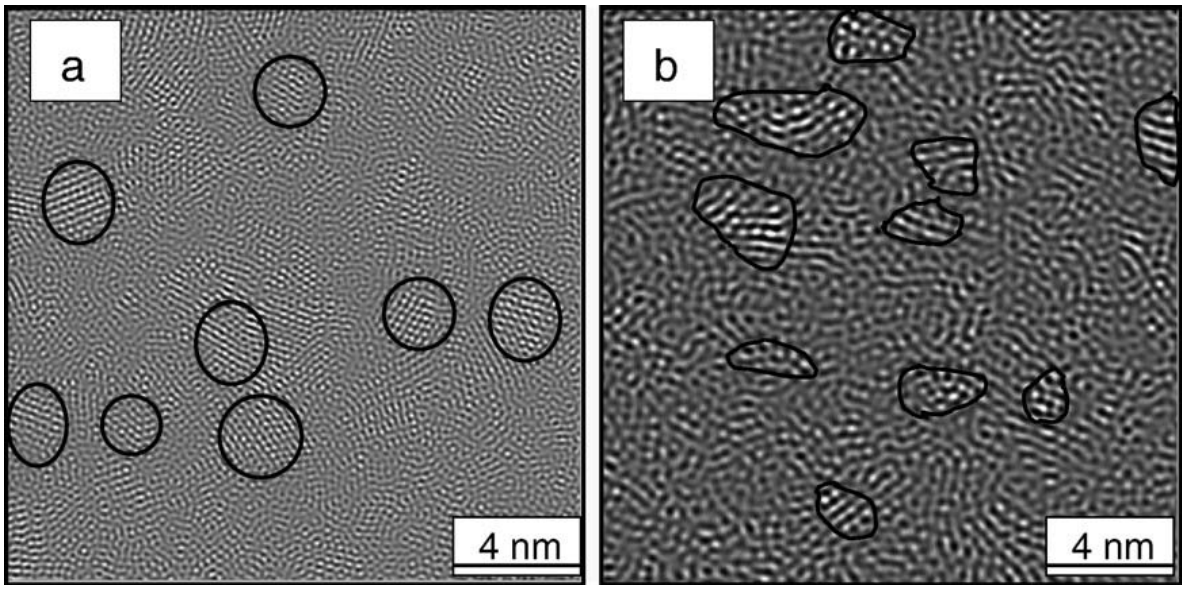

Figure 6: Digitally processed HRTEM images showing the same area of a crosssectional specimen for a Cr-B-N coating deposited at p_{N2} = 64 %. Fourierfiltered images using a ring mask enhancing **(a)** CrN (d= 0.20-0.26 nm) and **(b)** BN (d= 0.28-0.36 nm) spacings. The black lines are guides to the eye helping to identify coherent particles of the phases.

To illuminate this, the high N-containing coating (N ~ 47 at.%, p_{N2} = 64 %), which shows the highest amount of BN phase (~ 67 mol%), was investigated by HRTEM. Figs. 6(a) and (b) show Fourier-transformed cross-sectional HRTEM images utilizing the CrN and BN lattice spacing, respectively (see Ref. [29] for details). The morphology of this coating can be described as nanocomposite, where small grains (2-5 nm) of cubic CrN (Fig. 6a) are embedded in a large fraction of predominantly amorphous BN matrix (Fig. 6b). Within the amorphous BN matrix, a hexagonal lattice can only be identified for a few atomic layers, which have, furthermore, no preferential orientation [29]. Consequently, these sub-5-nm crystalline h-BN domains do not support shearing in a macroscopic tribological contact due to their small lateral extension and random orientation.

4. Conclusions

Cr-B-N coatings were synthesised by reactive unbalanced magnetron sputtering using a CrB_2 target in an argon/nitrogen atmosphere. By increasing the nitrogen partial pressure p_{N2} from 0 to 64 % of the total pressure ($p_{Ar} + p_{N2}$), the N content within the coatings could be increased to ~ 47 at.%, since Cr and B nitrides are thermodynamically favourable over CrB_2. Thus, the coating composition changes from the single CrB_2 phase via the ternary CrN–BN–CrB_2 phase field to a binary CrN–BN phase mixture. Owing to the large amount of B, predominantly amorphous BN is formed as soon as nitrogen is present in the discharge, which saturates at a phase fraction ≥ 62 mol% for $p_{N2} \geq 22$ %. As to the crystalline constituents, the CrB_2 coating, prepared with p_{N2} = 0 %, exhibits a columnar growth with (001) preferred orientation and hardness and indentation modulus of 40.6 and

397 GPa, respectively. With increasing N content, the columnar structure is suppressed by re-nucleation processes and for p_{N2} between 17 and 43 % an amorphous structure evolves. For p_{N2} > 43 %, crystalline CrN with diameters of 2 – 5 nm can be detected by X-ray diffraction, selected area electron diffraction, and transmission electron microscopy. Due to the increasing volume fraction of amorphous BN in the Cr-B-N coatings, their hardness and indentation modulus rapidly decreases with increasing N content to values below 17.1 and 174 GPa for $p_{N2} \geq 17$ %. Although a large amount of BN is present in the Cr-B-N coatings prepared at $p_{N2} \geq 22$ %, no solid-lubricant low-friction effect could be observed. All coatings show a friction coefficient of ~ 0.6 ± 0.15, independent of their chemical composition and microstructure. Fourier-transformed high-resolution transmission electron microscopy studies showed that the formed BN phase is highly distorted with no preferred orientation and hexagonal domains extending only over a few atomic layers. Consequently, this BN phase is not able to develop a low-friction effect by easy shearing during tribological contacts.

Acknowledgments

This work was financially supported by the European Union within the NAPILIS Specific Targeted Research Project (contract NMP3 CT 2003 505622). The authors are grateful for the XPS investigations performed by A. Fian (Joanneum Research, Weiz, Austria). J.N. acknowledges financial support by the Christian Doppler Society and the companies Plansee GmbH, Lechbruck, Germany, and Oerlikon Balzers AG, Balzers, Liechtenstein.

References

[1] I. Kvernes, P. Fartum, Thin Solid Films 53 (1978) 259.
[2] R. J. Brotherton, H. Steinberg, Progress in Boron Chemistry, Vol.2, Pergamon Press, Oxford, 1970, p. 173 – 230.
[3] C. Mitterer, A. Ubleis, R. Ebner, Mater. Sci. Eng. A 140 (1991) 670.
[4] E. Brandstetter, C. Mitterer, R. Ebner, Thin Solid Films 210 (1991) 123.
[5] C. Mitterer, P. Rodhammer, H. Stori, F. Jeglitsch, J. Vac Sci. Technol. A 7 (1989) 2646.
[6] C. Mitterer, M. Rauter, P. Rodhammer, Surf. Coat. Technol. 42 (1990) 351.
[7] B. Matthes, E. Broszeit, K. H. Kloos, Surf. Coat. Technol. 43-44 (1990) 721.
[8] L. S. Wen, X. Z. Chen, Q. Q. Yang, Y. Q. Zheng, Y. Z. Chuang, Surf. Eng. 6 (1990) 41.
[9] O. Knotek, F. Jungblut, K. Breidenbach, Vacuum 41 (1990) 2184.
[10] W. Gissler, Surf. Coat. Technol. 68-69 (1994) 556.
[11] P. H. Mayrhofer, C. Mitterer, J. G. Wen, I. Petrov, J. E. Greene, J. Appl. Phys. 100 (2006) 044301.
[12] P. Rogl, J. C. Schuster, Phase Diagrams of Ternary Boron Nitride and Silicon Nitride Systems, ASM, Materials Park, OH, 1992, p. 20 – 25.
[13] B. Rother, H. Kappl, Surf. Coat. Technol. 73 (1995) 14.
[14] B. Rother, H. Kappl, Surf. Coat. Technol. 96 (1997) 163.
[15] S. M. Aouadi, F. Namavar, E. Tobin, N. Finnegan, R. T. Haasch, R. Nilchiani, J. A. Turner, S. L. Rohde, J. Appl. Phys. 91 (2002) 1040.
[16] T. Z. Gorishnyy, D. Mihut, S. L. Rohde, S. M. Aouadi, Thin Solid Films 445 (2003) 96.

[17] Y. Sakamaoto, M. Nose, T. Mae, E. Honbo, M. Zhou, K. Nogi, Surf. Coat. Technol. 174-175 (2003) 444.
[18] M. Zhou, M. Nose, K. Nogi, Surf. Coat. Technol. 183 (2004) 45.
[19] T.P. Mollart, M. Baker, J. Haupt, A. Steiner, P. Hammer and W. Gissler, Surf. Coat. Technol. 74 (1995) 491.
[20] P. Losbichler, C. Mitterer, P. N. Gibson, W. Gissler, F. Hofer, P. Warbichler, Surf. Coat. Technol. 94/95 (1997) 297.
[21] J. H. Scofield, J. Electron. Spectrosc. Rel. Phenom. 8 (1976) 129.
[22] http://www.uni-leipzig.de/~unifit/ (accessed May 2007).
[23] HSC 5.11, 2004 HSC Chemistry 5.11, 2004 Outokumpu Research Oy, Pori, Finland.
[24] NIST X-ray Photoelectron Spectroscopy Database, http://srdata.nist.gov/xps/
[25] C. D Wagner, Handbook of XPS, Physical Electronics Inc., Minnesota, 1995.
[26] P. H. Mayrhofer, C. Mitterer, J. G. Wen, J. E. Greene, I. Petrov, Appl. Phys. Lett. 86 (2005) 131909.
[27] A. Audronis, P. J. Kelly, A. Leyland, A. Matthews, Thin Solid Films 515 (2006) 1511.
[28] A. Audronis, P. J. Kelly, A. Leyland, A. Matthews, Surf. Coat. Technol 201 (2006) 3970.
[29] E. Hegedős, I. Kovacs, B. Pecz, L. Toth, K.P. Budna, C. Mitterer, Vacuum 82 (2008) 209.

Publication II

Synthesis-structure-property relations for Cr-B-N coatings sputter deposited reactively from a Cr-B target with 20 at.% B

K.P. Budna[a], J. Neidhardt[b], P.H. Mayrhofer[c], C. Mitterer[c]

a. Materials Center Leoben Forschung GmbH, Franz-Josef-Straße 13, A-8700 Leoben, Austria
b. Christian Doppler Laboratory for Advanced Hard Coatings, Department of Physical Metallurgy and Materials Testing, University of Leoben, Franz-Josef-Straße 18, A-8700 Leoben, Austria
c. Department of Physical Metallurgy and Materials Testing, University of Leoben, Franz-Josef-Straße 18, A-8700 Leoben, Austria

Abstract

Cr-B-N films were synthesized by unbalanced magnetron sputtering from a sintered Cr-B target with 20 at.% B in an Ar-N_2 discharge at varying N_2 partial pressures (p_{N_2}) of up to 64 % of the total pressure ($p_{Ar} + p_{N_2} = 0.4$ Pa). Coating composition and microstructure were investigated by X-ray diffraction, X-ray photoelectron spectroscopy and wavelength-dispersive electron-probe microanalysis and correlated with mechanical and tribological properties measured by microindentation and dry-sliding ball-on-disk tests. For low nitrogen partial pressures ($p_{N_2} \leq 22$ %), the XRD patterns are composed of broad overlapping peaks with low intensity. These films have hardness values of ~ 15 GPa and indentation moduli of ~ 150 GPa. Increasing p_{N_2} from 22 % to 28 % results in an increase of the N content from ~ 38 to 50 at.% where the films meet the quasi-binary CrN-BN composition. Thereby, an increase of the hardness from ~ 15 to 32 GPa is obtained. A further increase in p_{N_2} up to 64 % results in minor changes of the chemical composition, micro- and bonding structure as well as mechanical properties. While in ball-on-disk testing early failure was observed for coatings grown at $p_{N_2} \leq 22$ %, higher nitrogen contents in the discharge yielded friction coefficients of ~ 0.43 independent of chemical composition, microstructure and mechanical properties.

Keywords: Cr-B-N, coatings, sputtering, tribological properties

1. Introduction

Over the last decades, protective coatings became increasingly important for industrial applications [1] and as such are widely used to prolong the lifetime of tools and components owing to their good corrosion resistance, high temperature stability as well as beneficial tribological properties. Especially for automotive applications, the combination of high wear resistance with low friction coefficient alongside with self-lubrication is

desired to increase lifetime, performance and efficiency [2,3]. Promising candidates for self-lubricating hard coatings are, among others, transition metal boron nitrides TMe-B-N. TMeN and $TMeB_2$ coatings are well known for their high hardness and excellent oxidation resistance, while hexagonal boron nitride (h-BN) is a common solid lubricant with a thermal stability of up to 770°C [4]. Several TMe-B-N type coatings are in the focus of interest for low-friction applications like Zr-B-N [5,6], Ti-B-N [7-11] and Cr-B-N [13-18]. After thermodynamic studies [12], first results on Cr-B-N were published in 1995 and 1997 by Rother and Kappl [13,14]. Further investigations followed whereas different target materials and deposition techniques were used [15-18]. Therefore, a comparison of the individual coatings with respect to their chemical composition, microstructure, mechanical and tribological properties is ambiguous.

In a congruent study [19], it has been shown that as soon as N is introduced, TMeN are thermodynamically favoured over TMe_xB_y phases with a saturation at the TMeN-BN tie line. The formed BN phase is at best nano-crystalline [20] and leads to a rapid deterioration of the mechanical properties of the coating. Thus, for this study the BN phase fraction is reduced by using a compound Cr-B target with 20 at.% B in order to retain the mechanical integrity of the resulting coating. The N-content in the Cr-B-N coatings was adjusted by varying the N_2 partial pressure (p_{N_2}) between 0 % and 64 % in the Ar-N_2 magnetron discharge. The resulting chemical composition, micro- and bonding structure, mechanical and tribological properties are investigated by means of X-ray diffraction (XRD), X-ray photoelectron spectroscopy (XPS), wavelength dispersive electron-probe microanalysis (EPMA), microindentation and dry sliding ball-on-disk tests.

2. Experimental details

Cr-B-N thin films were grown for 60 min by reactive magnetron sputtering from a powder metallurgically prepared Cr-B target (20 at.% B, ∅ 152.4 mm, Plansee GmbH, Lechbruck, Germany) in an Ar-N_2 atmosphere ($p_{Ar} + p_{N_2} = 0.4$ Pa) using a bias voltage of ~ -50 V, a substrate temperature of 450°C, and nitrogen partial pressures (p_{N_2}) from 0 % to 64 % of the total pressure in a laboratory-scale unbalanced dc magnetron sputtering system with a base pressure < $1x10^{-3}$ Pa (more details can be found in Refs. [21,22]). Silicon (100) (both sides mirror polished, 20 x 7 x 0.525 mm^3) and AISI M2 high-speed steel disks (∅ 40mm, polished, annealed and quenched to 65 HRC) were used as substrate materials for structural investigations and dry sliding ball-on-disk tests, respectively, and ultrasonically cleaned in an acetone/ethanol solution prior to deposition. After fixing the substrates on the sample holder parallel to the target surface at a distance of 10 cm, the target was pre-sputtered for 5 min at a current of 1.5 A in Ar atmosphere at 0.4 Pa, and the substrates were ion-etched using an Ar glow discharge with -1250 V and 2.6 Pa.

Coating morphology was studied on fractured cross-sections of coatings on Si substrates investigated by scanning electron microscopy (SEM) using a Zeiss EVO-50. To analyse the chemical composition and bonding structure, wavelength-dispersive EPMA and XPS

were performed with a MICROSPEC WDX-3PC and an Omicron Multiprobe analysis system, respectively. The latter was equipped with a monochromized Al Kα X-ray source providing for an energy resolution of ~ 0.2 eV. The microstructure and phase composition was assessed by XRD using a Siemens D500 in Bragg-Brentano mode with Cu Kα radiation. Coating hardness (H) and elastic modulus (E) were determined for all coatings deposited on silicon substrates from the unloading curves employing a computer-controlled microhardness tester (Fischerscope H100C equipped with a Vickers diamond indenter) which was calibrated following the built-in procedures on fused silica. The maximum load was varied between 20 and 50 mN to achieve an indentation depth of about 10 % of the coating thickness to minimize substrate interference. The tribology of the coatings was assessed on high-speed steel samples by dry sliding ball-on-disk tests at room temperature (30 – 45 % relative humidity) using a CSM tribometer equipped with alumina counterparts (∅ 6 mm). A load of 2 N, a sliding speed of 0.1 m/s, and a radius of the wear track of 5 mm were used in all experiments. After a sliding distance of 300 m, the obtained wear tracks were investigated by a Wyko NT 1000 3D white light profiling system.

3. Results and discussion

All coatings are well adherent and exhibit a silver grey lustre. The constant deposition time of 60 min resulted in a coating thickness of ~ 3 µm ($p_{N_2} \leq 28$ %) down to ~ 1 µm ($p_{N_2} > 28$ %) attributed to the target poisoning related drop in deposition rate from ~ 70 to ~ 30 nm/min going from lower to higher p_{N_2}. SEM fracture cross-sections of our Cr-B-N films reveal a featureless glassy to very fine-grained structure with a smooth surface for all the investigated N_2 partial pressures (Figs. 1a - c).

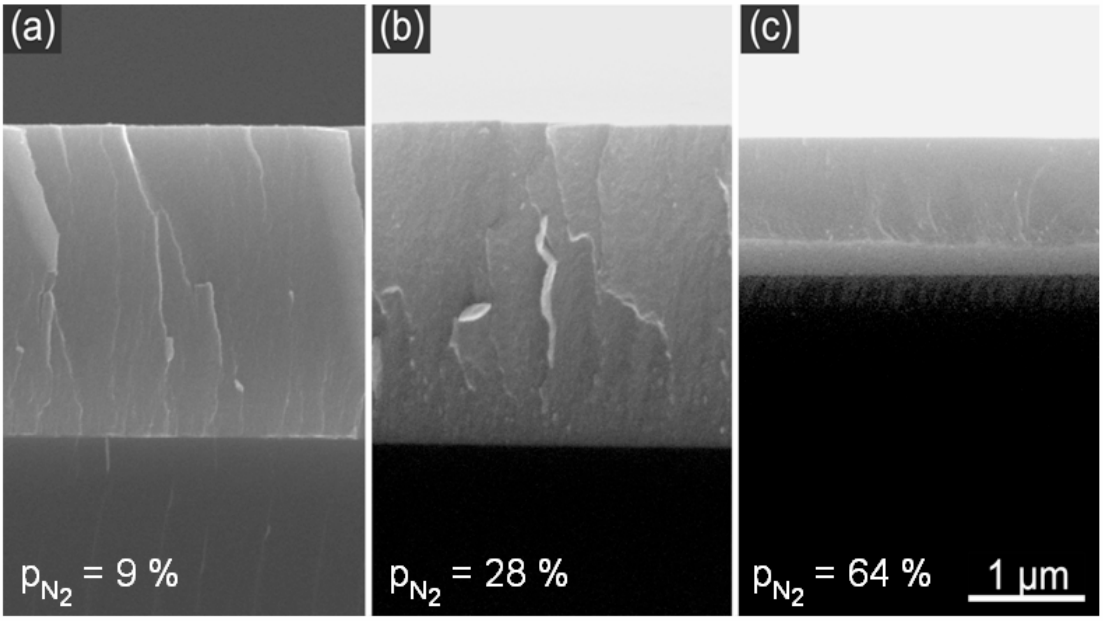

Figure 1: SEM fracture cross-sections of Cr-B-N films deposited at **(a)** p_{N2} = 9 %, **(b)** 28 % and **(c)** 64 %.

3.1. Chemical composition

The composition of the samples, determined with EPMA, is shown in the ternary Cr-B-N phase diagram (Fig. 2) and listed in Table 1. The sum of C and O impurities within the coatings was below 3 at.%. The coating deposited in Ar atmosphere (p_{N_2} = 0 %) exhibits a composition closely corresponding to the target material, whereas the additional ~ 2 at.% N might originate from post-deposition surface contamination or residual gases during deposition. With increasing p_{N_2}, the N content increases rapidly and saturates at ~ 50 at.% for $p_{N_2} \geq 28$ %. It is unclear if the increase in Cr/B ratio from 4.5 to 7.3 can be attributed to a measurement artefact due to the drastically different EPMA information depth of Cr and B making the analysis extremely sensitive towards surface contamination [23] or if actually less B is incorporated at higher N_2 fractions due to, e.g., gas phase scattering.

Table 1: Chemical composition of our Cr-B-N films analysed with EPMA alongside with the respective Cr/B as well as (Cr+B)/N ratio.

pN2 (%)	composition (at.%)			Cr/B	(Cr+B)/N
	Cr	B	N		
0	79.7	17.9	2.5	4.5	39.0
11	63.7	18	18.3	3.5	4.5
22	52.9	8.9	38.2	5.9	1.6
28	43.5	6.6	49.9	6.6	1.0
64	41.7	5.7	52.7	7.3	0.9

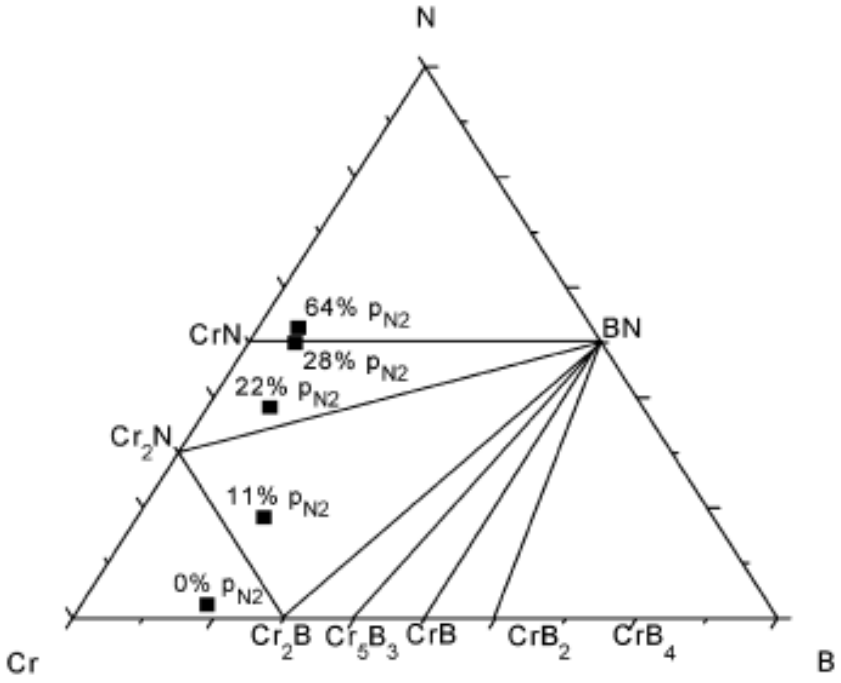

Figure 2: Classification of the chemical composition as determined by EPMA within the ternary phase diagram of Cr-B-N [12].

Fig. 2 illustrates the multitude of Cr-borides, which makes predictions regarding the phase composition especially for lower N-contents ambiguous. Furthermore, non-equilibrium thermodynamic growth conditions are inherent to plasma-assisted thin film growth. Thus, the phase composition purely derived from the equilibrium phase diagrams can only serve as a rough guide. However, the enthalpy of formation favours with -250 kJ/mol the BN formation over Cr_xB_y (e.g. -94 kJ/mol for CrB_2) [24]. Thus, higher N-containing films are dominated by Cr and B nitrides. As such the coating deposited at p_{N_2} = 22 % is within the ternary Cr_2N-CrN-BN phase field with the corresponding fractions of 61, 15, and 24 mol%, respectively (see Fig. 2 and Table 1). As soon as the nitrogen concentration saturates for $p_{N_2} \geq 28$ % (Table 1), Cr_2N transforms to CrN resulting in a dual-phase structure of ~ 87 mol% CrN alongside with ~ 13 mol% BN (Fig 2).

3.2. Chemical bonding

In order to draw conclusions about the near-surface bonding structure and, thus, the actual phase composition, XPS was conducted on five selected films (p_{N_2} = 0 %, 9 %, 22 %, 28 %, and 64 %). Instead of the common sputter cleaning procedure, only a gentle heat treatment at 350°C for 30 min was applied to remove volatile surface contaminations without disturbing the actual bonding structure by, e.g., ion-bombardment inflicted structural rearrangement or preferential sputtering. Figs. 3a-c shows the relevant core level spectra of Cr $2p^{1/2}$ and $2p^{3/2}$, N 1s, and B 1s, respectively. The positions of relevant binding energies of B, N and Cr as well as O related states are indicated [25,26]. Due to the gentle cleaning procedure, surface contamination related contributions, namely Cr-O and B-O, are still detected, especially for the more reactive Cr- and B-rich films deposited at lower N_2 fractions. However, their position at higher binding energies does not interference with bulk bonding states.

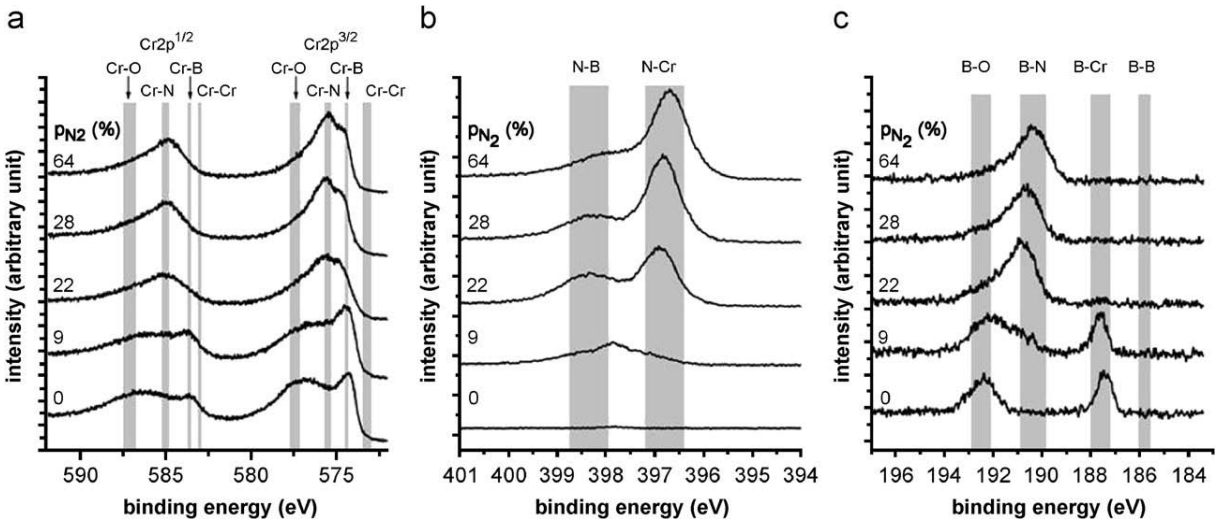

Figure 3: (a) XPS core level spectra of Cr 2p, **(b)** N 1s and **(c)** B 1s for the Cr-B-N films synthesized at different p_{N2}. The corresponding binding energies of reference materials are also indicated [25,26].

With increasing p_{N_2}, the Cr-B states at ~ 574 and ~ 584 eV for Cr $2p^{1/2}$ and $2p^{3/2}$ as well as the B-Cr state at ~ 187.5 eV for B 1s decrease in intensity. Congruently, the Cr-N (576 + 585 eV) and N-Cr (396.7 eV) states in Cr 2p and N 1s, respectively, as well as the B-N related bonding state at 190.5 eV in the B 1s spectra emerge. This corroborates the already mentioned notion that with increasing availability of activated nitrogen (radicals and ions originating from the discharge) BN and CrN phases are preferentially formed on the expense of Cr_xB_y.

3.3. Microstructure

The crystallinity of the coatings was investigated by XRD and the corresponding diffractograms are shown in Fig 4.

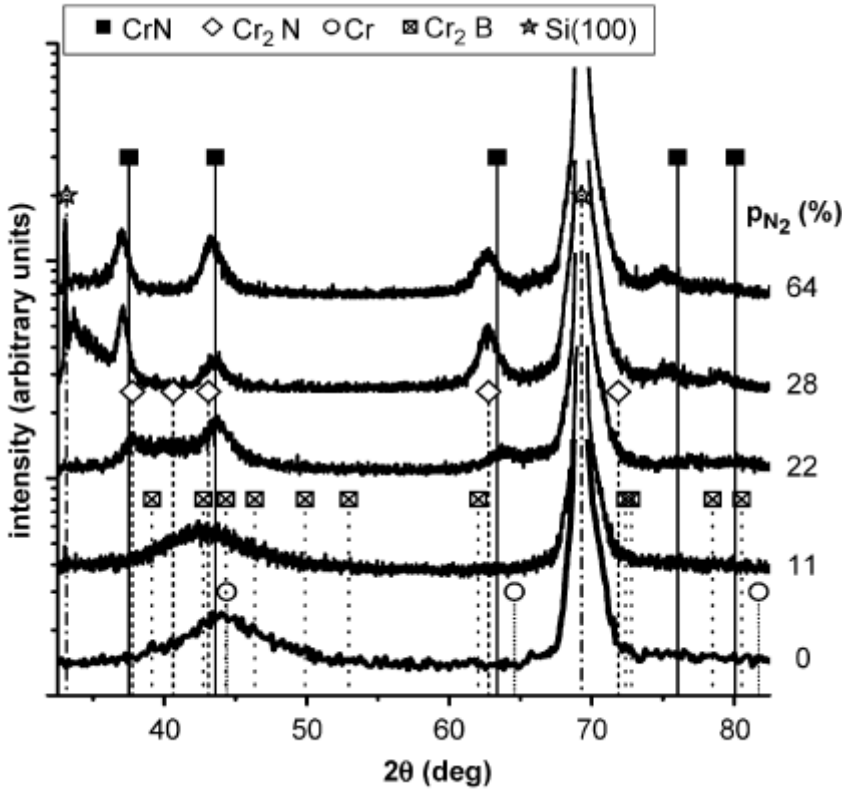

Figure 4: XRD patterns of Cr-B-N coatings on Si (100) substrates with increasing p_{N2}.

For $p_{N_2} \leq 11$ %, an X-ray amorphous or at best nano-crystalline structure is present, with a broad reflection at ~ 44°. A more detailed assignment is not practical due to the various potential phases having peaks in this range. The stoichiometry, however, suggests that beside Cr_xB_y and Cr_xN also metallic Cr contributes significantly to the pattern. At p_{N_2} = 22 %, a combination of Cr_2N and CrN reflexes can be detected. This is in good agreement with our XPS and EPMA results indicating a phase composition within the ternary CrN (15 mol%) + Cr_2N (61 mol%) + BN (24 mol%) phase field, compare to Fig. 2. Congruently, only CrN peaks are obtained as soon as the nitrogen concentration saturates for $p_{N_2} \geq 28$

%, corresponding to XPS and EPMA results corroborating a CrN-BN dual-phase structure (see Fig. 2). Quantitative Rietveld analysis yielded an average CrN crystallite size of less than 6 nm for the dual-phase coatings. However, no evidence for crystalline BN was found in the investigated films for p_{N_2} ranging from 0 % to 64 %. Thus, the dual-phase structure can be envisioned by CrN nano-crystals embedded in ~ 13 mol% amorphous BN.

3.4. Mechanical and tribological properties

The correlation of microstructure with mechanical properties is presented over the range of investigated N_2 partial pressures via H and E in Fig. 5.

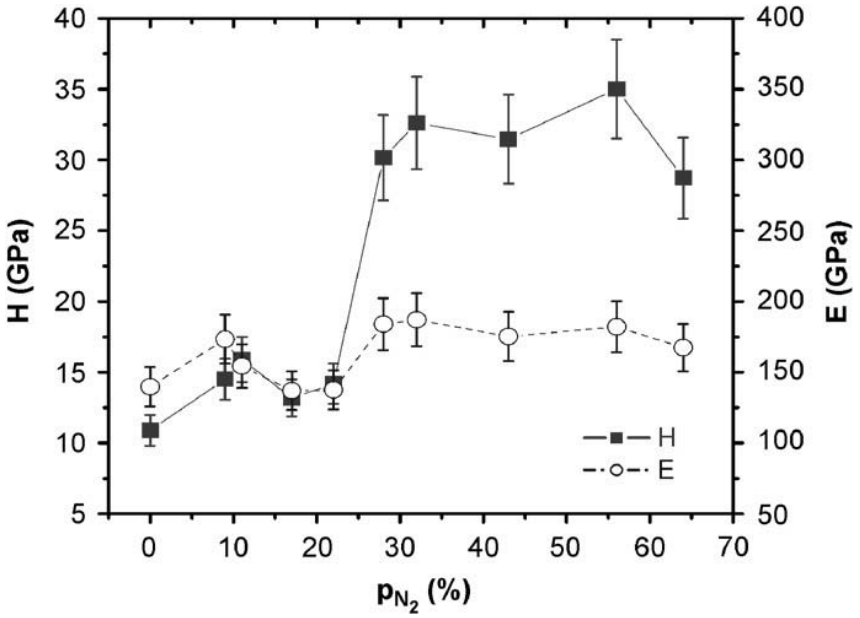

Figure 5: Microhardness (H) and elastic modulus (E) of our Cr-B-N films as a function of p_{N2}.

Not surprisingly, the lowest hardness and modulus values of ~ 15 and ~ 150 GPa, respectively, are obtained for the amorphous to nano-crystalline low N-containing films synthesized at $p_{N_2} \leq 18$ %, presumably due to its least partially metallic character. However, these low values are still retained for the partially crystalline film within the Cr_2N-CrN-BN phase field at $p_{N_2} = 22$ %, most probably due to the large fraction of 24 mol% of amorphous BN. Increasing p_{N_2} further results, however, in a dramatic rise of hardness to values of ~ 32 GPa. Here, the phase composition according to Table 1 and Fig. 4 is that of a nano-composite with ~ 6 nm CrN grains surrounded by just ~ 13 mol% BN, providing for the observed enhanced mechanical integrity. However, the increase in modulus with rising p_{N_2} is not as pronounced as for the hardness. This might be attributed to the dual-phase of those coatings grown at high p_{N_2}, where the low CrN grain size and the BN grain boundary phase contribute to a low modulus. Nevertheless, the high hardness and low modulus result in a higher H/E ratio (a descriptive parameter for the tolerance towards plastic deformation [27]) at high p_{N_2}. Thus, not surprisingly the hard coatings should

behave more elastic and may therefore be more damage tolerant as the softer coatings at low p_{N_2}.

The average friction coefficients for the Cr-B-N films deposited at $p_{N_2} \geq 28$ % are constant at ~ 0.43, with negligible differences between the respective coatings. An example of its development with sliding distance is shown in Fig. 6. This value is conform with data commonly published for CrN coatings [28]. Thus, the presence of ~ 13 mol% BN ($p_{N_2} \geq 28$ %) does not result in a beneficial effect, even though h-BN is commonly considered a solid lubricant [4]. This is presumably due to its rather low phase fraction but also its amorphous nature, which does not provide for the required macroscopic shear systems (see reference [19] for details).

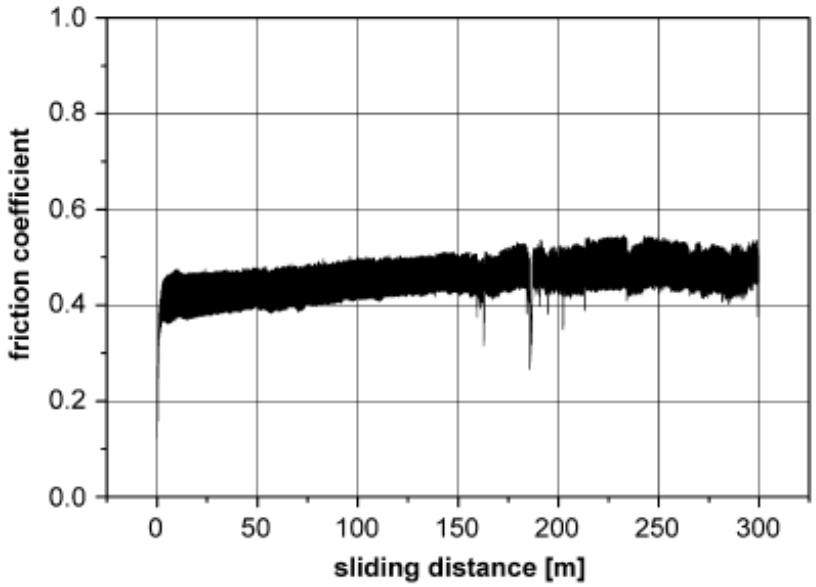

Figure 6: Development of the friction coefficient with sliding distance for the Cr-B-N coating deposited at p_{N2} = 28 % exemplifying the behaviour of all CrN-BN dual-phase coatings ($p_{N2} \geq 28$ %).

The films synthesized with $p_{N_2} \leq 22$ % failed already after 30 – 60 m sliding distance due to a lack of mechanical integrity and adhesion to the high-speed steel substrates. Wear resistance for the higher N-contaning coatings was much better, as exemplified for the coating deposited at p_{N_2} = 28 % by the slight abrasion grooves and the low average depth of the wear scar of ~ 130 nm (see Figs. 7a and b).

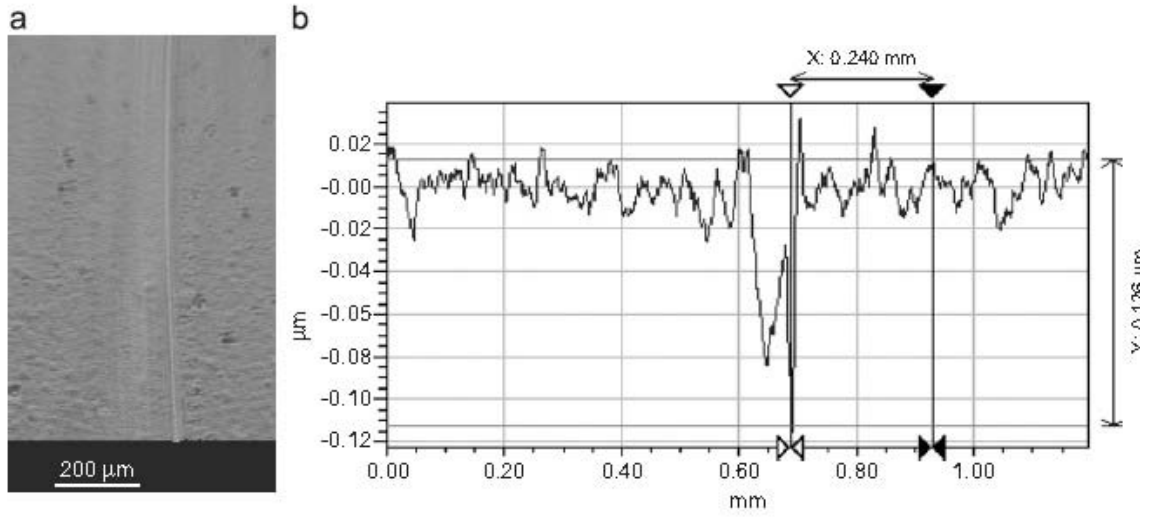

Figure 7: (a) Optical 3-dimensional profilometer image of the wear track of the Cr-B-N coating deposited at p_{N2} = 28 % after 300 m dry sliding and **(b)** corresponding cross-sectional depth profile.

4. Conclusions

Cr-B-N coatings were prepared by reactive magnetron sputtering of a Cr-B target with 20 at.% B at various N_2 partial pressures (p_{N_2}) from 0 % to 64 % of the total pressure (P_{Ar} + p_{N_2}). The Cr/B target ratio is roughly maintained in the coatings for non-reactive sputtering, whereas in reactively grown coatings BN forms preferentially over Cr-borides as soon as sufficient nitrogen is available in the discharge. Thus, an amorphous Cr-rich structure is obtained at lower N_2 fractions ($p_{N_2} \leq 11$ %), which transforms to a nano-crystalline nitride-based structure within the Cr_2N (61 mol%) - CrN (14.7 mol%) - BN (24 mol%) phase field for $p_{N_2} \leq 22$ %. Beyond that, the nitrogen concentration saturates ($p_{N_2} \geq$ 28 %) resulting in ~ 87 mol% CrN with a crystallite size of ~ 6 nm embedded in ~ 13 mol% amorphous BN. The under-stoichiometric coatings deposited at low N_2 fractions ($p_{N_2} \leq 11$ %) exhibit only moderate hardness and modulus values of ~ 15 and ~ 150 GPa, respectively, which is maintained even for the coating within the ternary Cr_2N-CrN-BN phase field ($p_{N_2} \leq 22$ %) presumably due to the large fraction (24 mol%) of amorphous BN. However, a dramatic increase in hardness to ~ 32 GPa is obtained as soon as the nitrogen concentration saturates for the CrN-BN dual phase structure ($p_{N_2} \geq 28$ %), whereas the modulus increases only moderately. This can be understood by the nano-composite structure of these coatings were sub-10-nm CrN grains are surrounded by few monolayers of BN. For that reason, the hardness of the Cr-B-N coatings synthesized at high p_{N_2} exceeds the values commonly observed for CrN substantially. The BN phase, on the other hand, does not provide for a solid lubrication effect, as the coefficient of friction is comparable to pure CrN coatings.

Acknowledgments

This work was financially supported by the European Union within the NAPILIS Specific Targeted Research Project (contract NMP3 CT 2003 505622). The authors thank Mr. Alexander Fian (Joanneum Research, Weiz, Austria) for XPS analyses and Mr. Gerhard Hawranek for performing SEM and EPMA investigations. J.N. acknowledges financial support by the Christian Doppler Society and the companies Plansee GmbH, Lechbruck, Germany, and Oerlikon Balzers AG, Balzers, Liechtenstein.

References

1. Mayrhofer P H, Mitterer C, Hultman L, Clemens H. Progr Mater Sci 2006; 51: 1032.
2. Sato T, Tada Y, Ozaki M, Hoke K, Besshi T. Wear 1994; 178: 95.
3. Su Y L, Yao S H, Wu C T. Wear 1996; 199: 132.
4. Brotherton R J, Steinberg H. Progress in boron chemistry. Vol 2. Oxford: Pergamon Press, 1970. p. 173 – 230.
5. Mitterer C, Übleis A, Ebner R. Mater Sci Eng A 1991; 140: 670.
6. Brandstetter E, Mitterer C, Ebner R. Thin Solid Films 1991; 210: 123.
7. Mitterer C, Rödhammer P, Störi H, Jeglitsch F. J Vac Sci Technol A 1989; 7: 2646.
8. Mitterer C, Rauter M, Rödhammer P. Surf Coat Technol 1990; 42: 351.
9. Matthes B, Broszeit E, Kloos K H. Surf Coat Technol 1990; 43-44: 721.
10. Wen L S, Chen X Z, Yang Q Q, Zheng Y Q, Chuang Y Z. Surf Eng 1990; 6: 41.
11. Knotek O, Jungblut F, Breidenbach K. Vacuum 1990; 41: 2184.
12. Rogl P, Schuster J C. Phase diagrams of ternary boron nitride and silicon nitride systems. Materials Park, OH: ASM, 1992. p. 20-25.
13. Rother B, Kappl H. Surf Coat Technol 1995; 73: 14.
14. Rother B, Kappl H. Surf Coat Technol 1997; 96: 163.
15. Aouadi S M, Namavar F, Tobin E, Finnegan N, Haasch R T, Nilchiani R, Turner J A, Rohde S L. J Appl Phys 2002; 91: 1040.
16. Gorishnyy T Z, Mihut D, Rohde S L, Aouadi S M. Thin Solid Films 2003; 445: 96.
17. Sakamaoto Y, Nose M, Mae T, Honbo E, Zhou M, Nogi K. Surf Coat Technol 2003; 174-175: 444.
18. Zhou M, Nose M, Nogi K. Surf Coat Technol 2004; 183: 45.
19. Budna K P, Mayrhofer P H, Hegedũs É, Kovács I, Tóth L, Pécz B, Mitterer C. Surf Coat Technol, submitted.
20. Hegedũs É, Kovács I, Tóth L, Pécz B, Budna K P, Mitterer C. Vacuum 2008 ; 82 : 209.
21. Losbichler P, Mitterer C. Surf Coat Technol 1997; 97: 568.
22. Losbichler P, Mitterer C, Gibson P N, Gissler W, Hofer F, Warbichler P. Surf Coat Technol 1997; 94/95: 297.
23. Brundle C R, Evans C A, Wilson S. Encyclopaedia of materials characterisation. Greenwich, USA: Manning Publication, 1992.
24. HSC 5.11, HSC Chemistry. Pori, Finland: Outokumpu Research Oy, 2004.
25. NIST X-ray Photoelectron Spectroscopy Database. http://srdata.nist.gov/xps/.
26. Wagner C D. Handbook of XPS, Minnesota: Physical Electronics, 1995.
27. Greenewood J A, Williamson J B P. Proc Roy Soc London A 1966; 295: 300.
28. Carrera S, Salas O, Moore J J, Woolverton A, Sutter E. Surf Coat Technol 2003; 167: 25.

Publication III

Synthesis and characterisation of sputtered hard coatings of Cr-N/MoS_x

K.P. Budna[1], C. Walter[2], R. Spicak[1], C. Mitterer[2]

1. Materials Center Leoben Forschung GmbH, Franz-Josef-Sraße 13, A-8700 Leoben, Austria
2. Department of Physical Metallurgy and Materials Testing, University of Leoben, Franz-Josef-Straße 18, A-8700 Leoben, Austria

Abstract

For protective coatings to be applied to engine components, a combination of high wear resistance with low friction is needful to increase performance and lifetime. Auspicious candidates have to conjoin the properties of a conventional hard coating with the low friction coefficient of a solid lubricant.

This study reports about thin films synthesized by reactive magnetron sputtering of a Cr target with 25 area% MoS_2 inlays. Nitrogen at different partial pressures was used as reactive gas. The chemical composition and microstructure were analyzed by electron probe microanalysis, X-ray diffractometry and X-ray photoelectron spectroscopy. Residual stress was determined with the substrate-curvature method and the mechanical properties were investigated by microindentation. To examine the tribological behavior, ball-on-disc tests were performed at room temperature. The desired low friction behavior could not be observed due to an insufficient content and lack of crystalline structure of the MoS_2 phase in the coatings.

Keywords: sputtering, hard coatings, molybdenum disulfide, chromium nitride, nanocomposite

1. Introduction

Physical vapour deposited Cr_2N and CrN based coatings are well known for their high hardness, good corrosion, and wear resistance facilitating various industrial applications [1-4]. A large number of investigations have been reported since the early 1990s focusing mainly on the influence of the processing parameters on film composition and properties such as microhardness or thermal stability [5-7]. Another important attribute of Cr-N coatings is their low friction coefficient of ~ 0.45 [8]. Nevertheless, there is a high demand for a further reduction of the friction coefficient and the development of self-lubricating CrN based coatings. A possible strategy to achieve this aim is embedding of a lubricating phase into the hard matrix. Well-known solid lubricants are e.g. graphite, hexagonal BN, MoS_2 or WS_2 [9,10]. All of them are characterised by their layered substructure. There

have been many attempts to develop and synthesise ternary and/or quaternary systems which combine the advantages of hard coatings and solid lubricants, for example the system Cr-B-N [11,12] or Cr-C-N [13]. Nevertheless, until now the use of MoS_2 and WS_2 as lubricant phase for CrN coatings has not been satisfactorily described in literature.
It is the aim of this work to investigate the chemical, structural, mechanical and tribological properties of sputtered coatings in the system Cr-N/MoS_2 deposited at different nitrogen partial pressures p_{N2}. Therefore, three coatings with were deposited at p_{N2}/p_{total} pressure ratios of 11, 22, and 28 % from a segmented Cr-MoS_2 target and investigated with electron probe microanalysis (EPMA), X-ray diffraction (XRD), X-ray photoelectron spectroscopy (XPS), microhardness testing and ball-on-disc dry-sliding experiments.

2. Experimental

Coatings were synthesised by reactive dc unbalanced magnetron sputtering from a Cr target with MoS_2 inlays in an Ar-N_2 glow discharge using a bias voltage of -50 V. To achieve a coverage of 25 area% MoS_2 in the sputter track of the Cr target with dimensions of ∅ 150 × 6 mm, 20 circular holes with a diameter of 8 mm and a depth of 4 mm were filled with matching inlays of sintered MoS_2. AISI M2 high speed steel discs and mirror polished Si (100) wafers were used as substrate materials. The AISI M2 substrates were quenched and annealed to a hardness of 65 HRC, ground and polished. Before mounting on the substrate holder, the substrates were ultrasonically precleaned in acetone and ethanol. The target was presputtered for 5 min at a current of 1.5 A in Ar atmosphere at 0.4 Pa, and the substrates were ion etched using an Ar glow discharge with -1250 V and 2.6 Pa. The target to substrate distance was 10 cm. During the 60 min deposition time, the substrate temperature was kept constant at 300°C and the target power density was 3.8 Wcm^{-2}. All depositions were run at a total pressure of 0.4 Pa while the p_{N2}/p_{total} pressure ratio varied from 11 to 28 %.
Coating thickness was measured by a CSM spherical abrasion test. Coating morphology was studied on fractured cross-sections of coatings on Si substrates investigated by scanning electron microscopy (SEM) using a Zeiss EVO-50. The chemical composition of the coatings was characterised by EPMA. The Mo and S content was measured by wavelength dispersive analysis with a MICROSPEC WDX-3PC using elemental Mo and CuFeS standards. For the determination of the Cr and N content, energy dispersive analysis was used.
Phase composition and microstructure were explored by XRD using a Siemens D500 diffractometer. X-ray diffraction patterns were recorded in Bragg-Brentano mode using Cu K_α radiation. Additionally, XPS analysis was conducted with an Omicron Multiprobe system. A monochromatic Al K_α X-ray beam was utilised. Spectra were recorded after annealing at 350°C for 1 h to clean the surface.
Coatings on silicon substrates were used for stress measurement by means of the substrate curvature method [14] applied for 21×6.5×0.38 mm Si (100) strips coated on one

side. The curvature was measured with an optical method using two parallel laser beams and the stresses were evaluated from the substrate curvature radius using the modified Stoney equation [15]. A detailed derivation and thermal substrate properties can be found in literature [16].

Indentation modulus E and universal plastic hardness H of the coatings on Si substrates were determined from the loading and unloading segments during 20 computer controlled microindentations using a Fischerscope H100C with a Vickers diamond tip. An indentation load of 30 mN was chosen.

The coefficient of friction was measured with dry-sliding ball-on-disc tests at room temperature and a humidity of ~ 40 % using a CSM tribometer. Alumina balls with 6 mm in diameter were taken as counterparts. All tests were performed over a distance of 300 m at a load of 2 N and a wear track radius of 0.5 cm.

3. Results and discussion

3a. Coating composition and structure

With increasing p_{N2}/p_{total} pressure ratio, the coating thickness decreased from 4.5 to 1.5 µm (see Table 1) as a result of the decreasing growth rate due to target poisoning [17].

Table 1: Film thickness and growth rates of the coatings deposited at different p_{N2}/p_{total}.

p_{N2}/p_{total} (%)	deposition time (min)	thickness (µm)	growth rate (nm/s)
11	60	4.5	1.25
22	60	3.5	0.97
28	60	1.3	0.36

The chemical composition of the coatings and their quantitative contents determined with EPMA are listed in Table 2. It can be seen that the MoS_2 surface coverage of 25 area% in the wear track of the Cr target results in 5 at.% Mo and 7.1 at.% S in the coating deposited at the lowest p_{N2}/p_{total} pressure ratio. While the Mo content stays approximately constant, the S content decreases to 2.4 at.% with increasing nitrogen partial pressure. Consequently, the Mo/S ratio, which is 0.5 in the target inlays, increases from 0.7 to 1.7 in the deposited coatings with p_{N2}/p_{total} pressure ratio increasing from 11 to 28 %. Fleischauer et al. observed by analysis of the chamber gas before and after film deposition that the concentration of H_2S and SO_2 in the contaminant was higher after sputtering than before [18]. Thus, it is assumed that the S loss observed is due to the formation of volatile components which leave the deposition chamber.

Table 2: Chemical composition analysed with EPMA of the coatings deposited at different p_{N2}/p_{total}.

p_{N2}/p_{total} (%)	composition (at.%)				Cr/N	Mo/S
	Cr	N	Mo	S		
11	70.4	17.5	5	7.1	4.3	0.7
22	52.5	39.1	4.1	4.3	1.3	1.0
27	44.9	48.5	4.1	2.4	0.9	1.7

With increasing p_{N2} a significant increase in N content is obtained in the coatings and correspondingly the Cr content decreases. Therefore, the Cr/N ratio of the deposited coatings decreases from 4.3 to a slightly overstoichiometric value of 0.9. This corresponds to earlier investigations within the system Cr-N [7,19,20].

Scanning electron microscopy fracture cross-sections of the authors Cr-N/MoS_2 films reveal a featureless structure with a smooth surface for all investigated N_2 partial pressures, see Fig.1. The cross-sections clearly show the reduction of the coating thickness due to target poisoning with increasing p_{N2} (cf. Table 1) [20].

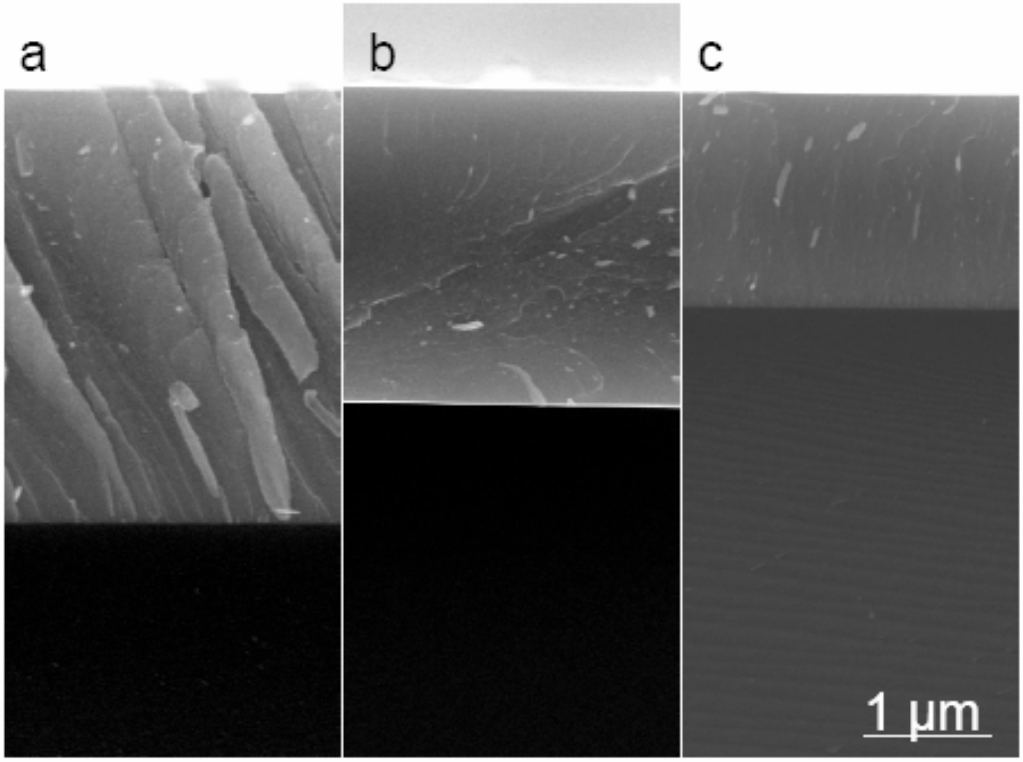

Figure 1: SEM fracture cross-sections of the coatings deposited at p_{N2}/p_{total} pressure ratios of **(a)** 11 %, **(b)** 22 %, and **(c)** 28 %.

X-ray diffraction patterns of the coatings as deposited and after annealing are presented in Fig. 2a and b, respectively. The diffraction peaks at ~ 33 and ~ 69° can be attributed to the Si substrate. In the as deposited state, the structure of the coating deposited at the lowest p_{N2}/p_{total} pressure ratio appears to be mainly X-ray amorphous, as evidenced by a high background covering the diffraction angle range between 33 and 50°. Only two unambiguous diffraction peaks can be detected which coincide with standard peak positions of Cr_2N. For higher nitrogen partial pressures, the coatings are crystalline and all peaks can be attributed to CrN and/or Cr_2N.

Owing to small grain size and internal stresses in the coatings the diffraction peaks are broad and overlapping. An unambiguous attribution to either CrN or Cr_2N for the diffraction peaks positioned at 43 and 63° is not possible. According to the chemical composition and

a peak separation after annealing (Fig. 2b) it is supposed that both phases are present and diffraction peaks are overlapping in the as deposited state. A shift of the CrN peaks to lower angles at a p_{N2}/p_{total} pressure ratio of 28 % can be observed. A similar effect has been stated in literature before and is attributed to substitution of Cr by Mo in the nitride [21-23]. It may also be a consequence of the compressive residual stress in the coating. No indication for the presence of crystalline MoS_2 is found.

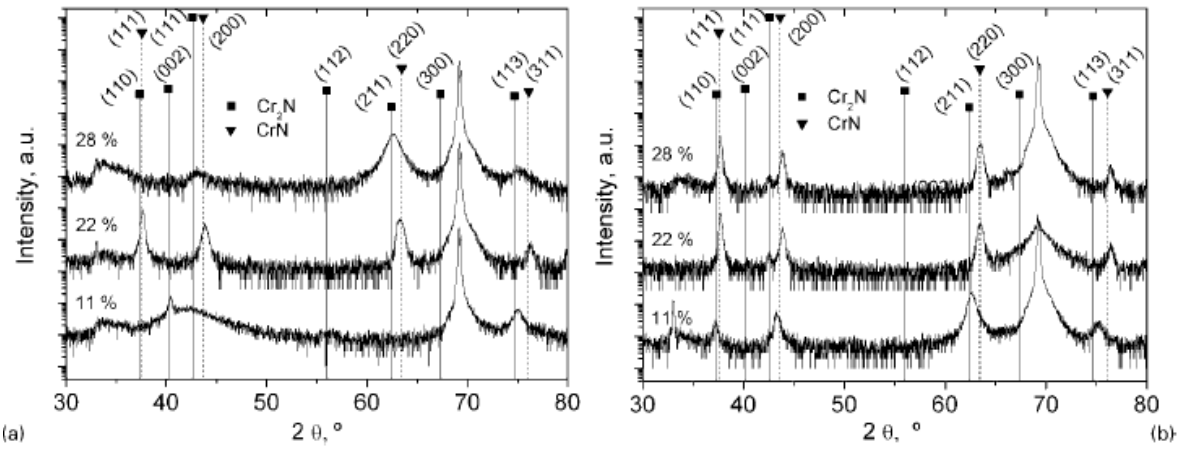

Figure 2: XRD patterns of the coatings **(a)** as–deposited and **(b)** after vacuum annealing at 550°C; drop lines mark standard peak positions for Cr_2N (JCPDS pattern 00-035-0803), and CrN (JCPDS pattern 01-076-2494) with relative heights indicating relative intensities.

To annihilate stresses and initialise grain coarsening, the coatings were annealed for 1 h at 550°C in vacuum with a pressure of $2x10^{-4}$ Pa to avoid oxidation. The XRD patterns of the annealed films are presented in Fig.2b. For the coating deposited with a p_{N2}/p_{total} pressure ratio of 11 %, a Cr_2N dominated structure is obtained. For higher nitrogen partial pressures, the XRD patterns exhibit a CrN dominated structure. This is in accordance with the EPMA results indicating a high Cr/N ratio for the coating deposited with p_{N2}/p_{total} = 11 % (Cr/N ratio of 4.3) and a stoichiometry close to CrN for films deposited with $p_{N2}/p_{total} \geq 22$ % (Cr/N ratios of 1.3 and 0.9, respectively, see Table 2). The observed correlation between phase formation and nitrogen partial pressure complies with literature data for the Cr-N system [7,19,20]. No crystalline MoS_2 phase could be detected by XRD in the annealed samples as well.

Since XRD measurements did not yield information about how S is incorporated in the coating, supplementary XPS analysis was performed. Fig.3a and b show the recorded spectra for the N 1s and S 2p energy regions, respectively. The shift to lower binding energies for higher nitrogen partial pressures of the N 1s peak confirms the change from a Cr_2N (binding energy 397.2 eV) to a CrN (binding energy 396.4 eV) dominated structure [24,25]. The decreasing intensity of the S 2p peak confirms the lower S content for higher p_{N2}/p_{total} during deposition. The S $2p_{3/2}$ peak of MoS_2 has a binding energy of 162.4 eV [24,26]. The peak shown in Fig.3b compares well to a typical spectrum of the S 2p energy

region for MoS_x found in literature [27,28]. Thus, it seems reasonable to conclude that an X-ray amorphous MoS_x phase is formed.

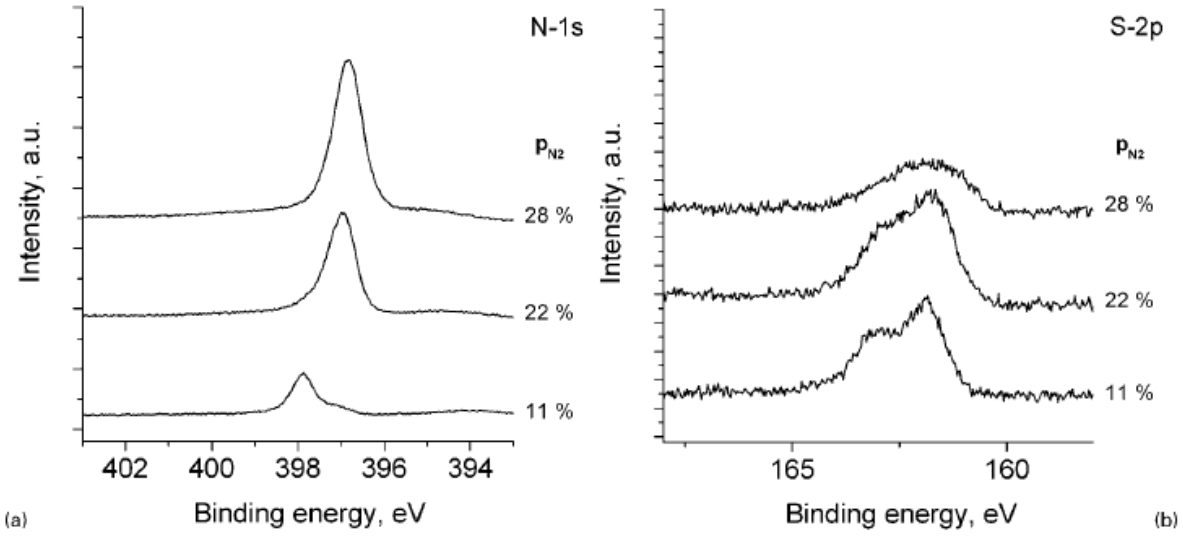

Figure 3: XPS spectra of the **(a)** N 1s and **(b)** S 2p energy region of the coatings deposited at different p_{N2}/p_{total}.

3b. Mechanical and tribological properties

The residual stress of the coatings is shown in Fig.4a. For the coating deposited at the lowest p_{N2}/p_{total} pressure ratio, 200 MPa tensile stress was measured. With increasing nitrogen partial pressure, the residual stresses become compressive and reach a value of ~ -1 GPa for a p_{N2}/p_{total} pressure ratio of 28 %. The increase in compressive stress with increasing p_{N2} during deposition is attributed to a decreasing substoichiometry of the chromium nitrides and a higher ratio of ions to neutrals arriving at the substrate due to a lower deposition rate.[7] This increased ion bombardment also leads to a smaller grain size which can be estimated from the greater full width at half maximum of the diffraction peaks for the coating deposited at p_{N2}/p_{total} = 28 %.

Hardness H and indentation modulus E of the coatings are presented in Fig.4b and c as a function of p_{N2}/p_{total} for the as-deposited state and after annealing. As-deposited, the coating hardness increases from 11 GPa to 23 GPa with increasing p_{N2}/p_{total} pressure ratio. The high value corresponds to literature data for crystalline CrN_x films [20], while the low value may be attributed to the mainly amorphous microstructure of the respective coating. The continuous increase in hardness also correlates to an increase in the indentation modulus and compressive stress.

Such dependence of hardness on compressive stress for pure Cr–N coatings has been shown by Mayrhofer et al. [7]. For the annealed coatings, a similar tendency can be observed. The indentation modulus increases along with the hardness. Before annealing, a maximum indentation modulus of 175 GPa is measured. After annealing, a significantly higher value of 220 GPa is reached. Both values lie within the quite wide range of elastic moduli of CrN that can be found in literature [29].

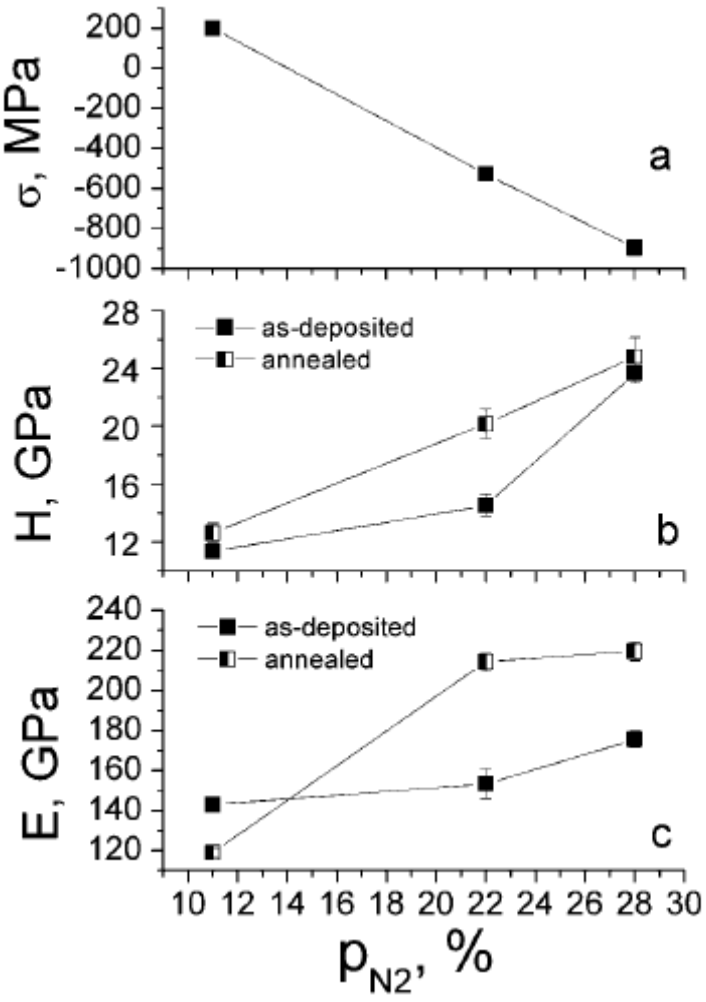

Figure 4: (a) Biaxial stresses σ, **(b)** microhardness H, and **(c)** indentation modulus E of the coatings as-deposited and after annealing as a function of p_{N2}/p_{total}.

The tribological investigations of the coatings were conducted with dry-sliding ball-on-disc tests. The film synthesised at a p_{N2}/p_{total} pressure ratio of 11 % failed after ~ 25 m due to bad adhesion on the AISI M2 steel substrate and no friction coefficient could be determined. For the coatings deposited at $p_{N2}/p_{total} \geq 22$ %, an average friction coefficient of 0.55 ± 0.05 against a corundum ball was measured. This agrees well with literature data for CrN dominated films [8]. Thus, no significant reduction of the friction coefficient compared to pure CrN films can be observed. This result suggests that the content of MoS_2 is too low and the formation of a lamellar structure which could support shearing has not taken place [30].

4. Conclusions

Coatings within the system Cr-N/MoS_2 were synthesised by unbalanced reactive magnetron sputtering using a Cr target with MoS_2 inlays (25 area% MoS_2) in an Ar/N_2 atmosphere. The content of Mo and S in the coatings was significantly lower than the target composition and the S content decreased even further with increasing p_{N2}/p_{total}

pressure ratio. Indications for the presence of an amorphous MoS_x phase in the coatings could be found. Furthermore, no evidence for the desired low-friction effect of MoS_2 was found in ball-on-disc dry-sliding experiments. The observed phase formation and mechanical properties can all be attributed to Cr_2N and CrN phases and seem to be largely unaffected by the presence of Mo and S. Thus, reactive magnetron cosputtering of Cr and MoS_2 did not prove successful in the deposition of self-lubricating coatings.

Acknowledgments

This work was financially supported by the European Union within the NAPILIS Specific Targeted Research Project (contract NMP3 CT 2003 505622). The authors wish to thank Mr. Gerhard Hawranek for performing SEM and EPMA measurements.

References

1. T. Hurkmans, D.B. Lewis, J.S. Brooks and W.-D. Münz: Surf. Coat. Technol. 1996, **86/87**, 192-199.
2. S.H. Yao and Y.L. Su: Wear, 1997, **212**, 85-94.
3. J.N. Tu, J.G. Duh and S.Y. Tsai: Surf. Coat. Technol., 2000, **133/134**, 181-185.
4. T. Sato, Y. Tada, M. Ozaki, K. Hoke and T. Besshi: Wear, 1994, **178**, 95-100.
5. M. Pakala and R.Y. Lin: Surf. Coat. Technol., 1996, **81**, 233-239.
6. P. Hones, R. Sanjines and F. Lévy : Surf. Coat. Technol., 1997, **94-95**, 398-402.
7. P.H. Mayrhofer, G. Tischler and C. Mitterer: Surf. Coat. Technol., 2001, **142-144**, 78-84.
8. S. Carrera, O. Salas. J.J. Moore, A. Woolverton and E. Sutter: Surf. Coat. Technol., 2003, **167**, 25-32.
9. W.J. Bartz: Wear, 1978, **49**, 1-18.
10. B. Bhushan: "Modern tribology handbook", Volume 2, 793; 2001, Baton Rouge, CRC Press.
11. B. Rother and H. Kappl: Surf. Coat. Technol., 1995, **73**, 14-17.
12. B. Rother and H. Kappl: Surf. Coat. Technol., 1997, **96**, 163-168.
13. G. Cholvy, J.L. Derep and M. Gantois: Thin Solid Films, 1985, **126**, 51-60.
14. A. Brenner and S. Senderoff: J. Res. Natl. Bur. Stand., 1949, **42**, 105-123.
15. J. D. Wilcock and D. S. Campbell: Thin Solid Films, 1969, **3**, 3-12.
16. P. H. Mayrhofer and C. Mitterer: Surf. Coat. Technol., 2000, **133/134**, 131-137.
17. B. Chapman: "Glow discharge processes", 1980, New York, John Wiley & Sons.
18. P.D. Fleischauer and R. Bauer: Tribol. Trans., 1988, **31**, 239-250.
19. G. Wei, A. Rar and J.A. Barnard: Thin Solid Films, 2001, **398-399**, 460-464.
20. Z. Han, J. Tian, Q. Lai, X. Yu and G. Li: Surf. Coat. Technol., 2003, **162**, 189-193.
21. E.Y. Choi, M.C. Kang, D. H. Kwon, D. W. Shin and K.H. Kim: J. Mater. Process. Technol., 2007, **187-188**, 566-570.
22. K. H. Kim, E. Y. Choi, S.G. Hong, B.G. Park, J.H. Yoon and J.H. Yong: Surf. Coat. Technol., 2006, **201**, 4068-4072.
23. R. Gilmore, M.A. Baker, P.N. Gibson, W. Gissler, M. Stoiber, P. Losbichler and C. Mitterer: Surf. Coat. Technol., 1998, **108-109**, 345-351.
24. NIST X-ray Photoelectron Spectroscopy Database, http://srdata.nist.gov/xps/
25. C.D. Wagner: "*Handbook of XPS"*, 1995, Minnesota, Physical Electronics.

26. L. Benoist, D. Gonbeau, G. Pfister-Guillouzo, E. Schmidt, G. Meunier and A. Levasseur: Thin Solid Films, 1995, **258**, 110-114.
27. J.-G. Choi, D. Choi and L.T. Thompson: Appl. Surf. Sci., 1997, **108**, 103-111.
28. M.A. Baker, R. Gilmore, C. Lenardi and W. Gissler: Appl. Surf. Sci., 1999, **150**, 255-262.
29. H.-Y. Chen, C.-J. Tsai and F.-H. Lu: Surf. Coat. Technol., 2004, **184**, 69-73.
30. K.J. Wahl, M. Belin and I.L. Singer: Wear, 1998, **214**, 212-220.

Publication IV

Synthesis and characterisation of sputtered hard coatings within the system Cr-N/WS_x

K.P. Budna[1, 2], C. Mitterer[2]

1. Materials Center Leoben Forschung GmbH, Franz-Josef-Sraße 13, A-8700 Leoben, Austria
2. Department of Physical Metallurgy and Materials Testing, University of Leoben, Franz-Josef-Straße 18, A-8700 Leoben, Austria

Abstract

CrN_x-WS_x films were deposited by unbalanced magnetron co-sputtering and investigated concerning their structure as well as their mechanical and tribological properties. A Cr target with WS_2 inserts was used to adjust coverage fractions of the erosion track of 25 and 37.5 area%. Deposition was done in an Ar/N_2 atmosphere with different nitrogen fractions (p_{N_2} = 0, 11, and 28 %). Chemical analysis and crystalline structure were investigated by electron probe microanalysis and X-ray diffraction. Hardness and indentation modulus were determined by micro-indentation, stresses were measured by the substrate-curvature method, and the tribological behaviour of the coatings was evaluated by dry-sliding ball-on-disc tests. With increasing p_{N_2}, a transformation from a Cr solid solution to a Cr_2N dominated structure was observed, which resulted in a moderate increase in hardness and elastic modulus. Due to the observed sub-stoichiometry of the formed WS_2 phase, no friction reduction compared to single-phase CrN coatings was obtained.

Keywords: magnetron sputtering, thin films, CrN, WS_2, tribology

1. Introduction

Modern protective hard coatings for tools and automotive components are well established since the early 1990-ies. The rising requirements imposed on these coatings, e.g. due to increased cutting speeds or reduced fuel and oil consumption, demand more and more continuative and extensive investigations and advancements. In addition to their hardness, thermal stability and oxidation resistance, also their friction and wear behaviour is decisive for their use in technical devices. Several well-known solid lubricants like diamond-like carbon or hexagonal boron nitride are considered for these applications, but also metal dichalcogenides like MoS_2 and WS_2 are attractive candidates for low-friction films. There, the lamellar structure of type II textured MX_2 films (M = Mo, W; X = S, Se)

and the resultant weak chemical bonds between MX_2 planes enable intercrystalline gliding and low friction coefficients.[1-7]

Many investigations have been done and published about MoS_2 and WS_2 coatings and their characteristics and properties.[8-15] Nevertheless, very limited reports about combinations of these layered MX_2 phases with a common hard coating material like CrN in the form of a nanocomposite are available. In spite of the relatively low friction coefficient of CrN films ($\mu \sim 0.45$),[16] a further reduction of friction losses while maintaining the typical CrN properties like excellent wear, oxidation and corrosion resistance and high hardness[17-23] by addition of MX_2 phases would be a promising approach to increase the performance of e.g. engine components like piston rings. In a previous paper, we explored the possibility of adding MoS_2 to CrN.[24] Within this study, coatings within the system Cr-N/WS_x with different chemical compositions have been synthesised by magnetron co-sputtering and their structure and morphology as well as mechanical and tribological properties have been examined.

2. Experimental details

Coatings were synthesised by reactive dc unbalanced magnetron co-sputtering from a Cr mosaic target with WS_2 inlays in an Ar-N_2 glow discharge using a bias voltage of -50 V. To achieve different WS_2 target coverage fractions in the erosion track of the Cr target with dimensions of $\varnothing$ 150 $\times$ 6 mm, 30 circular blind holes with diameters of 8 mm and depths of 4 mm were filled with matching inlays of sintered WS_2 and Cr rods, respectively (see Fig.1). For a 25 area% WS_2 target covering fraction, 20 WS_2 inlays in addition to 10 Cr inlays were placed in these holes, whereas for a covering of 37.5 area% WS_2, all holes were filled with WS_2. AISI M2 high-speed steel discs and mirror polished Si (100) wafers were used as substrate materials.

Fig. 1: Cr mosaic target with circular blind holes for WS_2 and Cr inlays used for coating deposition.

The AISI M2 substrates were quenched and annealed to a hardness of 65 HRC, ground and polished to 1 µm diamond polish. Before mounting on the substrate holder, the substrates were ultrasonically pre-cleaned in acetone and ethanol. The target was pre-sputtered for 5 min at a current of 1.5 A in Ar atmosphere at 0.4 Pa, and the substrates

were ion etched using an Ar glow discharge with -1250 V and 2.6 Pa. The target to substrate distance was about 10 cm. During the 60 min deposition time, the substrate temperature was kept constant at 300 °C and the target power density was 3.8 W cm^{-2}. All depositions were run at a total pressure of 0.4 Pa while the p_{N_2}/p_{total} pressure ratio was varied between 0 and 28 %.

Coating thickness was measured by a CSM CaloTest spherical abrasion test. Coating morphology was studied on fractured cross-sections of coatings on Si substrates investigated by scanning electron microscopy (SEM) using a Zeiss EVO-50. The chemical composition of the coatings was characterised by electron probe micro-analysis (EPMA). There, the W and S content was measured by wavelength-dispersive analysis with a MICROSPEC WDX-3PC using elemental W and CuFeS standards. For the determination of the Cr and N content, energy-dispersive analysis was used. Phase composition and microstructure were explored by X-ray diffraction (XRD) using a Siemens D500 diffractometer. X-ray diffraction patterns were recorded in Bragg-Brentano mode using Cu K_α radiation.

Indentation modulus E and universal plastic hardness H of the coatings on Si (100) substrates were determined from the loading and unloading segments during 20 computer-controlled micro-indentations using a Fischerscope H100C with a Vickers diamond tip. To achieve indentation depths of 10 % of the coating thickness, indentation loads of 50 and 100 mN were chosen, depending on the particular film thickness.

Stress measurement by means of the substrate curvature method[25] were done on 21×6.5×0.38 mm Si (100) strips coated on one side. The curvature was measured with an optical method using two parallel laser beams and the stresses were evaluated from the substrate curvature radius using the modified Stoney equation.[26] A detailed derivation and thermal substrate properties can be found in ref. [27]

The coefficient of friction was measured with dry-sliding ball-on-disc tests at room temperature and a relative humidity of ~ 40 % using a CSM tribometer. Alumina balls with 6 mm in diameter were taken as counterparts. All tests were performed over a distance of 300 m at a load of 2 N and a wear track radius of 5 mm.

3. Results and Discussion

The thicknesses, chemical compositions of the coatings grown at the two WS_2 target coverage fractions of 25 and 37.5 area% and the respective Cr/N and W/S atomic ratios of the Cr-N/WS_x films, as analyzed by EPMA, are listed in Table 1 for different N_2 partial pressures. The coatings deposited without nitrogen contain for the 25 area% WS_2 covered target 91.2 at.% Cr, 5.1 at.% W and 3.7 at.% S, whereas a composition of 86 at.% Cr, 6.7 at.% W and 7.3 at.% S has been reached for the target with a 37.5 area% WS_2 target coverage fraction. With p_{N_2} increasing to 28 %, a significant increase in N content up to 37.4 at.% for the 25 area% and 39.6 at.% for the 37.5 area% covered target, respectively,

was obtained and correspondingly the Cr content decreases to 56.5 and 54.7 at.%, respectively. The Cr/N atomic ratio (see Table 1) decreases to ~ 1.5 and ~ 1.4 for the 25 and 37.5 area% WS_2 target coverage fractions, respectively; however, a ratio of 1 indicating stoichiometric composition of the CrN phase has not been reached. The increasing p_{N_2} also results in decreasing W and S contents, i.e. to 4.2 and 1.9 at.% for the 37.5 area% WS_2 target coverage fraction and to 5.2 and 0.6 at.% for the coverage fraction of 25 area%. The W/S atomic ratio likewise decreases with raising p_{N2} from ~ 1.4 and ~ 0.9 without N_2 to ~ 2.2 and ~ 9.2 at p_{N_2} = 28 % for WS_2 target coverage fractions of 25 and 37.5 area%, respectively. This corresponds to a sub-stoichiometric composition compared to the W/S atomic ratio of 0.5 for WS_2, and is in good agreement to earlier publications on MoS_2 containing coatings.[28]

Table 1: Film thickness, chemical composition, as well as Cr/N and W/S atomic ratios of Cr-N/WS_x films as analyzed by EPMA as a function of N_2 partial pressure and WS_2 area target covering fraction ("n.d." means "not detectable").

p_{N_2} [%]	WS_2 [area%]	thickness [µm]	composition (at.%)				Cr/N	W/S
			Cr	N	W	S		
0	25	7.4	91.2	n.d.	5.1	3.7	n.d.	1.36
11	25	7.4	75.8	15.9	4.5	3.8	4.76	1.15
28	25	6.5	56.5	37.4	4.2	1.9	1.51	2.19
0	37.5	7.1	86.0	n.d.	6.7	7.3	n.d.	0.91
11	37.5	6.4	73.3	16.7	6.2	3.8	4.39	1.61
28	37.5	10.3	54.7	39.6	5.2	0.6	1.38	9.23

SEM fracture cross-sections of the films on Si substrates were recorded to obtain first information about the effect of WS_x and nitrogen additions on structure evolution (see Fig. 2). The cross-sections indicate a smooth film surface without major defects and an almost featureless structure. This structure is comparable to CrN coatings grown in the same deposition system at comparable conditions[23]. No unambiguous effect of the N_2 partial pressure on coating thickness and structure evolution was observed (see Table 1 and Fig. 2).

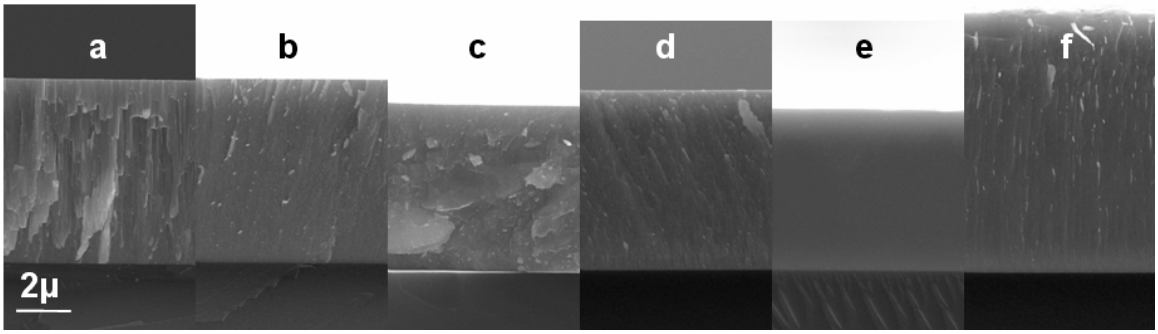

Fig. 2: SEM fracture cross-sections of reactive sputtered Cr-N/WS_x films for 25 area% WS_2 target coverage fraction with p_{N2} increasing from **(a)** 0 through **(b)** 11 to **(c)** 28 % and for 37.5 area% WS_2 target coverage fraction with p_{N2} increasing from **(d)** 0 through **(e)** 11 to **(f)** 28 %.

The XRD patterns of coatings grown on Si (100) substrates are presented in Fig. 3. The standard 2θ positions for WS_2 (JCPDS #08-0237), Cr_2N (JCPDS #35-0803), Cr (JCPDS #06-0694), WN (JCPDS #25-1256) and Si (strong (400) reflection at 2θ ~ 69.2°) are added to the plot. For both coatings deposited without N_2, only the (110) and (211) peaks of the body-centered cubic (bcc) α-Cr phase at 2θ ~ 44.4° and 2θ ~ 81.7°, respectively, can be detected. For the higher WS_2 target coverage fraction, a remarkable shift of these peaks to lower 2θ angles can be observed, which might indicate lattice expansion due to the higher level of W and/or S incorporation in the Cr phase. No unambiguous evidence for the WS_2 phase can be seen, although there is a very small and broad feature at 2θ ~ 33° which might correspond to the overlapping (100) and (101) peaks of WS_2.[29] While this peak might also be attributed to the Si (200) reflection at 2θ = 33.2°, the low intensity and pronounced broadening makes its origin from a highly distorted WS_x phase more likely.

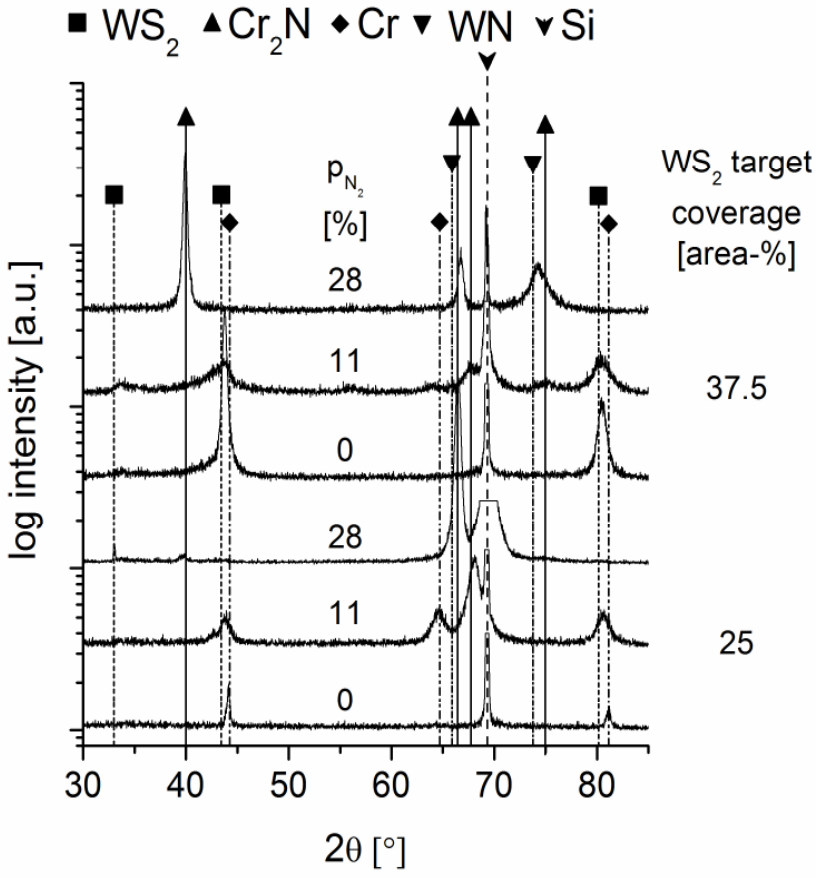

Fig. 3: XRD patterns of Cr-N/WS_x coatings on Si (100) substrates with increasing p_{N_2} and WS_2 target coverage fractions of 25 and 37.5 area%. The peak positions for the α-Cr, Cr_2N, CrN, WN, and WS_2 phases are marked by drop lines.

With p_{N_2} increasing to 11 %, the Cr peaks at 2θ ~ 44.4° and 2θ ~ 81.7° become broader and decrease in intensity, indicating grain refinement due to the increasing level of nitrogen incorporation. In addition, the broad peak at 2θ ~ 64.6° also corresponds to the α-Cr phase. According to Rebholz et al.[30], up to 16 at.% N might be incorporated into the α-

Cr phase, which is in fair agreement with those values given in Table 1. Additional XRD reflections at 2θ ~ 67.4° for both WS_2 target coverage fractions correspond to the hexagonal Cr_2N phase. In agreement to those pattern recorded for the films without nitrogen, additional small broad features can be seen at 2θ ~ 33°, which might again correspond to a WS_x phase and/or the Si substrate. Also here, the low intensity and pronounced broadening of this feature makes the formation of WS_2 more likely and also corresponds well to the observed W/S atomic ratios given in Table 1, indicating a highly defective sub-stoichiometric structure. Thus, we have to conclude that the films grown at p_{N_2} = 11 % consist of a Cr solid solution, Cr_2N and a highly distorted WS_x phase.

At p_{N_2} = 28 %, peaks of the Cr_2N phase can be seen at 2θ ~ 40.1° (i.e., (002), for both WS_2 target coverage fractions), 2θ ~ 66.4° (i.e., (300), 25 area% coverage) and 2θ ~ 74.8° (i.e., (113), 37.5 area% coverage) can be seen. No evidence for the Cr solid solution observed for the lower p_{N_2} values and for CrN formation was found. For all of the coatings grown at p_{N_2} = 28 %, the presence of WS_2 and WN can not be completely excluded. The observed phase compositions of all coatings correspond well to the EPMA results in Table 1 where the Cr/N atomic ratio is higher than 1, indicating a Cr-rich solid solution or a Cr-rich solid solution + Cr_2N composite as the main film constituents, and agree well with other investigations.[23,31]

Hardness, elastic indentation modulus, residual stress, and friction coefficient of the synthesised Cr-N/WS_x films are presented in Fig. 4 as a function of p_{N_2}. For films deposited from both WS_2 target coverage fractions, an increase from hardness values of about 14 – 18 GPa without any nitrogen addition to ~ 22 GPa at p_{N_2} = 28 % was observed (see Fig. 4a). The elastic indentation moduli yielded a similar dependency, with values increasing from 210 – 230 GPa at p_{N_2} = 0 % to ~ 260 GPa at p_{N_2} = 28 % (see Fig. 4b). While no pronounced effect of the WS_2 target coverage fraction on these mechanical properties was found, the general dependence of hardness and modulus can be attributed to the formed phase composition for both WS_2 target coverage fractions. Depending on the nitrogen partial pressure and the resulting phase composition (i.e., Cr-rich solid solution, Cr-rich solid solution + Cr_2N), an increase of hardness was reported by several authors, e.g. between p_{N_2} = 7.5 - 9.5 %, where the transformation from Cr to Cr_2N dominated structures takes place.[31,32] The higher amount of WS_x in the films grown from the target with 37.5 area% WS_2 coverage fraction obviously shifts this transition up to higher nitrogen partial pressures (see Fig. 4a) compared to the 25 area% WS_2 coverage fraction. The elastic modulus follows almost the same tendency versus p_{N_2} as the hardness, although the relative variations are much smaller.

The influence of p_{N_2} on biaxial stresses is shown in Fig. 4c and exhibits for both WS_2 target coverage fractions a similar shape, with values shifted more to the compressive range for the lower WS_2 fraction. Both films grown non-reactively show slight compressive

stresses, while low tensile stresses have been observed for p_{N_2} = 11 %. These tensile stresses could be related to formation of a ternary phase structure consisting of a Cr solid solution, Cr_2N and a highly distorted WS_2 phase (see Fig. 3). A further increase of p_{N_2} to 28 % results in compressive stresses.

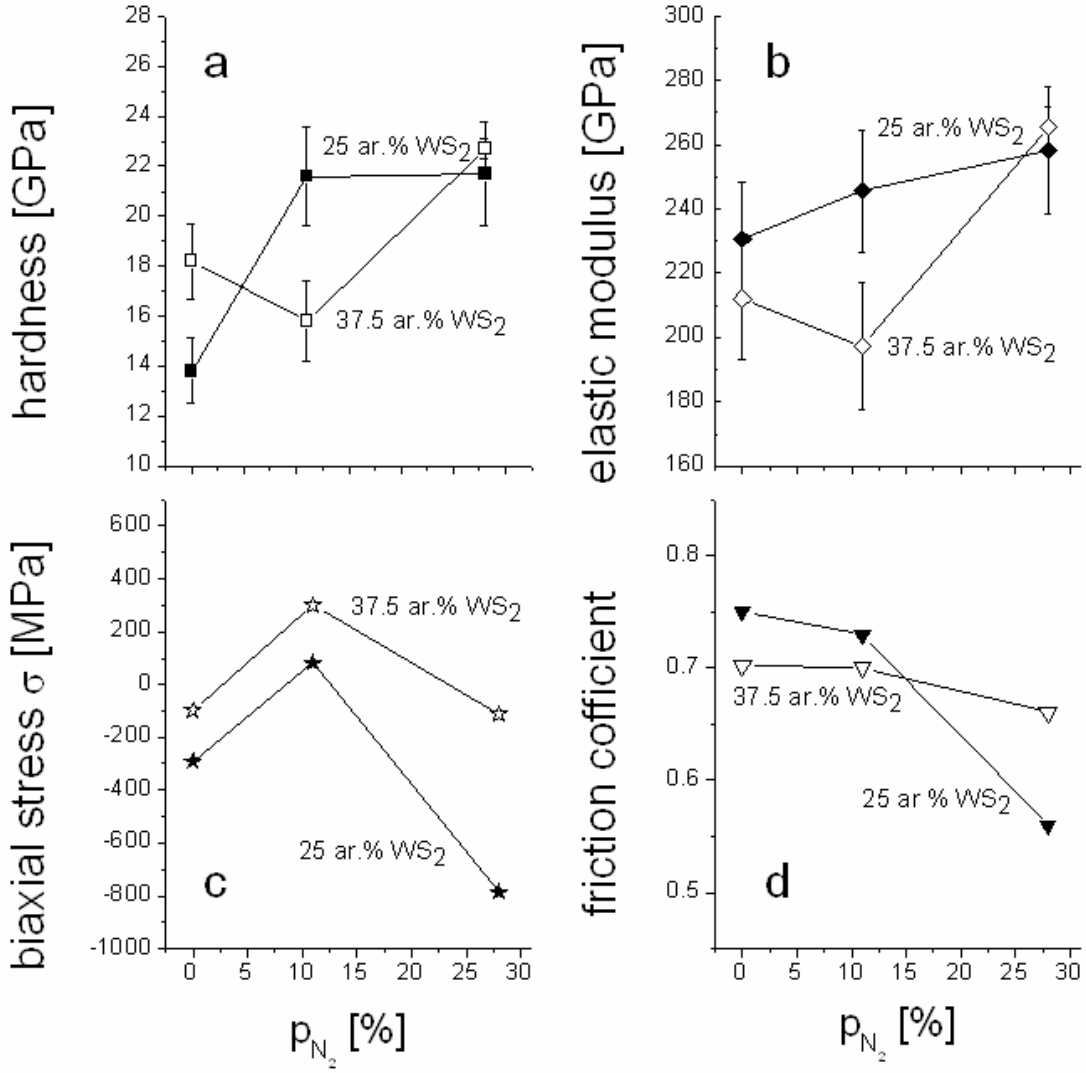

Fig. 4: (a) Hardness, **(b)** elastic indentation modulus, **(c)** biaxial stresses and **(d)** friction coefficient of Cr-N/WS_x films as a function of p_{N2} and WS_2 target coverage fraction.

Tribological investigations of the Cr-N/WS_x films were performed by means of dry-sliding ball-on-disc tests again alumina balls and the average friction coefficients are presented in Fig. 4d. Increasing p_{N_2} from 0 to 28 % results in a decrease of friction coefficients from ~ 0.75 to ~ 0.55 for films deposited from the target with 25 area% WS_2 coverage fraction, and from ~ 0.7 to ~ 0.65 for those films grown by using the 37.5 area% WS_2 coverage fraction, respectively. Due to insufficient adhesion on AISI M2 steel, two of the coatings (i.e., those grown at p_{N_2} = 11 % from the 25 area% WS_2 coverage fraction and at p_{N2} = 0 % from the target with 37.5 area% WS_2 coverage fraction) failed after ~ 20 and ~ 35 m, respectively. However, all other coatings survived the 300 m dry sliding test, with the

lowest wear track depths obtained for those films grown at p_{N_2} = 28 %. The obtained friction coefficients for coatings deposited at p_{N_2} = 28 % agree well with literature values for Cr_2N and CrN dominated films[16] as well as former investigations within the system CrN_x/MoS_x.[24] Nevertheless, it has to be concluded that neither the introduction of a WS_x phase in the coatings nor an increase of the WS_x content resulted in the aimed for friction reduction. This suggests that the formation of stoichiometric and well-crystalline WS_2 is either not possible, as already reported for MoS_2 containing films,[24] or that the content of WS_x is too low for the formation of a lamellar structure which could support the necessary lattice shearing.[33]

4. Conclusions

Coatings within the system Cr-N/WS_x were synthesised by unbalanced reactive magnetron co-sputtering using a Cr target with WS_2 inlays (25 and 37.5 area% WS_2 covering the target erosion track) in an Ar/N_2 atmosphere at various nitrogen partial pressures (p_{N_2} = 0, 11, and 28 %). The content of W and S in the coatings was significantly lower than the target composition and the S content decreased even further with increasing p_{N_2}. While low nitrogen partial pressures resulted in the formation of a Cr solid solution, composites consisting of this solid solution and Cr_2N were formed at higher p_{N_2} values. X-ray diffraction and electron probe micro-analysis suggest an additional low content of a highly distorted WS_x phase. While the formation of Cr_2N and the addition of the WS_x phase resulted in a slight increase of hardness and elastic modulus, no pronounced effect on the friction behaviour could be found in ball-on-disc dry-sliding experiments, where values comparable or even slightly above those obtained for single-phase CrN films were obtained. Thus, we have to conclude that reactive magnetron co-sputtering of Cr and WS_2 is not suitable for deposition of self-lubricating coatings.

Acknowledgments

This work was financially supported by the European Union within the NAPILIS Specific Targeted Research Project (contract NMP3 CT 2003 505622). The authors are grateful to Mr. Gerhard Hawranek for performing SEM and EPMA measurements.

References

1. W.J. Bartz: Wear, 1978, **49**, 1-18.
2. B. Bhushan: “Modern tribology handbook”, Volume 2, 793; 2001, Baton Rouge, CRC Press.
3. S.R. Cohen, L. Rapoport, E.A. Ponomarev, H. Cohen, T. Tsirlina, R. Tenne and C. Lévy-Clement: Thin Solid Films, 1998, **324**,190-197.
4. R.L. Fusaro: Lubr. Eng., 1995, 51, **3**,182-194.
5. S. Watanabe, J. Noshiro and S. Miyake: Surf. Coat. Technol., 2004, **183**, 347-351.

6. D.V. Shtansky, T.A. Lobova, V.Y. Fominski, S.A. Kulinich, I.V. Lyasotsky, M.I. Petrzhik, E.A. Levashov and J.J. Moore: Surf. Coat. Technol., 2004, **183**, 328-336.
7. C. Donnet and A. Erdemir: Surf. Coat. Technol., 2004, **180–181**, 76-84.
8. M. Regula, C. Ballif, J.H. Moser and F. Lévy: Thin Solid Films, 1996, **280**, 67-75.
9. K. Ellmer, C. Stock, K. Diesner and I. Sieber: J. Crystal Growth, 1997, **182**, 389-393.
10. J.J. Devadasan, C. Sanjeeviraja and M. Jayachandran: J. Crystal Growth, 2001, **226**, 67-72.
11. I. Martin-Litas, P. Vinatier, A. Levasseur, J.C. Dupin, D. Gonbeau and F. Weill: Thin Solid Films, 2002, **416**, 1-9.
12. Q. Cong, D. Yu, J. Wang and Y.J. Ou: Thin Solid Films, 1992, **209**, 1-8.
13. V.Y. Fominski, A.M. Markeev, V.N. Nevolin, V.B. Prokopenko and A.R. Vrublevski: Thin Solid Films, 1994, **248**, 240-246.
14. G. Weise, N. Mattern, H. Hermann, A. Teresiak, I. Bächer, W. Brückner, H.D. Bauer, H. Vinzelberg, G. Reiss, U. Kreißig, M. Mäder and P. Markschläger: Thin Solid Films,1997, **298**, 98-106.
15. A. Albu-Yaron, C. Lévy-Clément, A. Katty, S. Bastide and R. Tenne: Thin Solid Films, 2000, **361-362**, 223-228.
16. S. Carrera, O. Salas, J.J. Moore, A. Woolverton and E. Sutter: Surf. Coat. Technol., 2003, **167**, 25-32.
17. T. Hurkmans, D.B. Lewis, J.S. Brooks and W.-D. Münz: Surf. Coat. Technol., 1996, **86/87**, 192-199.
18. .S.H. Yao and Y.L. Su: Wear, 1997, **212**, 85-94.
19. J.N. Tu, J.G. Duh and S.Y. Tsai: Surf. Coat. Technol., 2000, **133/134**, 181-185.
20. T. Sato, Y. Tada, M. Ozaki, K. Hoke and T. Besshi: Wear, 1994, **178**, 95-100.
21. M. Pakala and R.Y. Lin: Surf. Coat. Technol., 1996, **81**, 233-239.
22. P. Hones, R. Sanjines and F. Lévy: Surf. Coat. Technol., 1997, **94-95**, 398-402.
23. P.H. Mayrhofer, G. Tischler and C. Mitterer: Surf. Coat. Technol., 2001, **142-144**, 78-84.
24. K. P. Budna, C. Walter, R. Spicak and C. Mitterer: Surf. Engin., 2008, **24**, 5, 350-354.
25. A. Brenner and S. Senderoff: J. Res. Natl. Bur. Stand., 1949, **42**, 105-123.
26. J. D. Wilcock and D. S. Campbell: Thin Solid Films, 1969, **3**, 3-12.
27. P. H. Mayrhofer and C. Mitterer: Surf. Coat. Technol., 2000, **133/134**, 131-137.
28. P.D. Fleischauer and R. Bauer: Tribol. Trans., 1988, **31**, 239-250.
29. O. Lignier, G. Couturier, J. Tedd, D. Gonbeau and J. Salardenne: Thin Solid Films, 1997, **299**, 45-52.
30. C. Rebholz, H. Ziegele, A. Leyland and A. Matthews: Surf. Coat. Technol., 1999, **115**, 222-229.
31. G. Wei, A. Rar and J.A. Barnard: Thin Solid Films, 2001, **398-399**, 460-464.
32. M. Pakala and R.Y. Lin: Surf. Coat. Technol., 1996, **81**, 233-239.
33. K.J. Wahl, M. Belin and I.L. Singer: Wear, 1998, **214**, 212-220.